Title

Telecommunication-Compatible, Plasmonics-Enabled Terahertz Sources and Detectors without Short-Carrier-Lifetime Photoconductors

Author

Lu, Ping-Keng

Publication Date

2022

Peer reviewed|Thesis/dissertation

UNIVERSITY OF CALIFORNIA
Los Angeles

Telecommunication-Compatible, Plasmonics-Enabled Terahertz Sources and Detectors without Short-Carrier-Lifetime Photoconductors

A dissertation submitted in partial satisfaction
of the requirements for the degree
Doctor of Philosophy in Electrical and Computer Engineering

by

Ping-Keng Lu

2022

ABSTRACT OF THE DISSERTATION

Telecommunication-Compatible, Plasmonics-Enabled Terahertz Sources and Detectors without Short-Carrier-Lifetime Photoconductors

by Ping-Keng Lu

Doctor of Philosophy in Electrical and Computer Engineering

University of California, Los Angeles, 2022

Professor Mona Jarrahi, Chair

Photoconductive terahertz devices require ultrafast (< 1 ps) carrier dynamics to generate and detect terahertz radiation. Conventionally, they have been heavily reliant on the use of defect-introduced short-carrier-lifetime photoconductors. While quite a few excellent results have been achieved by using short-carrier-lifetime photoconductors, the high concentration of defects intentionally incorporated in the active photo-absorbing material leads to lower carrier mobility and substantial degradation of photoconductive gain due to photocarrier scattering, trapping and recombination. Additionally, realization of many short-carrier-lifetime photoconductors is only possible at limited facilities due to the need for non-standard processes, as well as rare elements as defect-introducing dopants. Therefore, alternative approaches to realize terahertz sources and detectors have attracted increasing attention. During my doctoral studies, I have established two different approaches to develop photoconductive terahertz sources and detectors without using short-carrier-lifetime photoconductors. These approaches are based on carrier transit time reduction and photoconductor band engineering to introduce ultrafast carrier dynamics. With the strong optical field enhancement offered by plasmonic nanostructures, photocarrier generation in plasmonic photoconductors can be highly confined near the terahertz radiating elements, leading

to significantly reduced transport distances for the photocarriers that facilitates broadband terahertz operation. As a result, by utilizing the plasmonics-enabled carrier transit time reduction, high-efficiency terahertz sources and detectors are realized for both pulsed and continuous-wave operation. This scheme provides a generic and reliable approach for designing photoconductive terahertz devices using various semiconductors and optical wavelengths. Moreover, by engineering the photoconductor band structure, highly reliable bias-free terahertz sources are realized with multiple orders of magnitude improvement in optical-to-terahertz conversion efficiency compared to other passive terahertz generation techniques. In particular, a record-high-power pulsed terahertz source with a radiation power of 860 μW is demonstrated using a novel graded-composition InGaAs structure. Furthermore, to minimize terahertz propagation loss in the substrate, bias-free sources are successfully implemented on a silicon substrate, which not only leads to an increased radiation bandwidth, but also enables integrability with silicon photonic platforms, largely extending the scope and potential uses of terahertz sources to a diversity of practical applications.

The dissertation of Ping-Keng is approved.

Chee-Wei Wong

Benjamin S. Williams

Aydin Babakhani

Mona Jarrahi, Committee Chair

University of California, Los Angeles

2022

To my parents, Mou-Tien Lu and Yu-Yen Chu

To my wife, I-Ju Yu

Table of Contents

LIST OF TABLES AND FIGURES

ACKNOWLEDGEMENTS

First of all, I would like to express my deepest gratitude to my advisor Prof. Mona Jarrahi for all of her guidance and support throughout my study and research in the PhD program. Successfully going through this long and challenging journey is only possible thanks to her mentorship as well as all the resources she strives to provide. I feel grateful to have this opportunity in my life to challenge myself and to extend my knowledge and problem-solving skills.

I would like to thank my PhD committee members Prof. Benjamin Williams, Prof. Chee Wei Wong, and Prof. Aydin Babakhani for all their suggestions and guidance of my research, improving its quality in terms of breadth and depth. I would also like to thank Dr. Baolai Liang for growing countless MBE samples for me that enables all the research studies to be conducted.

I would also like to thank all previous and current members of Terahertz Electronics Laboratory directed by Prof. Jarrahi, including Dr. Shang-Hua Yang, Dr. Ning Wang, Dr. Nezih Tolga Yardimci, Dr. Deniz Turan, Dr. Semih Cakmakyapan, Dr. Leihao Wei, Yen-Ju Lin, Xurong Li, Yifan Zhao, Joseph Hwang, Ruixuan Zhao, Xinghe Jiang, Vivek Parimi, Tianyi Gan, and Anika Tabassum. Special thanks to Dr. Nezih Tolga Yardimci and Dr. Deniz Turan for all their help in numerous experiments that I tried to carry out.

I want to especially thank my wife I-Ju Yu for years of support and company through the period of my PhD study. Finally, I want to express my sincere gratitude for my brother Ping-Tsong Lu and my parents Mou-Tien Lu and Yu-Yen Chu for always encouraging me to pursue my interest in scientific exploration. This would not be possible without your decade-long, wholehearted help and support that give me the courage to keep moving forward.

VITA

2008 – 2012 B.Sc. in Electronics Engineering, National Chiao Tung University, Hsinchu.

2011 – 2012 Non-degree exchange student at University of Illinois at Urbana-Champaign.

2012 – 2014 M.Sc. in Electronics Engineering, National Chiao Tung University, Hsinchu.

2015 – 2022 Graduate Student Research Assistant under Professor Mona Jarrahi, University of California – Los Angeles.

PUBLICATIONS

Journal Papers

- W. Wang, P. K. Lu, A. K. Vinod, et al. “Coherent terahertz synthesis with 2.8-octave tunability and sub-Hz linewidths through chip-scale photomixed microresonator optical parametric oscillation.” in review by *Nature Communications*
- P. K. Lu, X. Jiang, Y. Zhao, et al. "Bias-free terahertz generation from a silicon-compatible photoconductive emitter operating at telecommunication wavelengths." in review by *Applied Physics Letters*
- P. K. Lu, A. D. J. F. Olvera, D. Turan, et al. "Ultrafast carrier dynamics in terahertz photoconductors and photomixers: beyond short-carrier-lifetime semiconductors." Nanophotonics (2022).
- P. K. Lu, D. Turan, and M. Jarrahi. “High-power terahertz pulse generation from bias-free nanoantennas on graded composition InGaAs structures.” Optics Express 30.2 (2022): 1584-1598.

- D. Turan, P. K. Lu, N. T. Yardimci, et al. “Wavelength conversion through plasmon-coupled surface states.” Nature Communications, 12.1 (2021): 1-8.
- P. K. Lu, D. Turan, and M. Jarrahi. "High-sensitivity telecommunication-compatible photoconductive terahertz detection through carrier transit time reduction." Optics Express 28.18 (2020): 26324-26335.
- S. Cakmakyapan, P. K. Lu, A. Navabi, et al. “Gold-patched graphene nano-stripes for high-responsivity and ultrafast photodetection from the visible to infrared regime.” Light: Science & Applications 7.1 (2018): 20. (2019 top-downloaded paper)
- J. Y. Wu, P. K. Lu, and S. D. Lin. "Two-dimensional photo-mapping on CMOS single-photon avalanche diodes.” Optics Express 22.13 (2014): 16462-16471.
- J. Y. Wu, P. K. Lu, Y. J. Hsiao, and S. D. Lin. "Radiometric temperature measurement with Si and InGaAs single-photon avalanche photodiode." Optics Letters 39.19 (2014): 5515-5518.

Chapter 1: Introduction

1.1. Photoconductive Terahertz Generation and Detection

The terahertz frequency range is loosely defined as the part of the electromagnetic spectrum between 100 GHz and 10 THz, which is above microwave and below infrared frequencies. Due to the presence of rotational resonances and collective librations of various polar molecules, the terahertz frequency range is widely explored for a plethora of applications including chemical sensing and material characterization, where highly frequency-selective absorption signatures provide ample information about the identity and physical characteristics of the sample under test [1-4]. In addition, terahertz waves can transmit through many optically opaque materials such as paper, plastics, textiles, and weakly doped semiconductors [5-9]. Therefore, terahertz radiation is well-suited for imaging and sensing applications in many optically inaccessible environments [10-13]. With photon energies below 40 meV, terahertz waves are non-ionizing and, hence, suited for many biomedical imaging, diagnosis and nondestructive quality inspection [14-22].

Generation and detection of terahertz radiation have been extensively realized through ultrafast photoconductors, which translate the mixing products of the frequency components of an optical pump beam to a terahertz photocurrent. A common implementation — the so-called photoconductive antenna (PCA) — uses a semiconductor-based photoconductor integrated with a metallic terahertz antenna. When photons with an energy above the semiconductor's band gap are absorbed by the semiconductor, mobile electron-hole pairs are generated. The concentration of these photocarriers oscillates at the beat terahertz frequencies that are generated from the mixing of the incident optical frequency components. These photocarriers are accelerated under an electric field and form a photocurrent. This electric field can be supplied through an external bias voltage

or a built-in field in the semiconductor. The electric field should be strong enough to drift the photocarriers at high velocities in order to attain a large photocurrent amplitude, which directly translates into strong terahertz radiation that is emitted by the antenna. The scheme can also be reversed to detect terahertz radiation: the antenna attached to a photoconductor receives the terahertz electric field that accelerates the pump-induced photocarriers. The resulting photocurrent is proportional to the convolution of the terahertz field and the laser-induced photoconductivity. Photoconductive terahertz emitters and detectors are utilized in pulsed or continuous-wave (CW) operation. For pulsed operation, a femtosecond laser is typically used as the optical pump source to generate and detect sub-picosecond terahertz pulses with a spectral width of several THz. For CW operation, two CW lasers with the same polarization and a terahertz frequency difference are superimposed to create an optical pump beam with a single-frequency beatnote that is used for the generation and detection of CW terahertz radiation.

1.2. Photoconductive Antennas for Spectroscopy Applications

Since the invention in 1984 by David H. Auston et al. at Bell Labs [23, 24], PCAs have been extensively studied for their use in both generation and detection of pulsed and CW terahertz radiations. Their compactness and room-temperature operation make them one of the most widely used technologies in various terahertz systems [25-44]. As mentioned above, terahertz waves have been extensively utilized to probe the unique spectral absorption and/or dispersion signatures of a wide range of substances — an application field called terahertz spectroscopy. Generally, terahertz spectroscopy systems can be classified into time-domain and frequency-domain categories.

As shown in Fig. 1.1, in a terahertz time-domain spectroscopy (THz-TDS) system, a femtosecond laser is used to pump/probe a terahertz source/detector to generate/detect a pulsed electric field with less than 1 ps duration, which carries broadband frequency components

simultaneously. A delay stage is used to change the time-delay between the pump and probe beams, so that the entire terahertz waveform can be captured. The obtained terahertz electric field is then post-processed by Fourier transform and averaging to obtain the terahertz spectrum. Compared to the frequency-domain scheme, THz-TDS systems usually achieve larger bandwidth and higher signal-to-noise ratio (SNR). Additionally, they can be used to realize time-of-flight imaging and resolve the depth information of multilayer structures, leading to the realization of terahertz tomography applications [45-47]. Despite these advantages, the frequency resolution of THz-TDS systems is typically limited to a few GHz.

For applications requiring very high spectral resolution, terahertz frequency-domain spectroscopy (THz-FDS) systems are used (Fig. 1.1). In these systems, narrowband CW terahertz radiation is typically generated and detected by beating two CW lasers. The spectrum is obtained by recording the detector output while tuning the beat frequency. Since THz-FDS systems do not require femtosecond lasers to operate, their cost is much lower compared to THz-TDS systems. THz-FDS systems are able to achieve sub-MHz spectral resolution, which is required for applications where closely spaced spectral lines exist, like gas spectroscopy [48]. In addition, THz-FDS systems are required for applications that need to accurately characterize the lineshape and/or broadening parameters of the spectral features of various gases to understand their detailed physical properties, such as air pollution monitoring and astrophysics studies [49, 50].

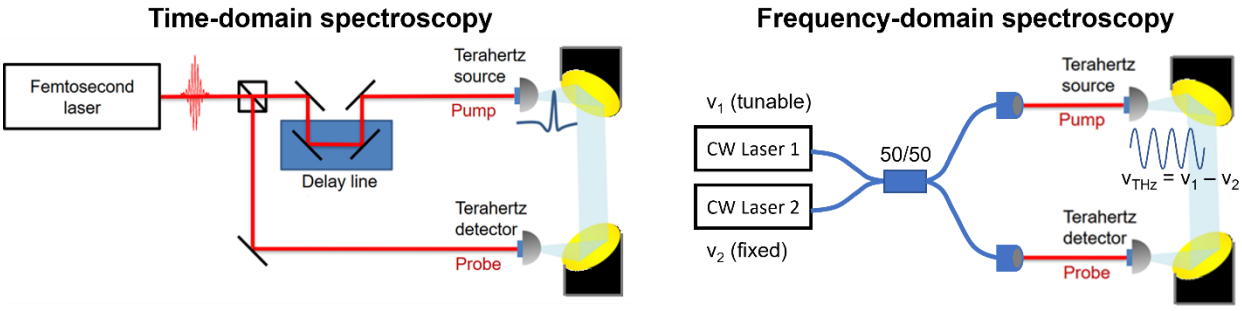

Fig. 1.1: Generic schematics of terahertz time-domain and frequency-domain spectroscopy systems.

1.3. Telecommunication-Compatible Photoconductive Antennas with Short-Carrier-Lifetime Photoconductors

Ultrafast dynamics of the photocarriers, with sub-picosecond to picosecond response times, are necessary to facilitate the broadband operation of terahertz photoconductors. A very commonly used approach to fulfill this requirement is to use short-carrier-lifetime semiconductors, where high concentrations of intentional defects are introduced into the semiconductor lattice, leading to extremely short carrier trapping times less than 1 ps. Low-temperature-grown GaAs (LT-GaAs) was the first, and is still one of the most commonly used short-carrier-lifetime semiconductors for terahertz generation and detection when working with an ~800 nm optical pump wavelength [51-54]. Growing GaAs at a low temperature (200-350 °C) and subsequent in-situ annealing at higher temperatures [52-54] induces crystal defects due to excess arsenic, which captures the photocarriers within less than one picosecond.

Following the same concept of defect introduction, a diversity of methods for growing short-carrier-lifetime photo-absorbing semiconductors at various optical excitation wavelengths have been introduced [55-61]. In particular, short-carrier-lifetime semiconductors with high photo-absorption at telecommunication wavelengths (~1550 nm) are of strong interest, because this will enable the integration with low-cost, small-footprint, and highly reliable fiber lasers as well as fiber-optic components. However, providing a high optical absorption at ~1550 nm wavelength requires a small enough bandgap energy (< 0.8 eV, such as $In_{0.53}Ga_{0.47}As$) for the photoconductor, which leads to a low substrate resistivity, causing early thermal breakdown for terahertz sources and high Johnson-Nyquist noise currents for terahertz detectors. As a result, the development of short-carrier-lifetime photoconductors based on these substrates has been challenging, because defect introduction has often led to even higher background carrier concentrations [62], resulting

in even lower substrate resistivity. To date, some of the most successful approaches to realize short-carrier-lifetime photoconductors at ~1550 nm wavelength include heavy-ion irradiation [62-65], incorporating rare-earth elements [66-68], transition metal doping [69-71], and low-temperature-grown InGaAs/InAlAs multilayer heterostructures [72-74].

While many impressive results have been demonstrated using short-carrier-lifetime photoconductors, their ultrafast carrier dynamics comes with several tradeoffs in photoconductive gain, optical responsivity, carrier mobility, and thermal conductivity. In particular, due to the sub-picosecond lifetime of the photocarriers, a substantial fraction of them is trapped and then recombined before contributing to the generation and detection of terahertz radiation, leading to degraded efficiency (i.e. the photoconductive gain) of the terahertz photoconductors. Also, while some growth methods for short-carrier-lifetime semiconductors like LT-GaAs are well-established processes performed by many groups, most growth methods for short-carrier-lifetime semiconductors utilize non-standard processes and, in some cases rare dopant elements, that are not readily available in most molecular beam epitaxy (MBE) and metal organic chemical vapor deposition (MOCVD) facilities, limiting their accessibility and widespread usage. In addition, these methods have to be adapted for each specific semiconductor, limiting the materials and optical wavelengths that can be used for realizing terahertz photoconductors. These drawbacks have motivated the emergence of alternative terahertz photoconductor and photomixer concepts that do not rely on short-carrier-lifetime semiconductors.

1.4. Telecommunication-Compatible Photoconductive Antennas without Short-Carrier-Lifetime Photoconductors

Instead of using defect-induced short-carrier-lifetime photoconductors, ultrafast carrier dynamics can be realized through alternative approaches including carrier transit time reduction through plasmonics, and optimization of semiconductor built-in electric field, as elaborated in detail in the following sections.

1.4.1. Use of Plasmonic Nanostructures

Fundamentals of plasmonics

Plasmonics refers to the research field that deals with collective, coherent electron oscillations, a.k.a. plasmons, and their interactions with electromagnetic waves. Of particular interest is the plasmons that reside at the interface between metallic and dielectric materials, called surface plasmon polaritons (SPPs). Constrained by the metal-dielectric boundary conditions, only transverse-magnetic (TM) SPPs can exist. The dispersion relation of SPPs is shown in Fig. 1.2, which shows that SPPs at all energies possess larger wave vectors than free space photons [75]. Due to their large wave vectors, these SPPs can propagate along the metal-dielectric interface with very tight electromagnetic field confinement [76-80], leading to strong light-matter interactions that can be exploited in a wide range of applications. However, direct excitation of SPPs with free space electromagnetic waves is not allowed because of the mismatch between their wave vectors. As a result, several methods have been developed to enable this excitation by effectively providing an additional wave vector. Periodic structuring of the metal-dielectric interface is a simple way that has been widely used. Typically, periodic metallic nanostructures are fabricated on the surface of a dielectric material to facilitate SPP excitation at optical frequencies.

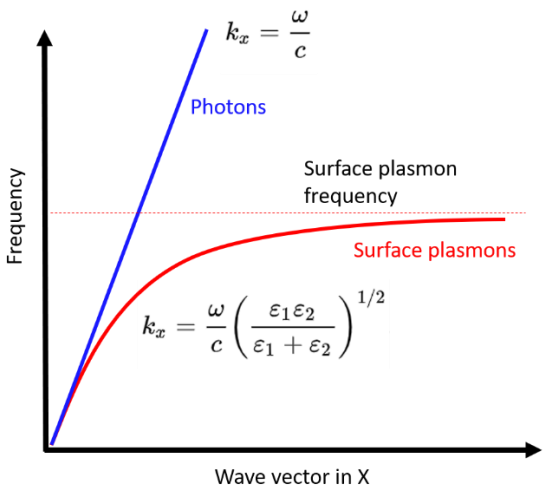

Fig. 1.2: Surface plasmon dispersion relation, showing that surface plasmons always have larger wave vector than free space photons.

Choosing a proper metal for plasmonics-enhanced PCAs involves a number of important considerations. First, the utilized metal should offer strong optical field enhancement near the plasmonic nanostructures at the optical pump wavelength. The utilized metal should not support any interband transition to prevent the direct absorption of the optical pump in the metal rather than the photoconductive substrate. For these reasons, gold and silver are extensively used in plasmonic devices pumped at visible and near-infrared optical wavelengths. Second, the utilized metal should be chemically stable and adhere well to the photoconductive substrate. Compared to silver, gold is much more resistant to oxidation and its high electrical and thermal conductivities are highly beneficial for operation at high optical pump powers. Therefore, most plasmonics-enhanced PCAs use gold as the plasmonic metal.

Plasmonic contact electrodes for photoconductive terahertz devices

The unique properties of SPPs have contributed to several impactful advancements in various scientific areas. In addition to breakthroughs in nonlinear optics [79], near field imaging and spectroscopy [81, 82], as well as electromagnetic waves detection and manipulation [83-85], it

was also recently shown that the use of plasmonic nanostructures can reduce the impulse response duration of long carrier lifetime photoconductors, enabling efficient generation and detection of both pulsed and CW terahertz waves [86-91]. This is because the concentration of the optical pump beam and photo-generated carriers in the photoconductor active area can be manipulated by plasmonic nanostructures so that the transport path length and average carrier transit time for most of the photocarriers are significantly reduced.

Plasmonic nanostructures are very commonly designed in the form of grating patterns that, under optimized geometry, enable the excitation of surface plasmon waves at the metal-dielectric interface by an incident transverse magnetic optical beam. A key development that significantly enhances the efficiency of terahertz devices is the realization of plasmonic contact electrodes since its introduction in 2010 [92], where the plasmonic gratings are used to both excite surface plasmon waves and collect the photocarriers, as shown in Fig. 1.3. This leads to significantly enhanced optical generation at the interface between the plasmonic contact electrodes and the photoconductor. As a result, this enhancement largely reduces the average transport path length and carrier transit time of the photocarriers to the plasmonic electrodes, leading to higher photocarrier collection efficiency and creating a strong ultrafast photocurrent that is dominated by electrons due to their high carrier mobility (Fig. 1.3). This plasmonics-enabled ultrafast carrier dynamics has been extensively explored to enhance the performance for both terahertz sources and detectors [93-118].

The strong surface confinement of optical generation offered by plasmonic electrodes provides a crucial benefit for telecommunication-compatible photoconductors, because it enables the use of thin photo-absorbing layers (200 nm or less) with negligible impact on the SNR. Reduction of the photo-absorbing layer thickness leads to lower dark leakage currents for terahertz sources and

lower Johnson-Nyquist noise levels for terahertz detectors. Furthermore, the high carrier mobility of non-short-carrier-lifetime photoconductors facilitates the ultrafast transport of the photocarriers, enabling broadband operation of the terahertz devices [90].

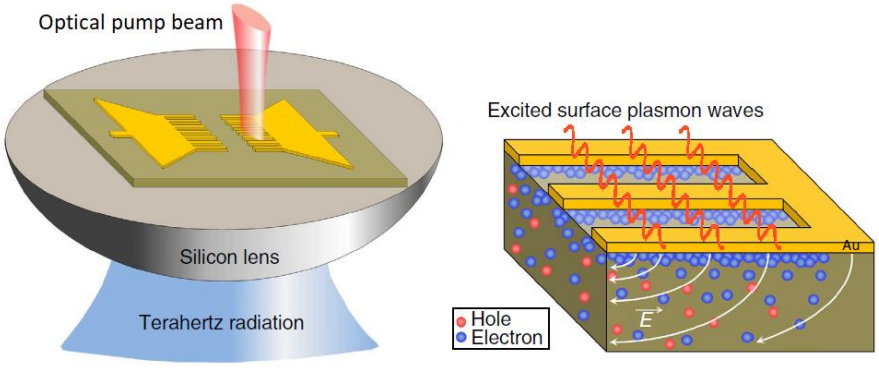

Fig. 1.3: Illustrations for a plasmonic PCAs based on a bow-tie antenna.

1.4.2. Use of Semiconductor Built-in Electric Field

Origin of semiconductor built-in electric field

When the semiconductor lattice is terminated, the break in the lattice symmetry results in the formation of electronic states with energies lying between the conduction band (CB) and the valance band of the semiconductor. These states can act either as donors or acceptors which carry a positive or negative charge when ionized, respectively. The ionized states at the semiconductor surface push the Fermi energy to the charge neutrality level of the surface states, i.e. to the position where the net charge of the states is zero. This Fermi level pinning results in a band bending between the bulk and the surface of a semiconductor material as illustrated in Fig. 1.4a [119-122]. As a result, a built-in electric field is formed between the semiconductor surface and the bulk. The electric field present at the semiconductor surface can be used for ultrafast transit of the photocarriers and generation of terahertz radiation. When the pump photons are absorbed in the semiconductor, the generated electron-hole pairs close to the semiconductor surface can be

accelerated by this built-in field and generate an ultrafast current within the semiconductor, realizing photomixing within the substrate without requiring any external bias voltage. This bias-free operation is highly beneficial for telecommunication-compatible photoconductive emitters because the undesired dark leakage current of the emitter is completely eliminated, leading to excellent reliability. On the contrary, many of the terahertz emitters realized on telecommunication-compatible short-carrier-lifetime photoconductors need high bias voltages (> 100 V) to generate acceptable terahertz power levels (> 50 μW) [69, 71, 73, 123-125].

Bias-free terahertz emitters

In a conventional bias-free surface-field emitter, optical excitation is directed under an angle with respect to the semiconductor surface normal such that terahertz waves normal to the semiconductor surface can be generated to allow more effective collection and utilization of the radiation. Terahertz generation as a result of the transported carriers through the surface built-in field (Fig. 1.4a) should not be confused with the photo-Dember effect (Fig. 1.4b), which is another bias-free terahertz emission mechanism [126, 127]. When an optical pump beam is absorbed in the semiconductor, photogenerated electrons and holes diffuse from the surface, where most carriers are generated according to Lambert Beer's law, towards the bulk due to the formation of a concentration gradient. The higher effective mass (lower mobility) of holes causes a difference between the hole and electron diffusion currents, resulting in the formation of a dipole inside the substrate, giving rise to terahertz generation (Fig. 1.4b). This process is referred to photo-Dember effect. The polarity of the generated terahertz electric field can be used to determine whether carrier drift or diffusion dominates the terahertz generation process. In most n-type semiconductors, the built-in field direction is towards the surface, drifting the photogenerated electrons towards the bulk, and holes towards the surface. In most p-type semiconductors, the built-in field direction is

towards the semiconductor, drifting the electrons towards the surface and holes towards the substrate. Therefore, the polarity of this drift current flips when the semiconductor doping type is changed, resulting in a polarity change in the generated terahertz electric field. In contrast, the net direction of electron diffusion is always from the semiconductor surface towards the substrate. Therefore, the direction of the current is independent of the doping type of the semiconductor.

Semiconductor surface states may induce very high built-in electric fields thanks to the Fermi level pinning at the surface. However, the extent of the built-in electric field is shallow in many semiconductors, limiting the amplitude of the generated ultrafast photocurrent for terahertz generation [128]. It was recently shown that plasmonic nanoantennas can be used to efficiently couple the incident optical pump beam to the semiconductor surface states, enabling a high concentration of photocarrier generation near the semiconductor surface where the intensity of the built-electric field is maximized, leading to high-efficiency bias-free terahertz generation [91, 129]. Moreover, the use of plasmonic nanoantennas effectively re-orients the induced photocurrent components in the direction parallel to the semiconductor surface. As a result, both the incident optical beam and the radiated terahertz beam are normal to the surface, which allows easy and high-efficiency collection of the radiated terahertz beam. It should be noted that this benefit does not exist for conventional surface-field emitters based on plain semiconductor substrates.

For practical applications where lower optical pulse energies are favored, plasmonic-enhanced bias-free emitters based on semiconductor surface-field have demonstrated much higher optical-to-conversion efficiencies compared to other bias-free emitters based on photo-Dember effect, nonlinear optics, and spintronics [91, 129].

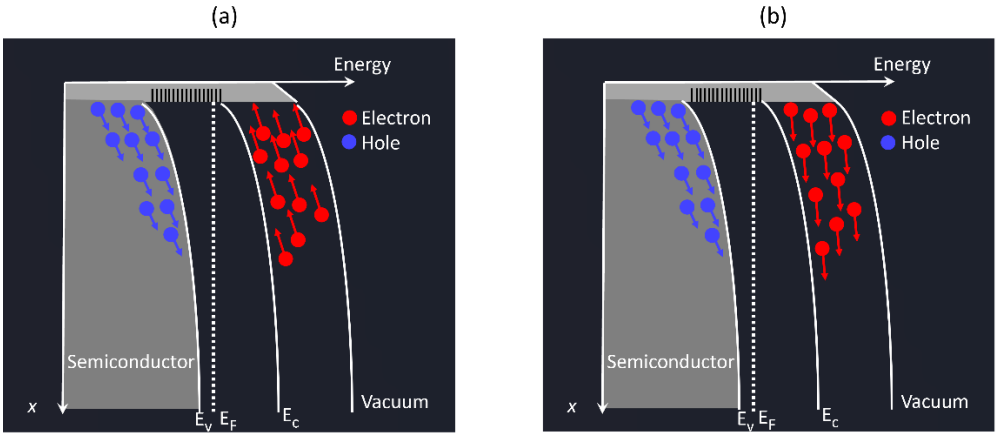

Fig. 1.4: The band structure of a p-type semiconductor surface emitter utilizing (a) the built-in electric field induced near the semiconductor surface and (b) photo-Dember effect.

1.5. Thesis Outline

The dissertation presents a detailed study of two novel approaches to telecommunication-compatible device design that provide ultrafast photoconductive response without requiring short-carrier-lifetime photoconductors. In Chapter 2, the first approach is elaborated, where plasmonics-enabled carrier transit time reduction allows the realization of broadband terahertz sources and detectors for both pulsed and CW operation. In particular, the demonstrated detector prototype offers a record-high sensitivity with a 122 dB SNR. Next in Chapter 3, the second approach is explained, which is based on the combined utilization of plasmonic enhancement and the strong built-in electric field in semiconductors, leading to broadband and high-power terahertz generation without requiring any external bias voltage. As a result, the undesired dark leakage current is completely removed, substantially increasing the emitter reliability. Specifically, the realized emitters based on graded-composition InGaAs structures provide a record-high pulsed terahertz radiation power of 860 μW, with orders of magnitude improvement in optical-to-terahertz conversion efficiency compared to other passive terahertz generation techniques. Finally, the conclusion and the outlook of the thesis are given in Chapter 4.

Chapter 2: Plasmonics-Enabled Ultrafast Carrier Dynamics with Carrier Transit Time Reduction

As mentioned in Section 1.3, although most of the photoconductive terahertz devices operating at 1550 nm have been realized using short-carrier-lifetime photoconductors, they impose some serious limitations in terms of the reduced photoconductive gain, optical responsivity, carrier mobility, and thermal conductivity, as well as the lack of wide accessibility and adaptability with various photoconductor materials.

It should be noted that pulsed terahertz detection as well as CW terahertz generation and detection have been particularly reliant on short-carrier-lifetime photoconductors in conventional designs due to the requirement of a sub-picosecond response time. On the contrary, long-carrier-lifetime photoconductors have been successfully used for realizing pulsed terahertz emitters [130-133], since the photoconductor has higher carrier mobility, and it can relax to the dark state between consecutive optical pump pulses. Therefore, this chapter is focused on the demonstration of pulsed detectors as well as CW emitters and detectors operating at telecommunication wavelengths (~1550 nm) with plasmonics-enabled carrier transit time reduction, eliminating the need for short-carrier-lifetime photoconductors.

2.1. Pulsed Operation of Terahertz Photoconductive Antennas Utilizing Carrier Transit Time Reduction

2.1.1. Background

To address the limitations of photoconductive terahertz detectors based on short-carrier-lifetime photoconductors, our group has previously proposed an alternative approach to provide an ultrafast detector response by reducing carrier transit time instead of carrier lifetime [89, 109]. By utilizing plasmonic nanostructures and exciting surface plasmon waves, the intensity of the optical probe beam is significantly enhanced near the contact electrodes of the photoconductive detectors [93-118]. As a result, most photo-generated carriers are highly concentrated within tens of nanometers beneath the contact electrodes, where the induced terahertz field will quickly collect the carriers. Therefore, the transport path length and transit time of the photo-generated carriers to the contact electrodes are significantly reduced to obtain an ultrafast terahertz detection operation. Consequently, this approach eliminates the need for a short-carrier-lifetime photoconductor, and photoconductors with a high carrier mobility can be used to realize high-responsivity terahertz detectors. This approach was first demonstrated with a large-area terahertz detector based on plasmonic nanoantenna arrays designed for operation at an 800 nm optical wavelength [89]. A combination of the plasmonic nanoantennas and an AlAs/AlGaAs distributed Bragg reflector (DBR) was used to form a nanocavity to confine photocarrier generation inside a thin GaAs layer under the plasmonic nanoantennas. Following this work, another study extended the operation wavelength of these large-area plasmonic photoconductive terahertz detectors to ~1 μm by using a plasmonic nanoantenna array to confine photocarrier generation inside a thin $In_{0.24}Ga_{0.76}As$ layer under the plasmonic nanoantennas [109]. Despite the high-performance terahertz detection achieved in these studies, the utilized terahertz detector architecture based on a large-area

plasmonic nanoantenna array does not provide an acceptable SNR when adopted for operation at optical wavelengths around 1550 nm. This is because of the considerably lower resistivity of photoconductive substrates at ~1550 nm wavelengths, which results in a substantially lower detector resistance and, thus, higher Johnson-Nyquist noise current when adopting the detector architecture based on a large-area plasmonic nanoantenna array [134].

As an example, a terahertz detector prototype based on a 250 μm × 250 μm large-area plasmonic nanoantenna array is designed for operation at 1550 nm wavelength (Fig. 2.1a). The detector is fabricated on an epitaxial semiconductor structure consisting of a 200-nm-thick undoped $In_{0.53}Ga_{0.47}As$ layer and a 200-nm-thick AlAs layer grown on a semi-insulating GaAs (SI-GaAs) substrate by MBE. The $In_{0.53}Ga_{0.47}As$ layer is the photo-absorbing active region of the terahertz detector. The indium concentration of 53% is chosen to obtain a high absorption coefficient at 1550 nm and a low substrate conductivity simultaneously. In addition, limiting the thickness of this layer prevents the generation of photocarriers deeper inside the semiconductor substrate, enabling a short transit time to the nanoantenna arrays for the majority of the photo-generated carriers. The AlAs layer serves as a high resistivity buffer to lower the substrate conductivity. The resistance of the detector, however, is not determined only by the substrate conductivity, but also by the geometry of the nanoantenna array. In contrary to the previous designs optimized for operation at shorter wavelengths [89, 109], for which photoconductors with higher bandgap energies and much lower conductivity levels were used, the fabricated terahertz detector based on the nanoantenna-array optimized for operation at 1550 nm wavelength has a much lower device resistance (tens of Ω as opposed to tens of kΩ for detectors optimized for operation at shorter wavelengths at tens of mW optical power). As shown in Fig. 2.1b, the SNR and bandwidth of a fabricated detector prototype with this nanoantenna array architecture is severely limited by the

high Johnson-Nyquist noise current caused by the low resistance of the detector. After capturing and averaging 1000 time-domain traces, the detector offers only 60 dB SNR over a ~2 THz bandwidth. To address this performance limitation, we present a new architecture for telecommunication-compatible photoconductive terahertz detectors without short-carrier-lifetime photoconductors that uses a broadband logarithmic spiral antenna with a small active area and, hence, a large resistance to offer more than a 122 dB SNR over a 3.6 THz detection bandwidth. In principle, this generic approach can be applied to design terahertz detectors operating at any given optical wavelength without being limited by the availability of short-carrier-lifetime photoconductors.

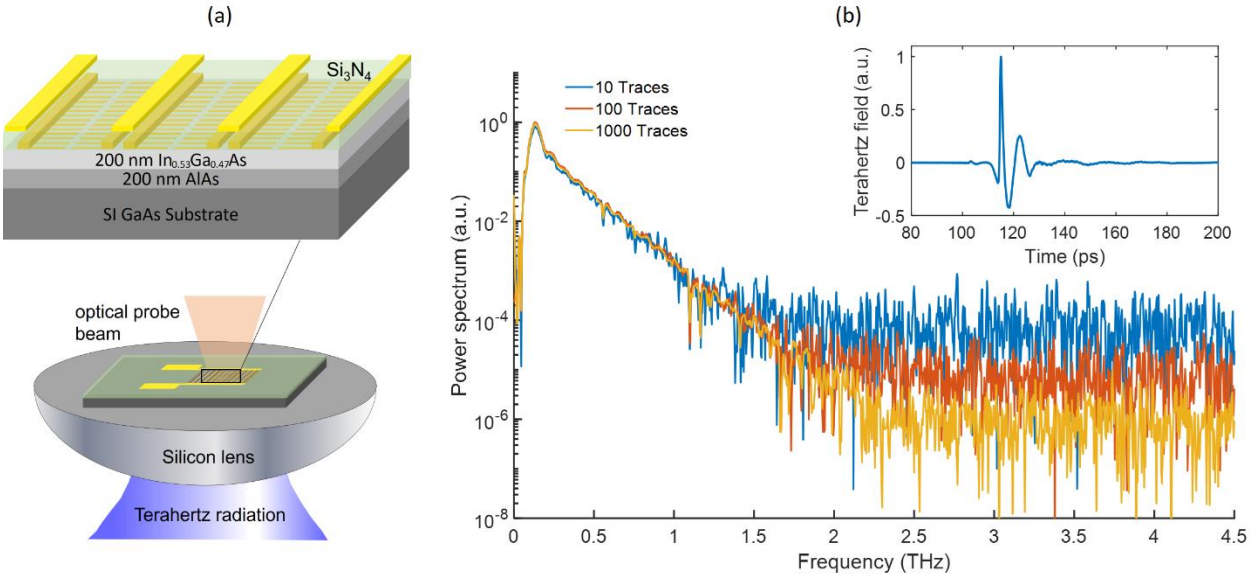

Fig. 2.1: (a) Schematic of the terahertz detector prototype based on a nanoantenna-array optimized for operation at 1550 nm. The 4-µm-wide metal stripes on the top are shadow metals to eliminate undesired photo-generation. The 2-µm-wide metal stripes on the $In_{0.53}Ga_{0.47}As$ surface are connected to the nanoantennas for current collection. The nanoantennas have an arm-length of 4 µm, separated by a 2 µm gap. (b) The measured power spectra corresponding different number of captured and averaged time-domain traces using a THz-TDS system. Inset shows the captured time-domain terahertz waveform.

2.1.2. Device Design and Fabrication

As illustrated in Fig. 2.2, the terahertz detector consists of a photoconductor with plasmonic contact electrodes integrated with a broadband logarithmic spiral antenna. The detector is fabricated on the same epitaxial semiconductor structure consisting of a 200-nm-thick undoped $In_{0.53}Ga_{0.47}As$ layer and a 200-nm-thick AlAs layer grown on an SI-GaAs substrate. The plasmonic contact electrodes, which are in the form of one-dimensional metallic gratings separated by a small tip-to-tip gap, have a 5 μm × 10 μm area each. They are designed to enhance optical intensity inside the $In_{0.53}Ga_{0.47}As$ layer near the tip of the gratings by excitation of surface plasmon waves. The $In_{0.53}Ga_{0.47}As$ layer is etched everywhere except under the plasmonic electrodes to form a mesa structure, which prevents photocarrier generation outside the device active area and increases the resistance of the detector. Covered with a Si_3N_4 anti-reflection coating (ARC), the plasmonic electrodes are optimized to offer the largest absorption of a TM incident optical beam at 1550 nm in the $In_{0.53}Ga_{0.47}As$ layer.

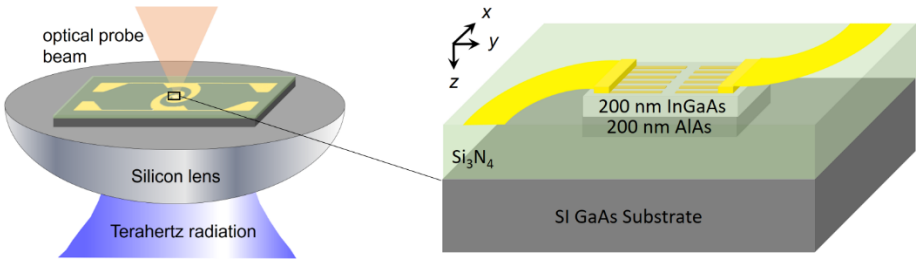

Fig. 2.2: Schematic of the spiral-antenna-based plasmonic terahertz detector operating at 1550 nm.

A numerical software based on finite-difference time-domain (FDTD) method (Lumerical) is used to analyze the interaction of the optical beam with the plasmonic grating to optimize its geometry. The optimum geometry has a 460 nm periodicity, an 80 nm grating gap, a 3/77 nm Ti/Au height, and a 240 nm Si_3N_4 ARC thickness. Using this grating geometry, an ~50% absorption is estimated for a TM-polarize optical beam at 1550 nm (Fig. 2.3a). Figure 2.3b shows

the optical absorption profile in the *x*-*z* and *y*-*z* cross-sections of the substrate near the tips of the gratings for a tip-to-tip gap size of 1 µm. Since the optical coupling is enhanced by the excitation of surface plasmon waves, most of the absorption is confined to the areas near the metal/semiconductor interface, providing a sub-picosecond transit time for the majority of the photo-generated carriers in the $In_{0.53}Ga_{0.47}As$ layer.

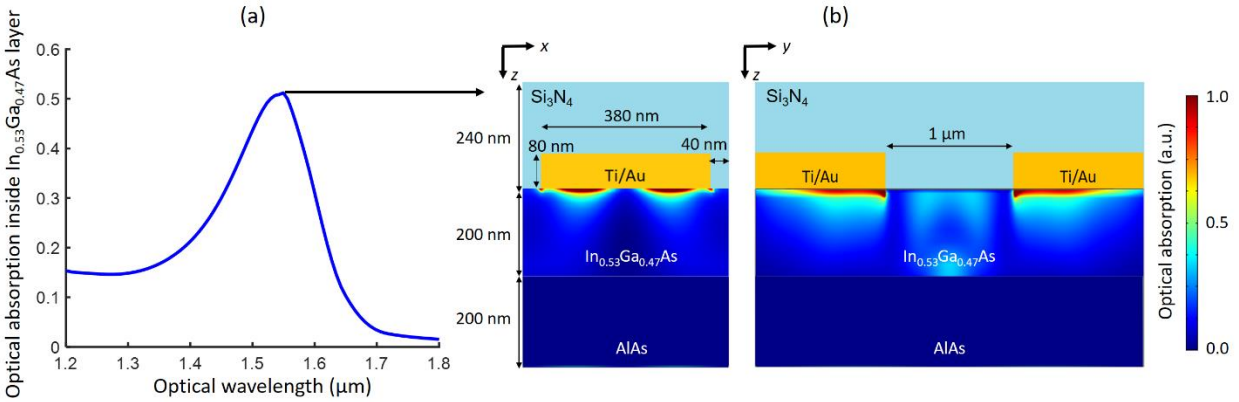

Fig. 2.3: (a) Estimated optical absorption spectrum inside the 200 nm $In_{0.53}Ga_{0.47}As$ layer using Lumerical. (b) Estimated optical absorption profile in the *x*-*z* and *y*-*z* cross-sections of the substrate.

To investigate the effect of the tip-to-tip gap between the plasmonic contact electrode gratings on the detector performance, the impact of the gap size on the induced terahertz voltage at the input port of the logarithmic spiral antenna, the induced terahertz electric field and optical absorption inside the $In_{0.53}Ga_{0.47}As$ layer is analyzed. Figures 2.4a and 2.4b show the estimated induced voltage and electric field distribution across the antenna terminals, by using two numerical software packages based on the finite element method (HFSS and COMSOL, respectively). Figure 2.4c shows the estimated optical absorption across the antenna terminals for a TM-polarized optical excitation at a 1550 nm wavelength with a $1/e^2$ diameter of 2 µm along the y-axis, by using Lumerical. The induced electric field and optical absorption are both enhanced at the tip of the antenna terminals, especially when the tip-to-tip gap between the plasmonic contact electrode

gratings is reduced. Therefore, higher responsivity values are expected for detectors utilizing smaller tip-to-tip gap sizes with the drawback of a steeper responsivity roll-off at higher terahertz frequencies. In addition, detectors with smaller gap sizes are more susceptible to carrier screening and bleaching and hence, output saturation at lower optical powers due to the generation and separation of a larger number of electrons and holes within a smaller volume. Considering these performance tradeoffs, we choose detectors with 0.5 and 1 µm tip-to-tip gap sizes for further experimental characterization.

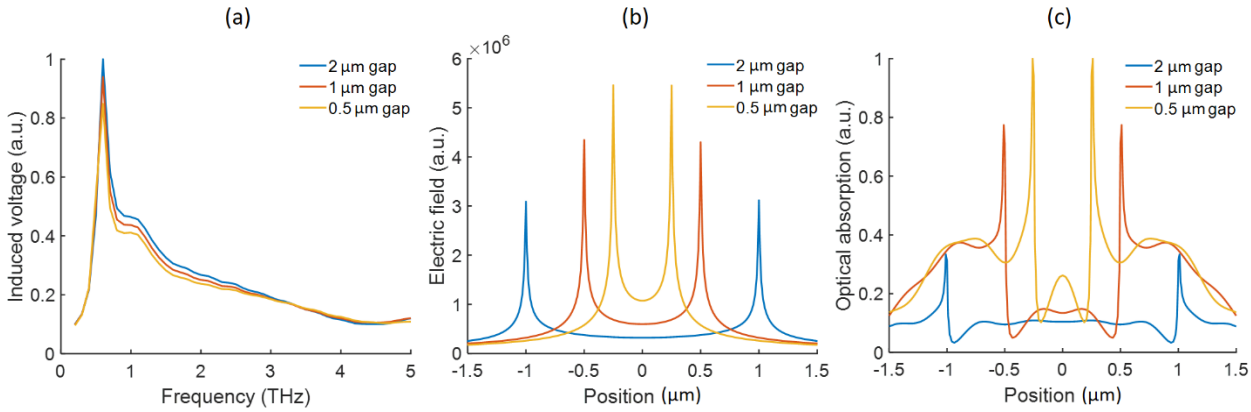

Fig. 2.4: (a) Estimated induced voltage across the antenna terminals for tip-to-tip gap sizes of 0.5, 1, and 2 µm as a function of frequency. (b) Induced electric field intensity at 0.6 THz and (c) optical absorption across the antenna gap at a 5 nm depth below the $In_{0.53}Ga_{0.47}As$ surface.

In order to have a strong overlap between the optical generation profile and the induced terahertz field across the antenna terminals, the optimum optical beam shape should be a narrow ellipse that covers the entire gap between the two plasmonic contact electrodes and is tightly confined around the grating tips. Such a tight optical focus would result in a high optical intensity, leading to possible optical absorption bleaching as the photocarriers fill up the limited available states inside the $In_{0.53}Ga_{0.47}As$ layer. To further investigate how this bleaching effect could impact our detector performance, we use Lumerical to estimate the optical intensity profile inside the $In_{0.53}Ga_{0.47}As$ layer, for an elliptical optical beam spot with 2 µm (the minimum achievable spot

size with our objective lens) and 10 μm $1/e^2$ diameters along the y-axis and x-axis, respectively, and calculate the bleaching threshold. The bleaching threshold is reached when the number of absorbed photons per unit volume is equal to the total density of states of $In_{0.53}Ga_{0.47}As$ that can be filled by absorbed 1550 nm photons, which is ~10^{17} cm^{-3}. Figure 2.5 shows the estimated number of absorbed photons per unit volume at a 190 nm depth inside the $In_{0.53}Ga_{0.47}As$ layer at optical power levels ranging from 0.01 mW to 10 mW. The areas where bleaching occurs are clearly shown in light yellow. Since the optical intensity drops as the depth increases, the bleached areas close to the bottom of the $In_{0.53}Ga_{0.47}As$ layer provide a very good assessment of the extent of bleaching. No bleaching is observed at a 0.01 mW optical power for both 0.5-μm-gap and 1-μm-gap detectors. When the optical power is increased to ~0.1 mW, small, bleached areas are spotted at the tip-to-tip gap between the plasmonic contact electrodes, which experiences the highest optical intensity. As the optical power is increased from 0.1 mW to 1 mW, a substantial part of the active area is bleached for both detectors. Therefore, we expect the detector output to be significantly saturated at optical powers beyond 1 mW, which is supported by our experimental results.

The optical and scanning electron microscopy images of a fabricated detector prototype are shown in Fig. 2.6. The fabrication process starts with electron-beam lithography (EBL) patterning, electron-beam evaporation of 3/77 nm Ti/Au, and liftoff to realize the plasmonic contact electrodes. Next, the $In_{0.53}Ga_{0.47}As$ layer is dry etched by using Cl_2/Ar chemistry with the plasmonic electrodes masked by a maN-2405 electron-beam resist. The 240-nm-thick Si_3N_4 ARC is then deposited globally using plasma-enhanced chemical vapor deposition. Then, contact vias at the edge of both plasmonic electrodes are patterned by optical lithography and opened by CHF_3/O_2 reactive ion etching chemistry. Finally, the logarithmic spiral antenna and bonding pads

are patterned by optical lithography followed by 50/550 nm Ti/Au deposition and liftoff. The fabricated terahertz detector prototypes are mounted on hyper-hemispherical silicon lenses to better focus the incident terahertz radiation onto the device active area.

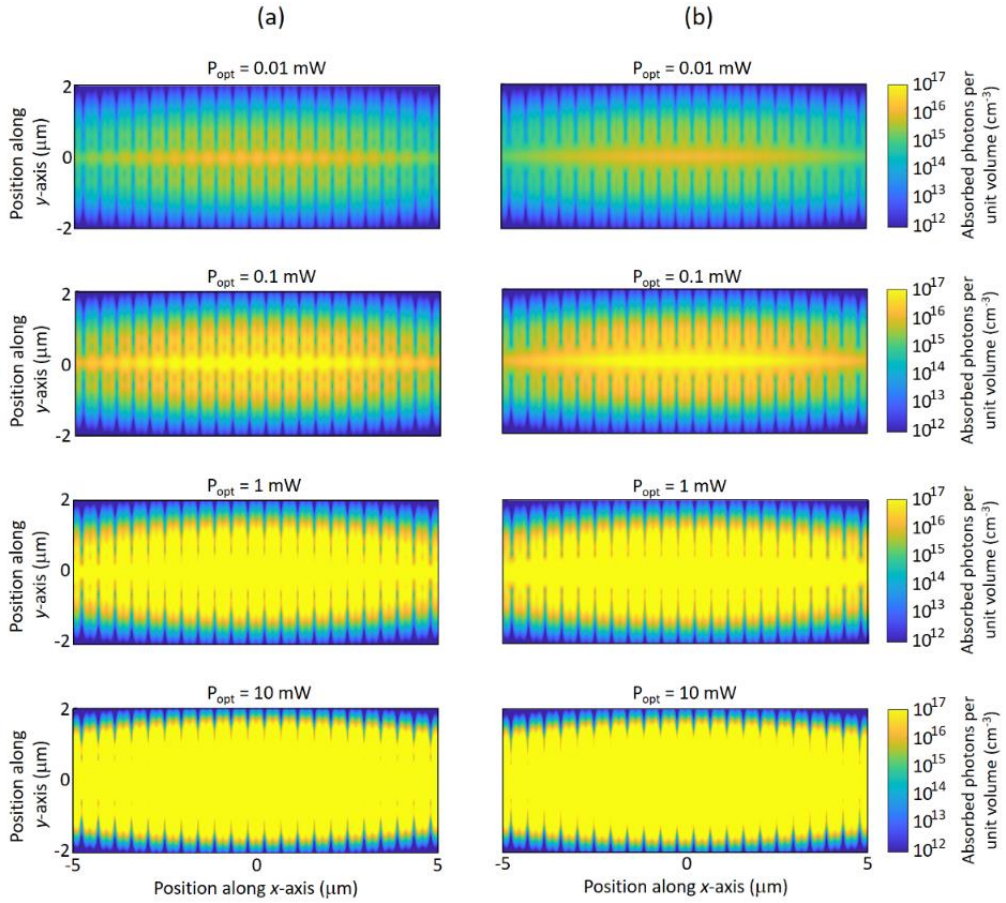

Fig. 2.5: The estimated number of absorbed photons per unit volume at a 190 nm depth inside the $In_{0.53}Ga_{0.47}As$ layer at optical powers levels ranging from 0.01 mW to 10 mW for the 0.5-µm-gap and 1-µm-gap detectors are shown in (a) and (b), respectively. The areas where bleaching occurs are shown in light yellow.

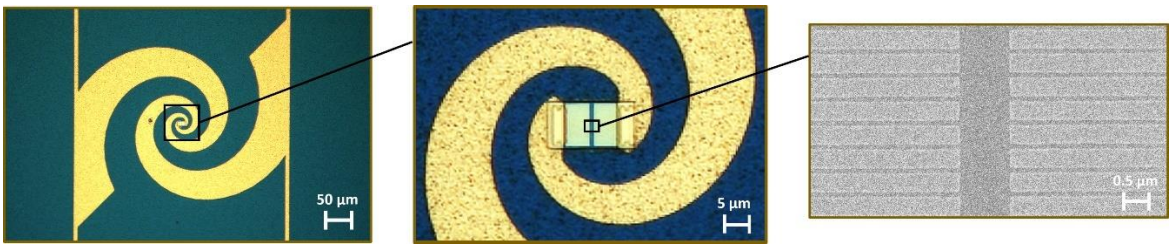

Fig. 2.6: The optical microscopy image of a fabricated detector prototype and the scanning electron microscopy image of the plasmonic contact electrodes at the center of the detector.

2.1.3. Experimental Results

Characterization of the terahertz detector prototypes is performed using a THz-TDS system with an optical parametric oscillator, which converts femtosecond pulses from a Ti-Sapphire laser (Coherent Mira HP) to femtosecond pulses at ~1550 nm center wavelength with a 190 fs pulse-width and a 76 MHz repetition rate. The laser is split into two branches to pump a terahertz source and probe the terahertz detector prototypes, respectively. A motorized delay stage is used to control the time-delay between the pump and probe beams. An InAs-based bias-free nanoantenna array is used as the terahertz source [135]. The combination of a cylindrical lens and a 100x objective lens is used to focus the optical probe beam down to a narrow elliptical spot with 2 μm and 10 μm $1/e^2$ diameters to cover the entire gap between the two plasmonic contact electrodes. The output photocurrent of the characterized detectors is amplified using a transimpedance amplifier (FEMTO DLPCA). The amplified signal is acquired while varying the time-delays between the optical pump and probe beams to resolve the time-domain terahertz field. The detected spectrum is obtained by calculating the Fourier transform of the time-domain data.

Figure 2.7 shows the obtained time-domain terahertz waveforms and the corresponding power spectra of the 1-μm-gap detector under 1 mW, 3 mW and 5 mW optical probe power levels at an average terahertz power of 206 μW. 10 time-domain traces are captured and averaged to obtain these results. As predicted by our numerical analysis, a strong saturation in the detector output is observed when the optical probe power exceeds 3 mW, at which most of the available states in the 200-nm-thick $In_{0.53}Ga_{0.47}As$ layer are occupied by photocarriers, limiting further increase in the induced photocurrent.

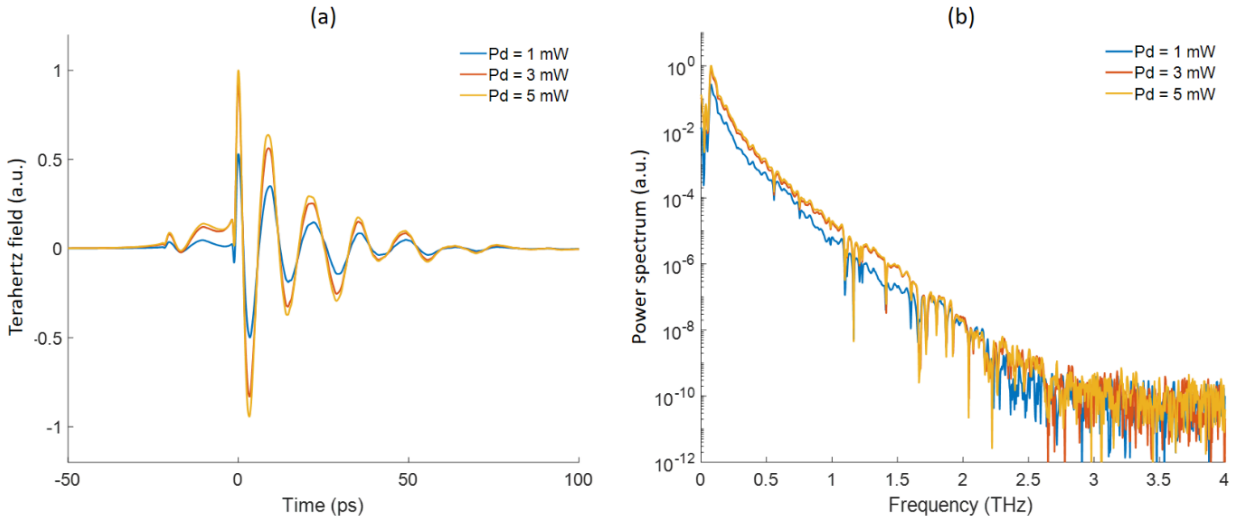

Fig. 2.7: (a) Time-domain terahertz waveforms and (b) the corresponding power spectra obtained by the 1-µm-gap detector under 1 mW, 3 mW and 5 mW optical probe power levels at a terahertz power of 206 µW. 10 time-domain traces are captured and averaged to obtain these results.

Figure 2.8 shows the obtained time-domain terahertz waveforms and the corresponding power spectra of the 1-µm-gap and 0.5-µm-gap detectors under a 5 mW optical probe power and 206 µW average terahertz power. 10 time-domain traces are captured and averaged to obtain these results. A comparison between the power spectra clearly shows a stronger roll-off in the frequency response of the 0.5-µm-gap detector, which is explained by the larger capacitive loading to the antenna when a 0.5 µm gap between the plasmonic contact electrodes is used. Since the detector resistance under illumination is much larger than the antenna radiation resistance, the RC time constant of these detectors is determined by the radiation resistance and parasitic capacitance. While the antennas of both detectors have the same radiation resistance, the estimated capacitance between the plasmonic contact electrodes for gap sizes of 0.5 µm and 1 µm is 1.53 fF and 1.27 fF, respectively. The slightly lower responsivity of the 0.5-µm-gap detector is attributed to a more severe carrier screening due to the stronger optical intensity enhancement and the separation of a larger number of electrons and holes in the active area of this detector.

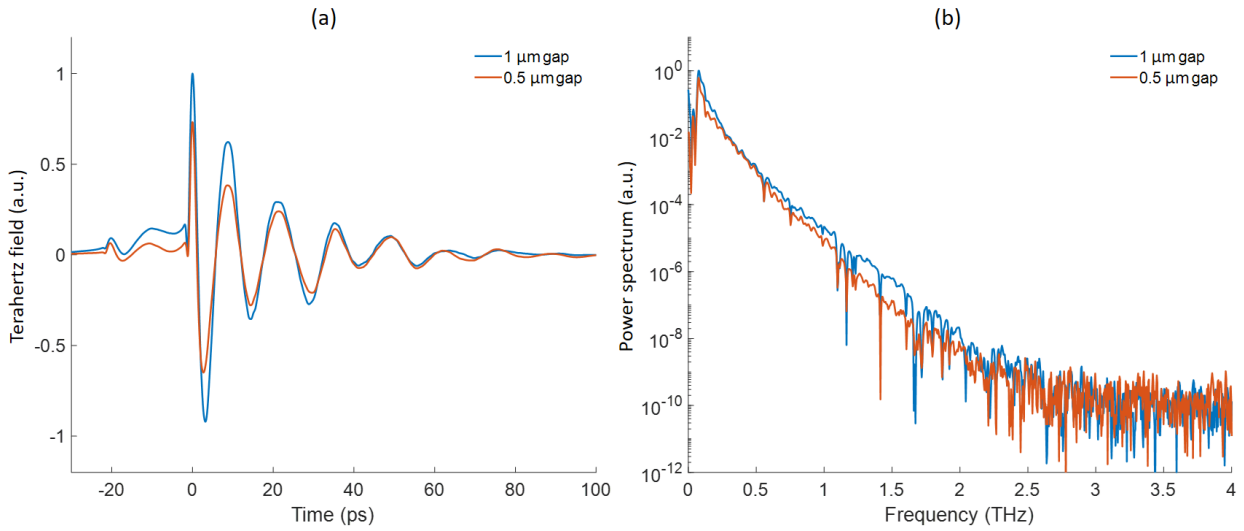

Fig. 2.8: (a) Time-domain terahertz waveforms and (b) the corresponding power spectra obtained by the 0.5-µm-gap and 1-µm-gap detectors under a 5 mW optical probe power and 206 µW terahertz power. 10 time-domain traces are captured and averaged to obtain these results.

The peak terahertz field, noise power, and SNR obtained by the 1-µm-gap and 0.5-µm-gap detectors under different probe power levels are shown in Fig. 2.9. As expected by our theoretical analysis, the output signal from both detectors saturates when increasing the optical probe power due to bleaching and carrier screening. However, the output of the 0.5-µm-gap detector is saturated at a lower optical probe power due to a stronger carrier screening and bleaching in the device active area, leading to a slightly lower responsivity offered by this detector (Fig. 2.9a). Since the detector noise is dominated by the Johnson-Nyquist noise, the measured noise power of both detectors shows a linear dependence on the optical probe power (Fig. 2.9b). The 0.5-µm-gap detector has two times higher noise power levels compared to the 1-µm-gap detector since its resistance is approximately half of the 1-µm-gap detector. As predicted by the measured peak terahertz field and noise power values, the measured SNR saturates when increasing the optical probe power for both detectors and higher SNR levels are offered by the 1-µm-gap detector (Fig. 2.9c). The maximum SNR values of 102 dB and 97 dB are achieved at 5 mW and 10 mW optical probe

powers for the 0.5-μm-gap and 1-μm-gap detectors, respectively. For these SNR measurements 10 time-domain traces are captured and averaged.

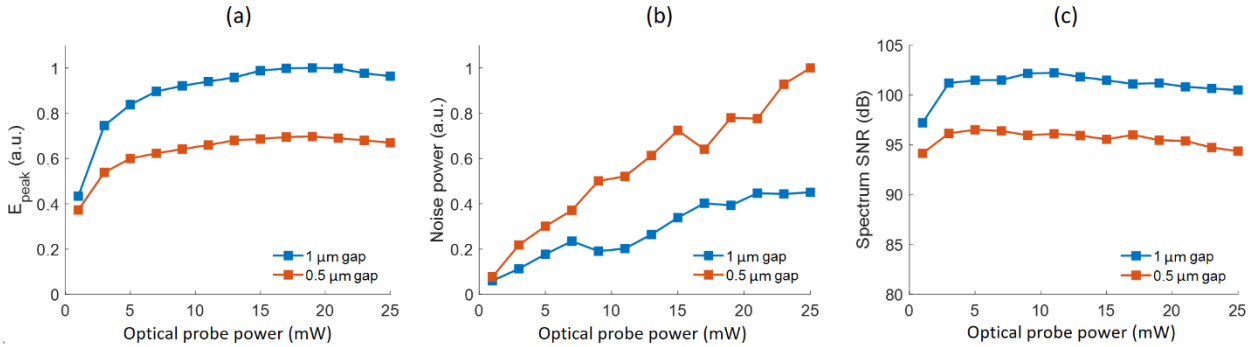

Fig. 2.9: The measured (a) peak terahertz field, (b) noise power, and (c) spectrum SNR as a function of the optical probe power for the 0.5-μm-gap and 1-μm-gap detectors. 10 time-domain traces are captured and averaged for the SNR measurements.

To further enhance the SNR, we increase the number of the time-domain traces that are captured and averaged to obtain the SNR. Figure 2.10 shows the resolved power spectra by the 1-μm-gap detector when changing the number of the time-domain traces from 10 to 1000, corresponding to 4 s to 400 s data acquisition time. As expected, increasing the number of traces reduces the noise power, leading to higher SNR and bandwidth. As clearly shown in Fig. 2.10, the noise level is reduced by 10 dB for every 10x increase in the number of traces, resulting in an SNR increase from 102 dB to 122 dB when increasing the data acquisition time from 4 s to 400 s. More than a 3.6 THz of detection bandwidth is achieved, as confirmed by the concurrence of the experimentally detected spectral dips and water vapor absorption lines taken from the HITRAN database [136]. It should be mentioned that the achieved bandwidth is limited by the pulse-width of the optical beam used to pump/probe the terahertz source/detector in the THz-TDS system and hence, broader detection bandwidths would be achieved when using shorter optical pulse-widths.

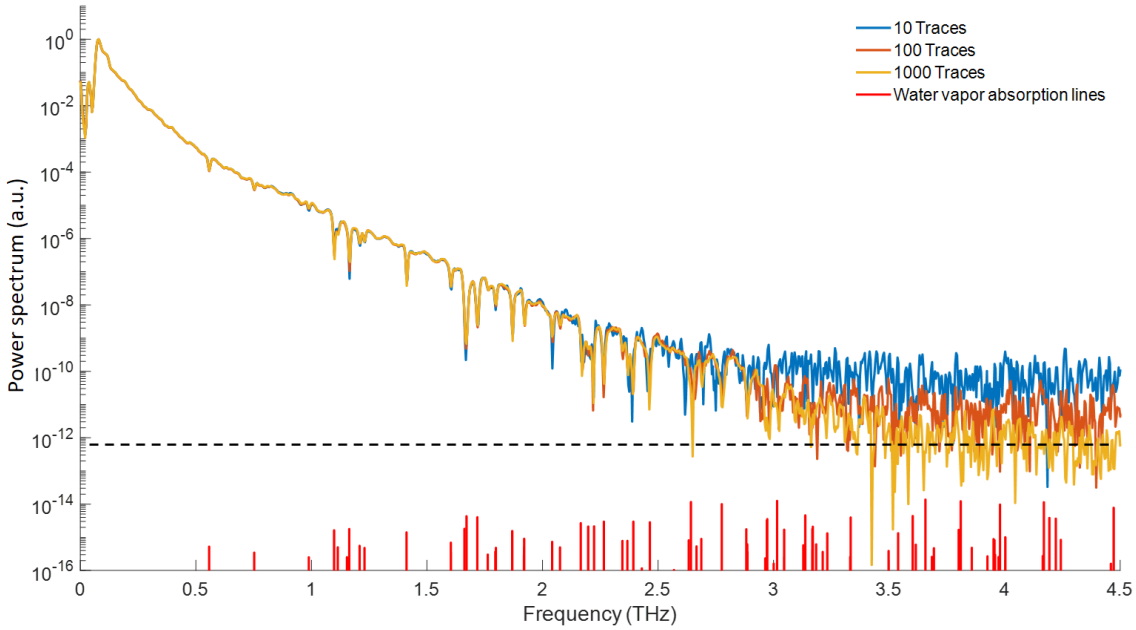

Fig. 2.10: The resolved power spectra by the 1-μm-gap detector when changing the number of the time-domain traces that are captured and averaged to obtain the spectra.

Table 2.1 shows a comparison between the performance of the demonstrated terahertz detector and state-of-the-art photoconductive detectors operating at ~1550 nm wavelength based on short-carrier-lifetime substrates, including InGaAs/InAlAs multilayer heterostructures, transition-metal-doped InGaAs, and ErAs:InGaAs. The demonstrated terahertz detector offers much higher SNR levels compared with the state-of-the-art, while requiring lower optical probe powers. This enhancement in SNR is partly due to the use of plasmonic contact electrodes, which enhance carrier concentration near the antenna terminals, and partly due to the absence of a short-carrier-lifetime photoconductor, which boosts the responsivity by reducing carrier recombination and increasing carrier mobility. On the other hand, the demonstrated terahertz detector provides a narrower detection bandwidth compared with the state-of-the-art. This reduction in bandwidth is partly due to the larger laser pulse-width used for characterizing the detector. However, the long transit time of the photocarriers generated away from the plasmonic contact electrodes is another

factor that results in this reduced bandwidth. Therefore, the use of an $In_{0.53}Ga_{0.47}As$ layer with a smaller thickness could enhance the detection bandwidth further.

Table 2.1: Terahertz detection performance comparison

Reference	Photoconductive substrate	Laser pulse-width	Optical power	SNR	Bandwidth	Number of traces
[74]	InGaAs/InAlAs MLHS	90 fs	16 mW	82 dB	5.8 THz	1000
[137]	Fe:InGaAs / Rh:InGaAs	90 fs	20 mW	105 dB	6 THz	1000
[67]	ErAs:InGaAs	90 fs	16 mW	85 dB	6.5 THz	2000
This work	Undoped InGaAs	190 fs	10 mW	122 dB	3.6 THz	1000

In summary, we introduce a telecommunication-compatible plasmonic photoconductive terahertz detector that utilizes short carrier transit time, instead of short carrier lifetime, to offer high responsivity levels. A photoconductor with plasmonic contact electrodes integrated with a broadband logarithmic spiral antenna is used to offer highly concentrated optical generation around the tips of the contact electrodes, where a strong overlap with the induced terahertz field is achieved, to provide an ultrashort transit time for most of the photo-generated carriers. Therefore, this terahertz detector architecture eliminates the need for a short-carrier-lifetime photoconductor. Hence, a long-carrier-lifetime and high mobility semiconductor can be used as the photoconductive substrate to offer high responsivity levels by reducing carrier recombination and increasing carrier mobility. We demonstrate terahertz detection with a record-high SNR of 122 dB and a 3.6 THz bandwidth when using an optical wavelength of 1550 nm, probe power of 10 mW, and pulse-width of 190 fs. The terahertz detection bandwidth could be increased by the use of shorter optical pulse-widths. In addition, reducing the $In_{0.53}Ga_{0.47}As$ layer thickness could also enhance the terahertz detection bandwidth, while having a negligible impact on the SNR since the optical absorption is tightly confined near the plasmonic contact electrodes. Furthermore, reducing the $In_{0.53}Ga_{0.47}As$ layer would reduce the Johnson-Nyquist noise as a result of an increase in the device resistance. Importantly, this work introduces a generic and reliable approach for designing

photoconductive terahertz detectors that utilize various semiconductors and optical wavelengths, without being limited by the availability of short-carrier-lifetime photoconductors.

2.2. Continuous-Wave Operation of Terahertz Photoconductive Antennas Utilizing Carrier Transit Time Reduction

2.2.1. Background

To generate and detect CW terahertz radiations, two CW lasers with their frequency difference in the terahertz range are used to excite the PCA. It is crucial to have the polarization of the lasers aligned in the same direction so that the superposition of the two laser beams creates a terahertz envelope. Since a terahertz frequency is created from two optical frequencies, the PCAs operating in CW mode are usually called photomixers.

To analyze the terahertz beatnote generated through photomixing, we assume that the phasor electric fields of the two lasers at ω_1 and ω_2 angular frequencies are given by

$$E_1 = |E_1|e^{j(\omega_1 t+\phi_1)} \tag{2.1}$$

$$E_2 = |E_2|e^{j(\omega_2 t+\phi_2)} \tag{2.2}$$

where ϕ_1 and ϕ_2 are the phases of the laser electric fields. When the heterodyning optical pump beam is incident on the photomixer, the induced photocurrent is proportional to the squared magnitude of the total phasor field given by

$$\begin{aligned} |E_{total}|^2 = |E_1 + E_2|^2 &= |E_1|^2 + |E_2|^2 + E_1E_2^* + E_2E_1^* \\ &= |E_1|^2 + |E_2|^2 + 2|E_1||E_2|\cos\left[(\omega_2 - \omega_1)t - (\phi_2 - \phi_1)\right] \end{aligned} \tag{2.3}$$

Therefore, as it can be seen from Eqn. 2.3, the induced photocurrent consists of a DC component and the desired terahertz oscillation at $\omega_{THz} = |\omega_2 - \omega_1|$. An important observation from the above equation is that at a fixed total optical power, the maximum photomixing efficiency is obtained when the two lasers have the same electric field amplitudes, i.e. $|E_1| = |E_2|$. Therefore, it is essential to keep the powers of the two lasers identical to achieve the largest terahertz photocurrent and the highest photomixing efficiency.

A major advantage of CW terahertz generation and detection through photomixing is the high frequency resolution offered by CW signals. Thanks to the advancements in laser technology, frequency tunable lasers are readily available at various wavelengths, enabled by either temperature tuning or mechanical tuning. Only a modest frequency tuning range is required for terahertz applications. For example, at around 1550 nm optical wavelength, a wavelength detuning of only 8 nm for the heterodyning optical pump would offer a 1 THz frequency tunability.

With the same logarithmic spiral antenna design presented in Section 2.1, we successfully demonstrate CW generation and detection in a THz-FDS system that utilizes a fixed CW laser and a wavelength-swept laser to generate the terahertz beatnotes pumping the terahertz source and detector, as detailed in the following sections. Importantly, this is the very first demonstration of short-carrier-lifetime-photoconductor-free PCAs for CW operation, which validates the effectiveness of plasmonics-enabled transit time reduction for ultrafast photocarrier transport.

2.2.2. Frequency-Domain Spectroscopy Using Linearly Swept Laser

In a THz-FDS system, an oscillating carrier concentration is generated by photomixing two laser beams separated by a terahertz frequency at the source and detector for the generation and detection of terahertz radiations, respectively. To modulate the detector signal and allow for lock-

in detection, an optical phase modulator is typically used to periodically sweep the terahertz phase difference between the source and detector branches from -π to π [138-140]. As a result, the detector output photocurrent will be modulated sinusoidally, enabling a highly sensitive readout by a lock-in amplifier at each discrete terahertz beat frequency.

It was recently shown that this active phase modulator can be eliminated using a delayed self-heterodyning (DSH) scheme, leading to simpler system configuration yet with much faster scan rate (> 24 Hz) [141]. Self-heterodyning refers to the cases that the same pair of CW lasers are used to excite both the source and detector, but with a nonzero frequency difference between their terahertz beatnotes. The schematic of the DSH THz-FDS system is shown in Fig. 2.11a. A static laser (Santec TSL-510) is combined with a swept laser (Finisar WaveSource^{TM}) to generate linear sweeping of the terahertz beat frequency. After that, the combined lasers are amplified by an Erbium-doped fiber amplifier (EDFA) and split into a pump beam and probe beam for the excitation of the terahertz source and terahertz detector, respectively. An intentional imbalance of fiber length is introduced in the probe branch to induce an extra time delay such that as the photomixing occurs at the terahertz detector, there exists a constant frequency difference f_0 between the received terahertz wave and the detector beatnote. In other words, the terahertz wave is downconverted to an intermediate frequency (IF) equal to f_0, which can be demodulated during data post-processing using a software-based lock-in amplifier. As shown in Fig. 2.11b, since the terahertz beat frequency is swept linearly, it is clear that f_0 and the time delay ΔT are related by the terahertz frequency sweep rate,

$$f_0 = \Delta T * \frac{df_{THz}}{dt}, \tag{2.4}$$

where $f_{THz}(t)$ denotes the instantaneous terahertz beat frequency. For optimal performance, ΔT should be chosen such that f_0 is high enough to avoid $1/f$ noise and acoustic noise at low frequencies, while ensuring ΔT to be much smaller than the coherence time of the swept laser (typically around tens of nanosecond) so that the terahertz detector beatnote and the received terahertz wave always remain coherent. Therefore, with $df_{THz}/dt = 0.5\,GHz/\mu s$ for the WaveSource swept laser, we use $\Delta T \approx 1\,ns$ to obtain $f_0 \approx 500\,kHz$.

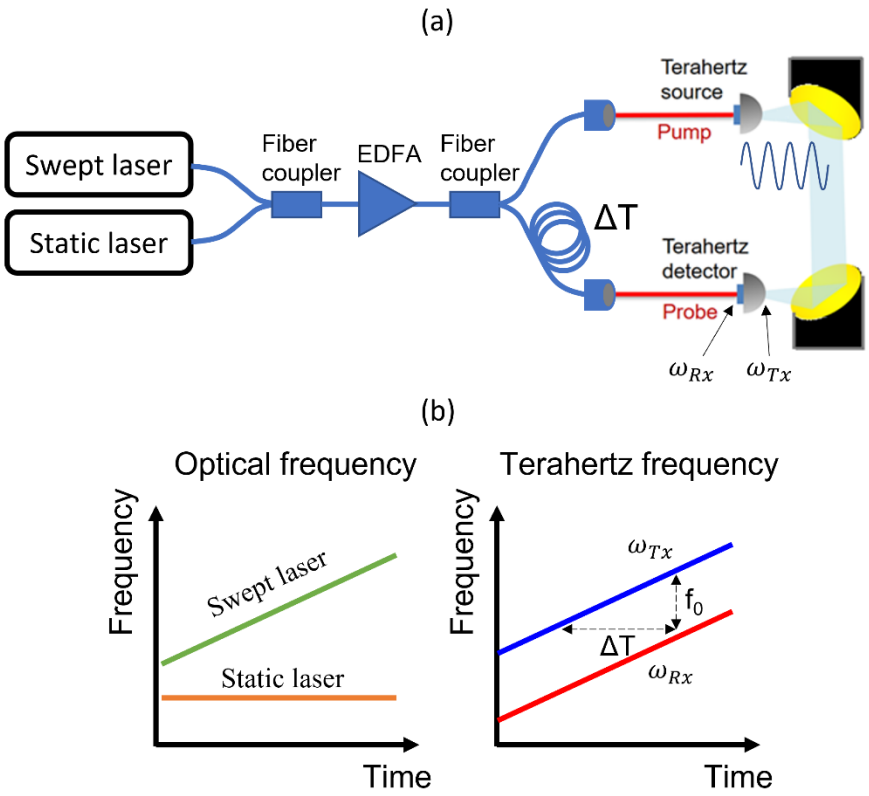

Fig. 2.11: (a) The schematic of the delayed self-heterodyning THz-FDS system that uses a static laser and a linearly swept laser as the optical sources. (b) Illustration of the optical frequencies (left) as well as the terahertz beatnote frequencies (right) as a function of time, showing a linear sweeping.

2.2.3. Experimental Results

To validate the DSH THz-FDS system, we first use a commercial PIN-diode-based terahertz emitter (Toptica PCA-FD-1550-100-TX) as the source and the plasmonic logarithmic spiral

antenna as the detector. The fiber-coupled PIN emitter is biased at -1.5 V and pumped with 30 mW optical power to offer terahertz power levels of > 100 µW at 100 GHz, and > 1 µW at 1 THz. The output photocurrent from the detector is first amplified by a transimpedance amplifier (FEMTO DHPCA-100 at 10^4 V/A gain) before being digitized by a data acquisition card (AlazarTech ATS660). Using a software-based lock-in detection algorithm, the raw data is post-processed to obtain the terahertz power spectrum through several steps, including invalid data removal where laser mode transition occurs, IF estimation, multiplication by exp $(j2\pi f_0 t)$, low-pass filtering, and ensemble averaging.

Figure 2.12 shows the measured raw data and the terahertz power spectrum obtained by averaging 1000 traces within a 20 second acquisition time, showing a 1.6 THz radiation bandwidth and 98 dB dynamic range. The dynamic range and radiation bandwidth are further increased to 118 dB and more than 2.5 THz, respectively, when the number of averages is increased to 10^5 (Fig. 2.13). As theoretically expected, for every 10 times increase in the number of averaging, the noise level is reduced 10 times.

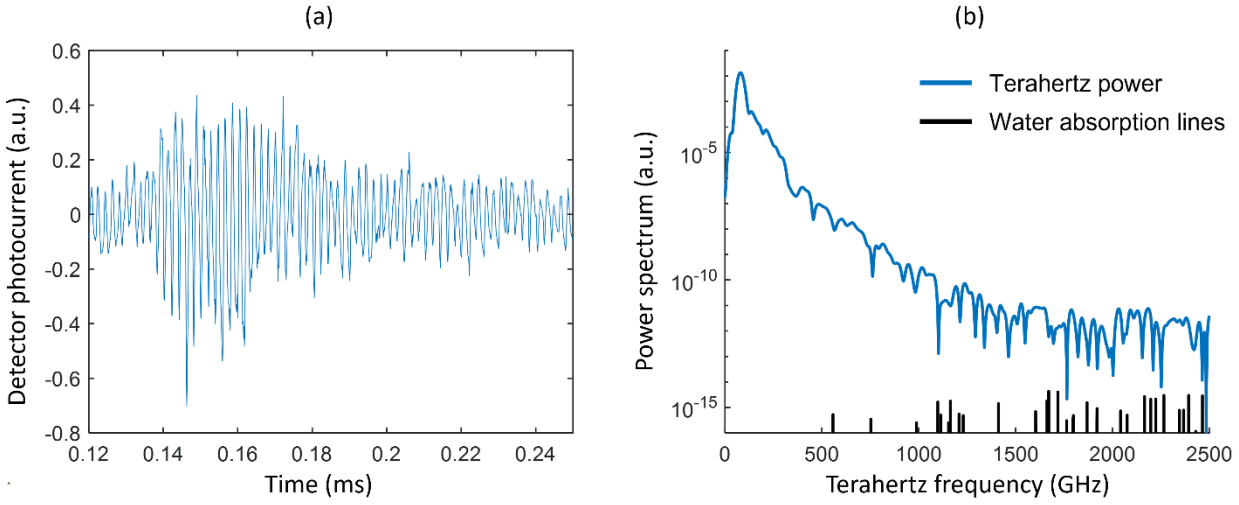

Fig. 2.12: (a) The acquired detector photocurrent before software-based lock-in detection. (b) The power spectrum obtained by averaging 1000 traces within a 20 second acquisition time.

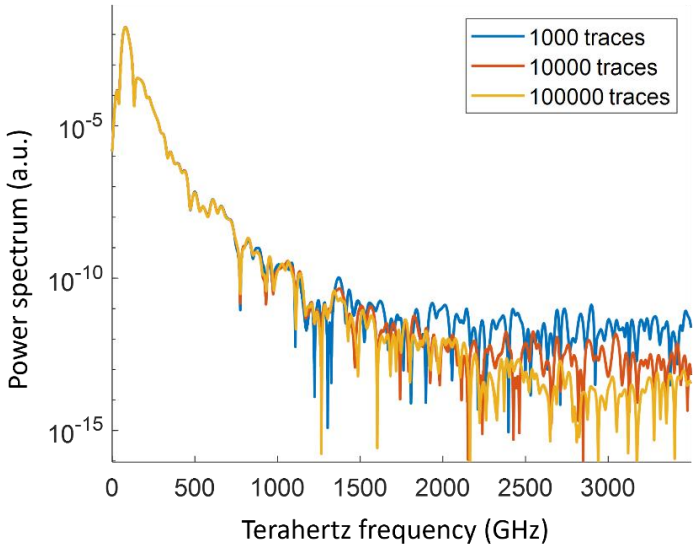

Fig. 2.13: The power spectra obtained by averaging over various number of traces, showing a 10x reduction in noise level for every 10x increase in the number of traces.

To demonstrate a short-carrier-lifetime-photoconductor-free THz-FDS system, we replace the PIN-based terahertz emitter by a plasmonic photoconductive emitter. The emitter uses the same substrate and logarithmic spiral antenna used for the detector, with the difference that the logarithmic spiral antenna is oriented with the opposite handedness relative to that of the detector. To enhance the radiated terahertz power level from the spiral antenna, both the bias voltage and the optical pump beam are modulated with a low duty cycle at 5 MHz. Since the modulated optical beam is effectively sampling the terahertz spectrum (Fig. 2.14), the modulation frequency has to be higher than the Nyquist rate (chosen ~10 times of f_0 in our experiment). Figure 2.15 shows the power spectrum obtained by averaging 10000 traces, showing a 79 dB dynamic range and 2 THz radiation bandwidth.

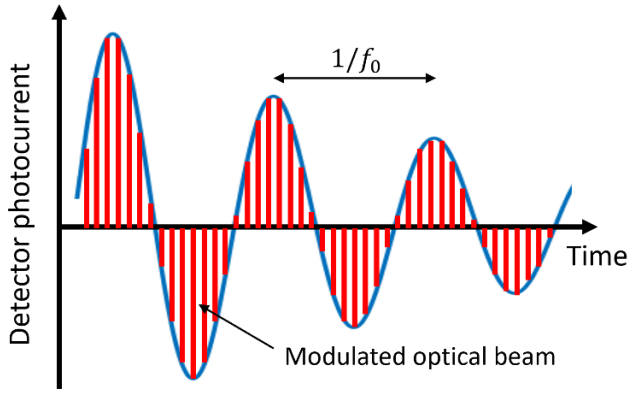

Fig. 2.14: Illustration of the detector output photocurrent for a DSH THz-FDS system with the optical beam modulated under a low duty cycle.

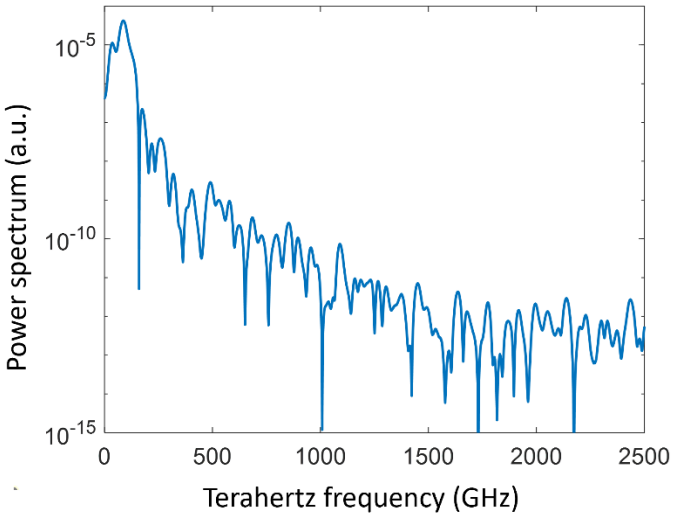

Fig. 2.15: The measured power spectrum using plasmonic photoconductive logarithmic spiral antennas for both the terahertz source and detector, after averaging 10000 traces.

Chapter 3: Plasmonics-Enabled Ultrafast Carrier Dynamics Based on Photoconductor Band Engineering

3.1. Background

It was recently demonstrated that the need for an external bias voltage in a telecommunication-compatible terahertz emitter can be totally eliminated by taking advantage of the strong, naturally-induced built-in electric field inside the photoconductor [91, 129]. This bias-free photoconductive emitter concept is very appealing because it completely removes the undesired leakage current, enabling a highly reliable operation. Among various photoconductors that offer high optical absorption at 1550 nm wavelength, InAs is a very good choice because of its high electron mobility ($> 10^4$ $cm^2/V/s$ at room temperature) as well as the strong Fermi level pinning at the InAs surface, where its Fermi level is fixed above the CB minimum energy. Specifically, a bilayer InAs structure consisting of a 500-nm-thick p+ InAs layer followed by 100-nm-thick undoped InAs layer was epitaxially grown on a SI-GaAs substrate through MBE, where a strong built-in electric field is induced in the undoped InAs layer to accelerate photocarriers for terahertz generation [91]. To further enhance the generated ultrafast photocurrent, a large area plasmonic nanoantenna array designed for 1550 nm excitation was fabricated at the InAs surface to confine the optical generation near the nanoantenna elements, where the strength of the built-in electric field is also maximized. As a result, the average transit time of the accelerated photocarriers to the plasmonic nanoantennas, which also serve as the terahertz radiating elements, is significantly reduced [108,

111, 142, 143], leading to efficient and broadband terahertz radiation with optical-to-terahertz conversion efficiencies exceeding other passive terahertz emitters based on nonlinear optical processes (by 4 orders of magnitude) [144, 145], photo-Dember effect [126, 127], and spintronics [146, 147].

3.2. Silicon-Compatible Bilayer InAs Plasmonic Nanoantenna Arrays

3.2.1. Device Design and Fabrication

As the radiation bandwidth of photoconductive terahertz emitters improve, the impact of terahertz absorption in the substrate becomes more important. In particular, GaAs is known to possess a phonon absorption band beyond 5 THz [148, 149], which limits the transmission of the generated terahertz radiation. Here we present the very first bias-free telecommunication-compatible photoconductive terahertz emitter based on the same bilayer InAs structure directly grown on a high-resistivity silicon substrate. In addition to the compatibility with silicon integrated optoelectronic platforms, the presented bias-free photoconductive emitter provides higher SNR levels at high terahertz frequencies compared to the previously demonstrated GaAs-based bias-free emitters. Through a detailed characterization it is shown that, in addition to higher terahertz transmission, this SNR enhancement is also partially due to a shorter carrier lifetime in the InAs layers grown on silicon, which gives rise to a faster photocurrent response. The reduced carrier lifetime originates from higher defect concentrations as a result of a larger lattice mismatch at the InAs/Si interface, as compared to the InAs/GaAs interface. We demonstrate a bias-free, telecommunication-compatible photoconductive emitter with more than a 6 THz radiation bandwidth which can be integrated with silicon photonic platforms and/or components.

Figure 3.1a illustrates the bias-free plasmonic photoconductive emitter implemented on a high-resistivity (> 5000 Ω·cm) silicon substrate (InAs/Si emitter), where a 500-nm-thick p^+-doped (p = 1.4×10^{19} cm^{-3} Beryllium doping) InAs layer followed by a 100-nm-thick undoped InAs layer are grown using MBE. Thanks to the Fermi level pinning at the InAs surface, where the Fermi energy is fixed above CB [121, 122, 150], a built-in electric field is induced inside the undoped InAs layer. The thickness of the undoped InAs layer and the doping of the p^+-doped InAs layer are engineered to maximize the induced built-in electric field in the undoped InAs layer to enable ultrafast photocarrier transport. In particular, the p^+-doped InAs layer effectively raises the valence band (VB) energy such that it is aligned close to the surface Fermi level, consequently inducing a strong built-in electric field in the undoped InAs layer. More importantly, as shown by the band diagram in Fig. 3.1a, the direction of the induced electric field is such that the photo-generated electrons (rather than holes) are accelerated toward the surface and get collected by the terahertz antenna for terahertz emission. As a result, the higher mobility of electrons ensures a faster photocarrier response and, hence, a broader terahertz radiation bandwidth.

With a strong built-in electric field induced in the 100-nm-thick undoped InAs layer, it is also crucial to maximally confine the optical generation within this region such that most of the photocarriers will be accelerated to high drift velocities, contributing to high-efficiency and broadband terahertz generation. To achieve this goal, the same large-area plasmonic nanoantenna array as reported in Ref. [91] is fabricated on the InAs surface, which is designed to excite surface plasmon waves in response to an incident optical pump beam at ~1550 nm wavelength with a TM polarization. The optimized nanoantenna geometry, which is in the form of metallic gratings, has a 440 nm periodicity, 80 nm gap, 3/97 nm Ti/Au metal height, covered by a 240-nm-thick Si_3N_4 anti-reflection coating. Using an FDTD method-based electromagnetic solver (Lumerical), the

optical absorption profile inside the 100-nm-thick undoped InAs layer is calculated. As illustrated in Fig. 3.1b, optical absorption is maximized at a 1550 nm wavelength, while achieving a strongly enhanced photocarrier concentrations right below each individual nanoantenna elements. This optical absorption profile allows a high photocarrier collection efficiency with a reduced average transport distance and transit time for the photocarriers, enabling the generation of a strong ultrafast photocurrent feeding the plasmonic nanoantenna arrays for high-efficiency and broadband terahertz generation.

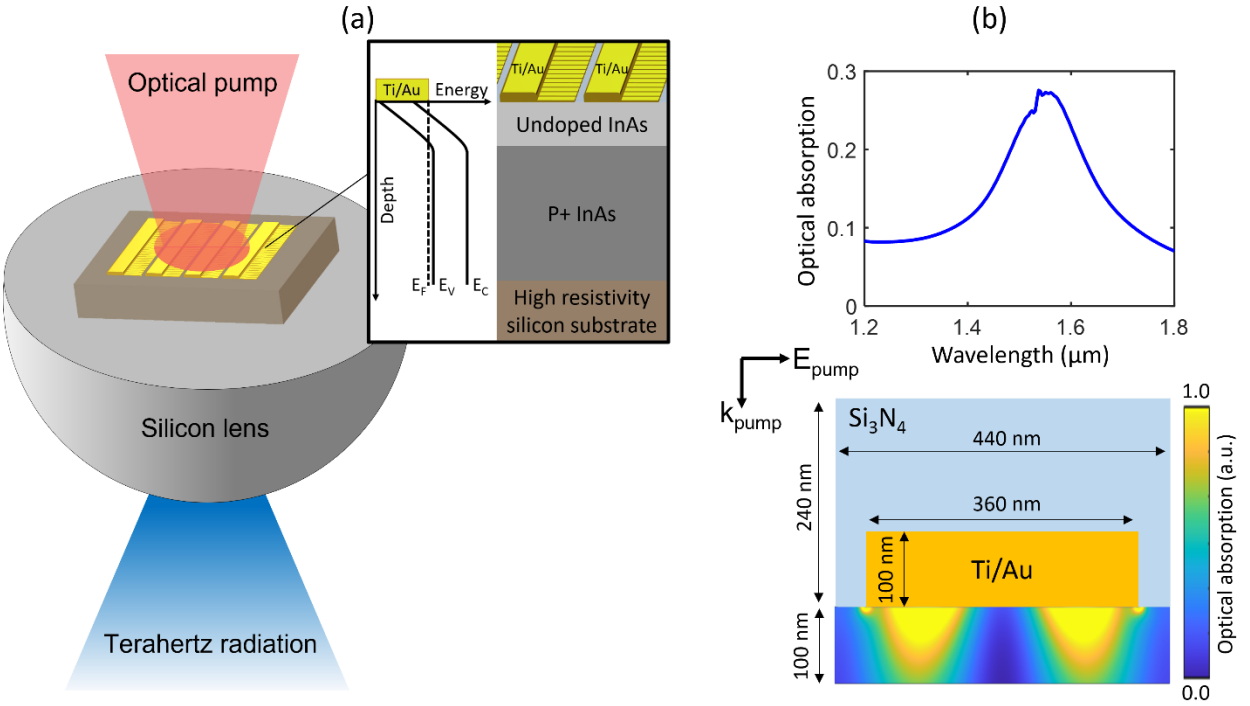

Fig. 3.1: (a) Schematic diagram of the bias-free plasmonic photoconductive emitter implemented on a silicon substrate. Inset shows the band diagram and epitaxial layers directly grown on high-resistivity silicon, which consist of a 500-nm p+-doped InAs layer followed by a 100-nm undoped InAs layer. (b) Optical absorption within the 100-nm-thick undoped InAs layer (top) and the color plot of the optical absorption profile at a 1550 nm incident wavelength, indicating the excitation of surface plasmon waves (bottom).

The fabrication of the bias-free emitter starts with patterning of all nanoantenna elements using EBL, which is followed by a Ti/Au evaporator deposition and lift-off. After this, a second EBL step defines a series of 2-μm-wide ground stripes, followed by a 500-nm-thick Ti/Au deposition

to electrically connect all of the nanoantenna elements on one side. These ground stripes are crucial to ensure a unidirectional flow of all photocurrent elements, leading to a constructive interference of the terahertz field from the entire nanoantenna array in the far field. Finally, the Si_3N_4 anti-reflection coating with a 240 nm thickness is globally deposited using plasma-enhanced chemical vapor deposition. Figure 3.2 shows the optical microscopy and scanning electron microscopy images of a fabricated InAs/Si emitter with a 1 × 1 mm^2 nanoantenna array, where the vertical ground stripes are clearly seen in the middle image.

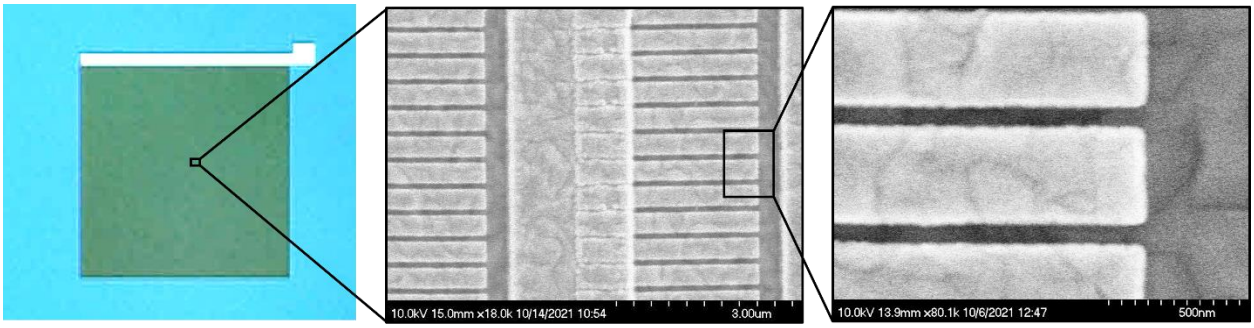

Fig. 3.2: Optical and scanning electron microscopy images of a fabricated bias-free InAs/Si emitter prototype.

3.2.2. Experimental Results

The radiation spectrum of the InAs/Si emitter is characterized using a THz-TDS system and compared to the bias-free bilayer InAs emitter implemented on an SI-GaAs substrate (InAs/GaAs emitter). Two different femtosecond lasers are separately used in our THz-TDS system to examine the impact of the laser parameters on the radiation spectra. The first laser is an optical parametric oscillator (OPO) that converts femtosecond laser pulses from a Ti:Sapphire laser (Coherent Mira HP) into femtosecond laser pulses with a central wavelength of 1550 nm, a 76 MHz repetition rate, and a ~ 225 fs pulsewidth. The second laser is a compact Erbium fiber laser (Toptica FemtoFErb 1560) that emits laser pulses with a central wavelength of 1560 nm, a 100 MHz repetition rate, and a ~ 53 fs pulsewidth. The laser pulses are split into a pump beam and a probe beam in order to

excite the bias-free emitters as well as a photoconductive terahertz detector. The output photocurrent of the detector, which is proportional to the received terahertz electric field, is amplified through a transimpedance amplifier (FEMTO DHPCA-100 at 10^6 V/A gain) before being digitized and recorded.

The time-domain electric field waveforms and their corresponding power spectra under excitation by the OPO laser (at a 450 mW power) and the fiber laser (at a 100 mW power) are shown in Figs. 3.3a-3.3b and Figs. 3.3c-3.3d, respectively. As expected, we see a slower frequency roll-off for the measured spectra using the fiber laser thanks to its shorter optical pulse width. In addition, for both lasers, the InAs/Si emitter shows a slower frequency roll-off, leading to higher SNR levels at high terahertz frequencies. This is partially explained by the difference in the terahertz transmission through the silicon substrate compared to the GaAs substrate. Since silicon is a non-polar semiconductor, its optical phonon absorption is much weaker in the terahertz frequency range compared to GaAs. To quantify the impact of the substrate transmission, we measure the terahertz transmission spectra of bare InAs/Si and InAs/GaAs wafers using THz-TDS and Fourier transform infrared (FTIR) spectroscopy, as shown in Fig. 3.4. The InAs/Si substrate shows a higher terahertz transmission, with ~ 3 dB difference below 4 THz and more than 10 dB above 6 THz. The absorption dip present for both substrates at ~ 6.5 THz corresponds to the optical phonon absorption band of the InAs layers. The terahertz transmission spectra of the substrates explain the difference between the high-frequency portions of the radiated power spectra from the InAs/Si and InAs/GaAs emitters (Figs. 3.3b and 3.3d). However, the InAs/Si emitter consistently shows smaller low-frequency radiation components, suggesting additional mechanisms affecting the generated terahertz radiation.

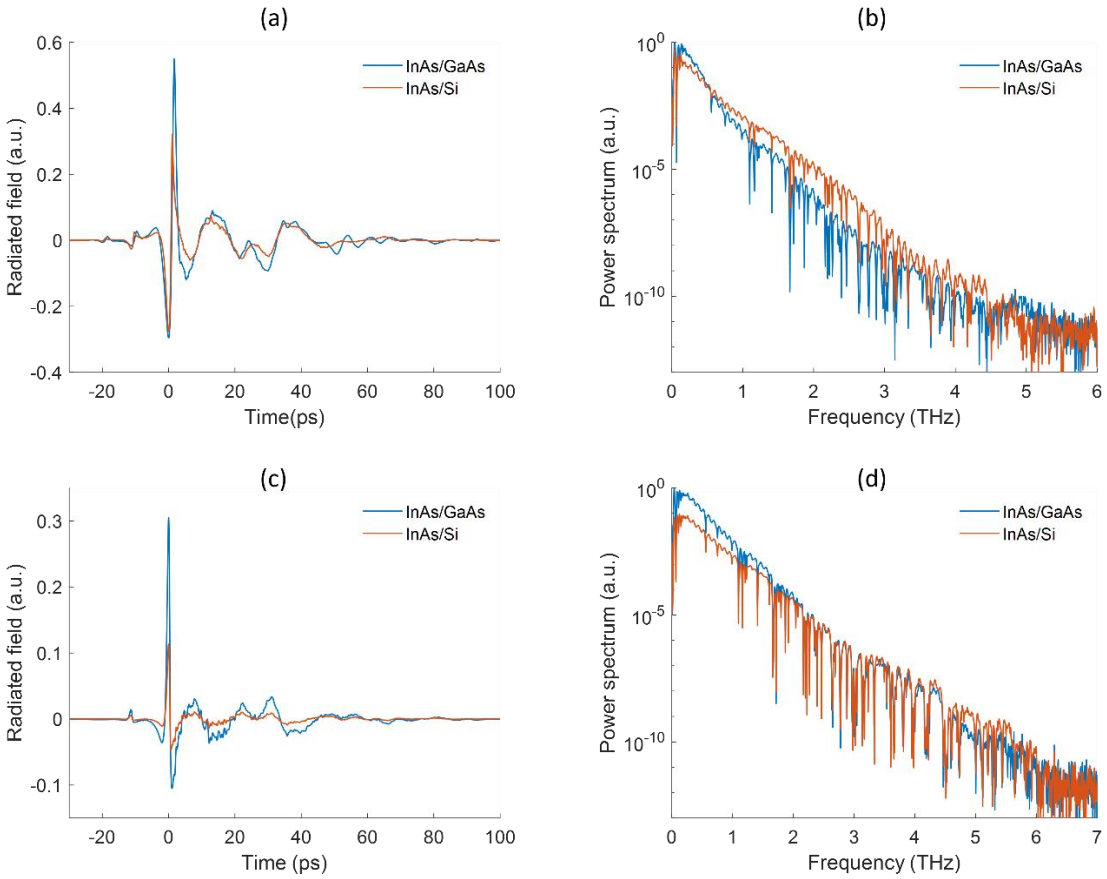

Fig. 3.3: (a) The time-domain electric field waveforms and (b) the radiated power spectra from the InAs/GaAs and InAs/Si emitters under a 450-mW OPO laser excitation. (c) The time-domain electric field waveforms and (d) the radiated power spectra from the InAs/GaAs and InAs/Si emitters under a 100-mW fiber laser excitation.

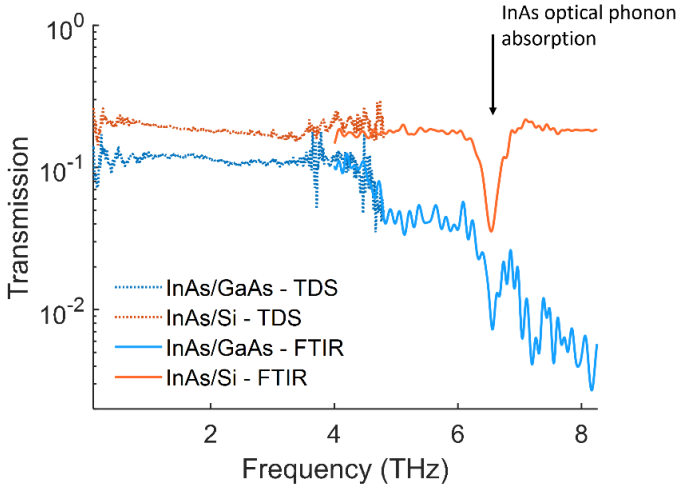

Fig. 3.4: Terahertz transmission spectra through the bare InAs/GaAs and InAs/Si substrates measured using THz-TDS and FTIR, showing a higher transmission for the InAs/Si substrate. An absorption dip around 6.5 THz is present in both substrates, which corresponds to the optical phonon absorption of InAs.

The main cause of the reduced power and the slower frequency roll-off at low terahertz frequencies for the InAs/Si emitter is the shorter carrier lifetime of the InAs layers, which originates from their higher concentration of defects. This is due to a larger lattice mismatch of 11% at the InAs/Si interface, compared to the 7% mismatch at the InAs/GaAs interface. To verify this hypothesis, we characterize the carrier lifetime of InAs in bare InAs/Si and InAs/GaAs substrates through optical-pump terahertz-probe differential transmission measurements. For these measurements, the transmitted terahertz signal modulated by a transient optical excitation is recorded through lock-in detection, while changing the time delay between the optical and terahertz beams. The carrier lifetime is obtained from exponential fitting of the differential transmission decay as a function of time delay. As shown in Fig. 3.5a, the carrier lifetime of InAs in the InAs/GaAs substrate is on the order of several hundred picoseconds (~ 303 ps). On the contrary, the carrier lifetime of InAs in the InAs/Si substrate is ~ 4.5 ps, preventing the drift of the photocarriers with longer transit times to the nanoantenna arrays, leading to the reduction of the low-frequency radiation power and frequency roll-off. The higher defect concentration of the InAs/Si substrate is also supported by surface morphology measurements using atomic force microscopy. As shown in Fig. 3.5b, the surface roughness of the InAs/Si substrate is about 10 times higher than that of the InAs/GaAs substrate, indicating much higher level of disorder in the InAs crystal lattice.

Another important observation from comparing Figs. 3.3b and 3.3d is the difference in the power ratios when pumping the emitters with the OPO and fiber laser. As shown in Fig. 3.3b, the radiated power from the InAs/Si emitter surpasses that of the InAs/GaAs emitter by around 10 dB between 1 THz and 3 THz when using the OPO as the optical pump source. However, Fig. 3.3d shows a considerably lower power ratio when using the fiber laser as the optical pump source. This

difference can be explained by the carrier screening effect. Carrier screening occurs under high photocarrier concentrations since the separated electrons and holes induce an opposing electric field that reduces the built-in electric field of the emitter. As explained in Ref. [26], the strength of the carrier screening can be qualitatively captured by the $\omega_p \tau_s$ product, where τ_s is the momentum scattering time and ω_p is the plasma frequency defined by $\omega_p^2 = nq^2/m^*\varepsilon$, with n being the electron concentration, q the elementary charge, m^* the effective mass, and ε the dielectric permittivity. For $\omega_p \tau_s \gg 1$, the built-in electric field is severely screened with an opposing field on the same order, while for $\omega_p \tau_s \ll 1$, the screening effect is negligible. The combination of the InAs/GaAs emitter with the 450-mW OPO is expected to suffer most from carrier screening because of ~ 6 times higher optical pulse energy as well as a much longer momentum scattering time due to lower-defect InAs layers. On the other hand, the InAs/Si emitter is much more immune to carrier screening for both optical pump sources due to its short momentum scattering time. This leads to a larger power ratio between the InAs/Si and InAs/GaAs emitters under the OPO excitation. This observation points to a subtle relation between the crystal quality and the impact of the carrier screening effect, which will be important for further optimization of the InAs/Si emitter.

To clearly compare the radiation spectra, atmospheric absorption lines are removed by nitrogen-purging the THz-TDS setup. Figure 3.6 shows the measured power spectra when the fiber laser is used as the optical pump source. For these measurements, 10000 time-domain traces are captured and averaged over a total measurement time of 170 minutes. The InAs/Si emitter offers a 6.2 THz radiation bandwidth with more than a 100 dB dynamic range. The unique combination of silicon-compatibility, telecommunication-compatibility, bias-free operation, and broad radiation

bandwidth for the presented InAs/Si emitter makes it highly attractive for a wide range of practical application scenarios.

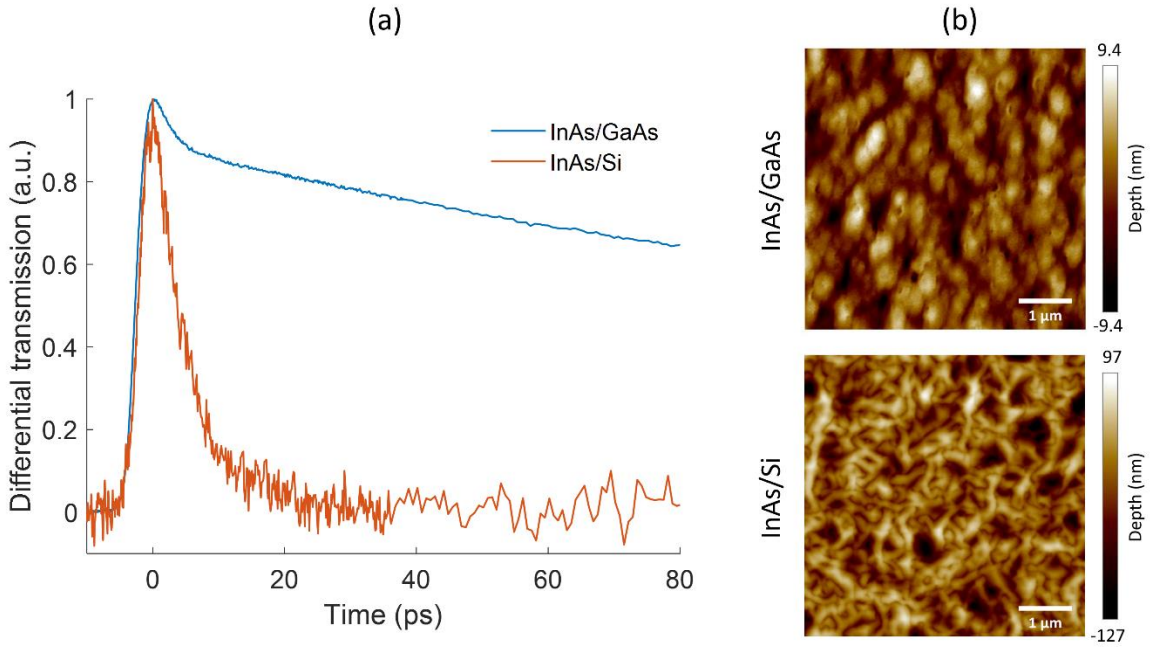

Fig. 3.5: (a) Measured differential terahertz transmission in an optical-pump terahertz probe setup to characterize carrier lifetime of the InAs layers in the InAs/GaAs and InAs/Si substrates. (b) Atomic force microscopy images of the two substrates, showing a much higher surface roughness for the InAs/Si substrate.

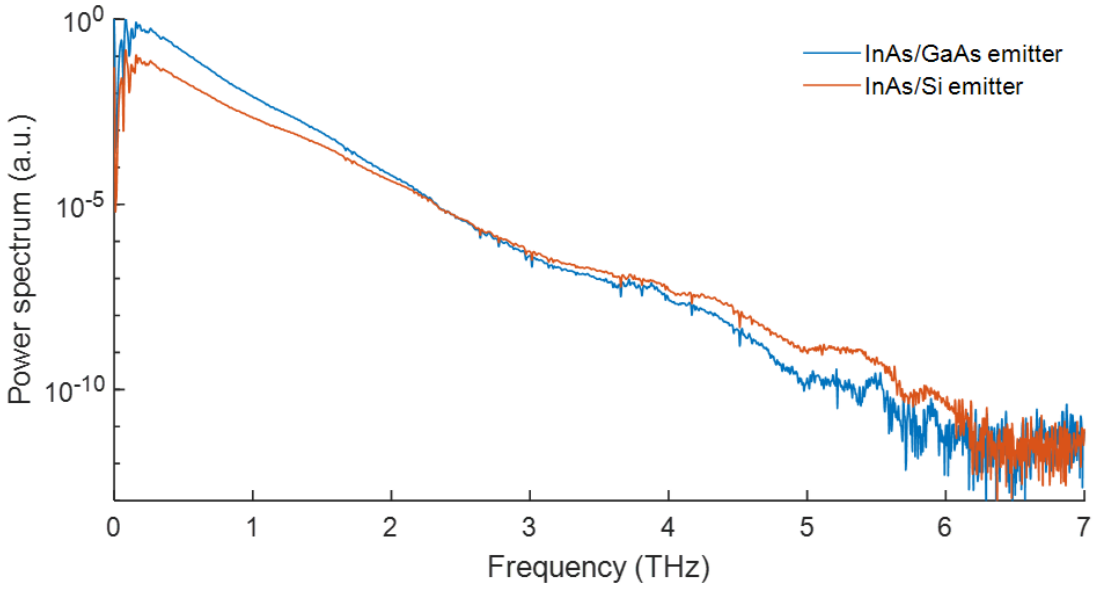

Fig. 3.6: Radiated power spectra of the InAs/GaAs and InAs/Si emitters excited by the fiber laser in a nitrogen-purged THz-TDS setup.

In summary, we demonstrate the first bias-free, telecommunication-compatible photoconductive terahertz emitter realized on a silicon substrate. By epitaxially growing a p^+-doped InAs layer followed by an undoped InAs layer, a strong built-in electric field is induced within the undoped InAs layer thanks to the Fermi level pinning above CB at the InAs surface. This band bending enables bias-free operation of the emitter, leading to a complete removal of the leakage current and, hence, significantly improving the emitter reliability. Implementing the bias-free emitter on a silicon substrate is highly desirable because it allows the integration of the emitter with other silicon photonic platforms, enabling more compact terahertz systems with a wider range of functionalities. Moreover, using a silicon substrate largely suppresses the phonon absorption of terahertz radiation, which causes significant power loss for typical III-V substrates beyond 5 THz. This benefit is clearly observed when comparing the radiation spectra of the InAs/Si and InAs/GaAs emitters. Furthermore, it is observed that the large lattice mismatch at the InAs/Si interface causes a higher defect concentration in the InAs layers, leading to a shorter carrier lifetime. This shorter carrier lifetime explains the reduction/increase of the radiation power in the low/high frequency part of the terahertz spectrum when using the InAs/Si emitter. With the optical generation confined and enhanced by a large-area plasmonic nanoantenna array, the photocarrier transport distance and transit time to the nanoantennas are significantly reduced, resulting in a 6.2 THz radiation bandwidth with more than a 100 dB dynamic range. The broadband and large-dynamic-range terahertz radiation achieved from a platform that is compatible with silicon photonics and fiber optics, make the presented InAs/Si emitter a promising solution for real-world terahertz imaging and sensing applications.

3.3. Graded-Composition InGaAs Plasmonic Nanoantenna Arrays

3.3.1. Device Design and Analysis

Section 3.2 describes terahertz generation from the bilayer InAs structures (bilayer InAs emitter), where the strong built-in electric field within the undoped InAs layer is utilized. However, the built-in electric field drops sharply to almost zero inside the highly doped InAs layer, which means that only a fraction of the photocarriers is accelerated for terahertz generation. To address this limitation, we develop a bias-free photoconductive emitter based on an InGaAs photo-absorbing layer with a linearly graded Indium composition (graded InGaAs emitter). The use of the graded InGaAs layer extends the built-in electric field through the entire InGaAs layer to drift all of the photo-generated carriers to the terahertz radiating elements, leading to the generation of terahertz pulses with ~4 times higher total radiation power while introducing a slight reduction in bandwidth compared to the bilayer InAs emitter. A detailed quantitative analysis is performed to describe and compare the two emitter structures in terms of their carrier dynamics and radiation properties, which is supported by the experimental results. The high radiation power, broad bandwidth, telecommunication compatibility, bias-free and reliable operation of the presented graded InGaAs emitter extend the scope and potential uses of terahertz pulse emitters to practical imaging and sensing applications.

Schematic diagram and operation principles of the graded InGaAs emitter are illustrated in Fig. 3.7. A nanoantenna array is fabricated on a 500-nm-thick, 1.4×10^{19} cm^{-3} Be-doped InGaAs layer grown on a SI-GaAs substrate. The InGaAs layer has a linearly graded Indium composition varying from 60% at the InGaAs/GaAs interface to 100% at the surface. With the VB flattened out due to the p^+ doping, the graded bandgap creates a slope in CB, which induces a built-in electric field that drifts the photo-generated electrons toward the nanoantenna electrodes at the surface.

The geometry of the nanoantennas is chosen to enhance optical intensity near the nanoantennas, where the built-in field strength is maximized, by the excitation of surface plasmon waves. In order to excite surface plasmon waves at ~1550 nm wavelength range, the nanoantennas are designed in the form of gratings with a 440 nm periodicity, 80 nm gap, and 80 nm metal height, covered by a 240-nm-thick Si_3N_4 anti-reflection coating.

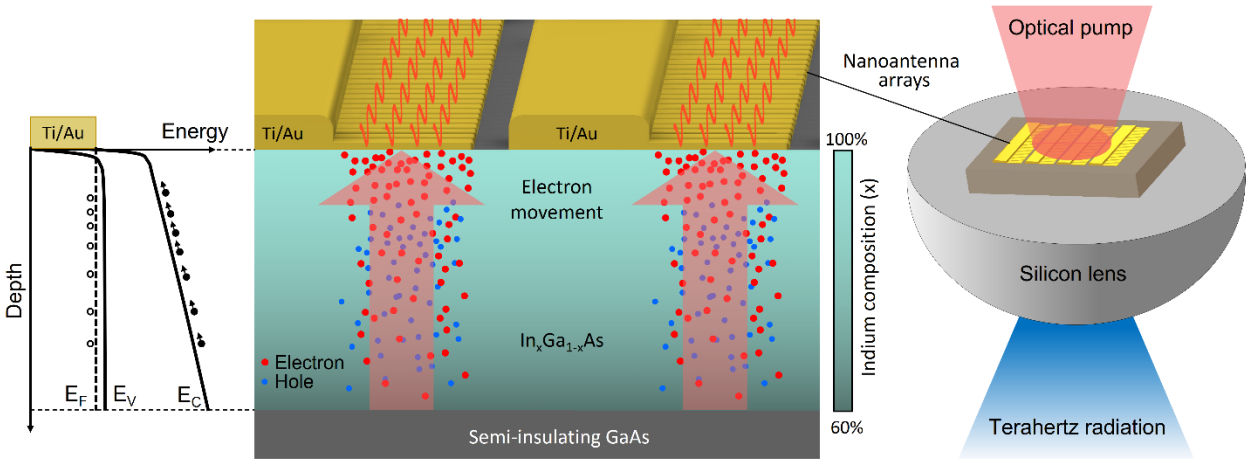

Fig. 3.7: Schematic diagram and operation principles of the graded InGaAs emitter, illustrating the electron movement within the epitaxial graded InGaAs layer toward the nanoantenna array at the surface. Energy band diagram of the graded InGaAs layer is shown on the left, where the Fermi, conduction band minimum, and valence band maximum energy levels are marked as E_F, E_c, and E_v, respectively.

To examine the impact of the Indium composition gradient on the carrier transport, Fig. 3.8 shows the energy band diagrams and CB quasi-electric field profiles of graded InGaAs structures with different starting compositions at the InGaAs/GaAs interface, calculated using a semiconductor device simulator (Sentaurus). It should be noted that the electric force in a semiconductor heterostructure is not only determined by the electric field, but also by the gradient of the electron affinity χ_s and bandgap energy E_g. Therefore, the quasi-electric fields are defined for the CB and VB separately as,

$$F_e = -\frac{dE_c}{dx} = q\frac{dV}{dx} + \frac{d\chi_s}{dx} = -q\mathcal{E}_c^*, \tag{3.1}$$

$$F_h = \frac{dE_v}{dx} = -q\frac{dV}{dx} - \frac{d(\chi_s + E_g)}{dx} = q\mathcal{E}_v^*, \tag{3.2}$$

where F_e, F_h are the electric forces exerted on electrons and holes, E_c, E_v are the CB and VB energies, V is the electrostatic potential, and $\mathcal{E}_c^*, \mathcal{E}_v^*$ are the quasi-electric fields for the CB and VB, respectively. Generally, the quasi-electric fields for the CB and VB can be different. As clearly shown in Fig. 3.8, the p^+ graded InGaAs structure has a non-zero CB quasi-electric field, which depends on the starting Indium composition at the InGaAs/GaAs interface, while the VB quasi-electric field is almost zero except for a ~20 nm depth near the surface. For the starting Indium composition of 60%, the CB quasi-electric field is ~ 6 kV/cm throughout nearly the entire epitaxial structure, which leads to a steady-state drift velocity of ~ 1.5×10^7 cm/s [151-159] (see Section 3.3.3 for more details). Higher composition gradients could potentially lead to stronger built-in quasi-electric fields, but the material quality could be severely degraded by the additional dislocation defects caused by the larger strain in the lattice [160-162]. Therefore, the starting Indium composition of 60% is chosen for the epitaxial growth. As shown in Fig. 3.8, for the pure p^+ InAs structure without any bandgap gradient, the CB quasi-electric field decays rapidly into the substrate, and therefore it will accelerate only a small fraction of the photo-generated electrons within the top 10-20 nm.

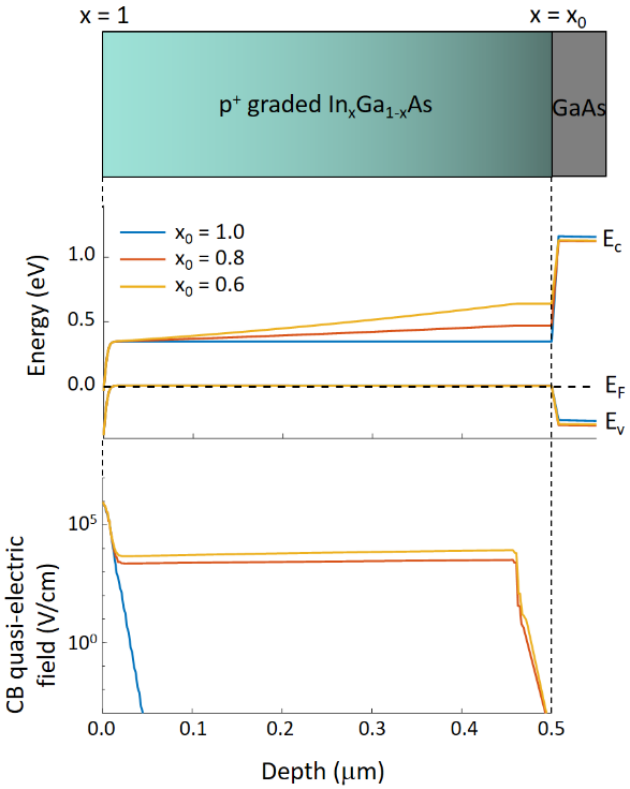

Fig. 3.8: Energy band diagram and CB quasi-electric field of the graded InGaAs semiconductor structure for different starting Indium compositions at the InGaAs/GaAs interface.

To compare the graded InGaAs emitter with the bilayer InAs emitter, Fig. 3.9 shows both of their energy band diagrams and CB quasi-electric field profiles. In contrast to the graded InGaAs structure with its CB quasi-electric field extending throughout the entire photo-absorbing semiconductor region, the bilayer InAs structure has a much stronger field (> 30 kV/cm) which is concentrated within a shallower depth of 100 nm. Importantly, within such a small carrier transport range with minimal defects under a high accelerating field, where scattering events are almost negligible, most of the photo-generated electrons would transport quasi-ballistically. To justify this, we consider the electron mobility in the undoped InAs layer to be 10^4 $cm^2/V/s$ [163] and the scattering time in bulk InAs to be ~130 fs at room temperature [164]. This scattering time is larger than the ballistic transit time for electrons over the 100-nm-thick undoped InAs layer under the uniform field intensity of 30 kV/cm, which is calculated to be 93 fs [165],

$$\tau_{tr} = \sqrt{2m^* L/q\mathcal{E}_c^*}, \tag{3.3}$$

where m^* is the effective mass of electron in bulk InAs and L is the transport distance. As a result, compared to the graded InGaAs structure, the bilayer InAs structure is expected to collect less electrons but with a much higher velocity than the electron saturation velocity, an effect usually termed "velocity overshoot" [166, 167]. After being accelerated for τ_{tr}, the final electron ballistic velocity can be obtained by [165]

$$v_{bal} = q\mathcal{E}_c^*\tau_{tr}/m^*, \tag{3.4}$$

which is the theoretical upper limit of the electron velocity with absolutely no scattering events. To consider all electrons generated at different depths in the substrate, we calculate the weighted average of ballistic velocities using the simulated optical generation profile under the nanoantennas, and obtain 1.3×10^8 cm/s as the theoretical upper limit of the average electron velocity. In reality, a few scattering events could still occur during the transport in addition to the carrier screening that could further reduce the CB quasi-electric field, leading to lower electron velocities. On the other hand, the graded InGaAs structure has much longer carrier transit times compared with the scattering time in InGaAs due to its deeper CB quasi-electric field extension and the high p^+ doping. This suggests that the electron drift velocity will reach its steady-state value within a small fraction of the total transit time. Therefore, we assume that the electrons travel non-ballistically at a steady-state drift velocity of ~ 1.5×10^7 cm/s [151-159].

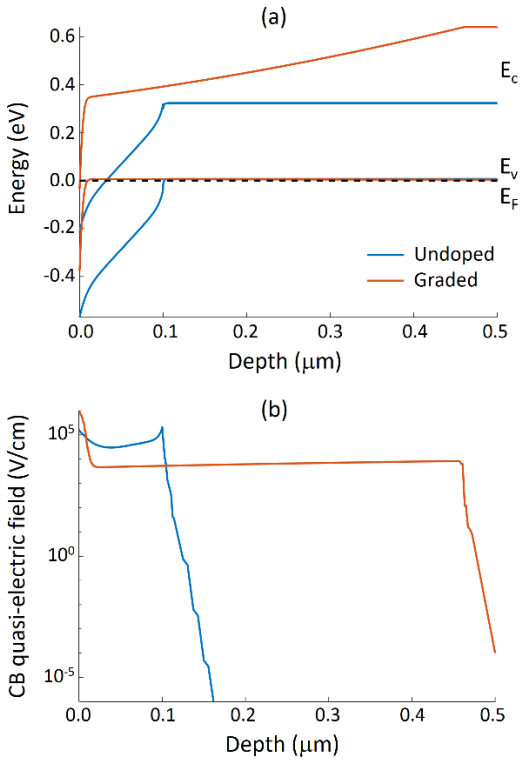

Fig. 3.9: (a) Energy band diagram and (b) CB quasi-electric field of the bilayer InAs and graded InGaAs semiconductor structures, where the bilayer InAs structure is composed of a 500-nm-thick, 1.4×10^{19} cm^{-3} Be-doped InAs layer followed by a 100-nm-thick undoped InAs layer on a semi-insulating GaAs substrate and the graded InGaAs structure is composed of a 500-nm-thick, 1.4×10^{19} cm^{-3} Be-doped InGaAs layer on a semi-insulating GaAs substrate.

An in-depth analysis is performed to calculate the impulse responses of these two substrate structures under a 1550 nm optical excitation to theoretically investigate radiation characteristics of the graded InGaAs and bilayer InAs emitters. We solve the drift-diffusion equation for electrons to obtain the transient electron concentrations over the photoconductive active regions of both semiconductor structures. Since the built-in electric field is normal to the substrate surface, electron movements parallel to the surface are not considered below. Denoting +y axis as the direction into the substrate with y = 0 at the surface, we have

$$\frac{\partial n}{\partial t} = \frac{\partial (v_e n)}{\partial y} + D_n \frac{\partial^2 n}{\partial y^2} - \frac{n}{\tau_e}, \tag{3.5}$$

$$n(y,\ 0) = G_0(y), \tag{3.6}$$

where $n = n(y,t)$ is the electron concentration as a function of position y and time t, v_e is the electron drift velocity, D_n is the electron diffusion constant, τ_e is the electron minority carrier lifetime, and $G_0(y)$ is the optical generation profile, obtained by numerical simulations (Fig. 3.10a). The electron recombination lifetime of the 1.4×10^{19} cm^{-3} Be-doped InAs substrate is experimentally measured to be ~5 ps [91]. Considering the electron diffusion coefficient of $D_n = 1.3 \times 10^{-3}\ m^2/s$ [163, 168], the diffusion term is estimated to be much smaller than the drift term in the undoped InAs region and recombination terms in the p^+ regions of both devices (see more detail in Section 3.3.3). Therefore, the diffusion term is ignored, and the transient electron concentration values are calculated analytically.

For the graded InGaAs structure, considering $v_e = 1.5 \times 10^7\ cm/s$ and $\tau_e = 5\ ps$, the transient electron concentration values are calculated as

$$n(y,\ t) = G_0(y + v_e t)e^{-t/\tau_e}. \tag{3.7}$$

This solution is in the form of a decaying traveling wave in the -y direction toward the electrodes with a speed of v_e. This traveling wave form of solution describes the electron drift under a uniform electric field with an exponential decay due to the electron recombination occurring at the same time.

For the bilayer InAs structure, the electron velocity is modeled as a logistic function of y to take into account the sharp change in velocity between the undoped and doped regions. By considering $\tau_e = 5\ ps$, the solution is

$$n(y,\ t) = \frac{G_0\left(f^{-1}\left(y + v_{bal}t + \frac{1}{k}e^{k(y-w)}\right)\right) \cdot v_e\left(f^{-1}\left(y + v_{bal}t + \frac{1}{k}e^{k(y-w)}\right)\right) \cdot e^{-t/\tau_e}}{v_e(y)} \quad (3.8)$$

where v_{bal} is the average ballistic velocity in the undoped region, $w = 100\ nm$ is the depth of the undoped region, k is the factor that controls the sharpness of the velocity drop, which is taken to be 0.1 nm^{-1}, $v_e(y) = v_{bal}/(1 + e^{k(y-w)})$, and $f(y) = y + e^{k(y-w)}/k$. The solution converges to the same form as for the graded InGaAs structure when y is within the undoped region far enough from the undoped/p+ interface,

$$n(y,\ t) \sim G_0(y + v_{bal}t)e^{-t/\tau_e}, for\ y \ll w. \quad (3.9)$$

Figures 3.10b and 3.10c show the time evolution of the electron concentration solutions under the same incident optical intensities for the bilayer InAs (assuming $v_{bal} = 1.3 \times 10^8\ cm/s$) and graded InGaAs semiconductor structures with a time resolution of 50 fs at the depth cross section with the highest optical generation (monitor lines shown in Fig. 3.10a). Under higher quasi-electric field and ballistic transport, the electrons in the undoped region of the bilayer InAs structure are rapidly swept out to the nanoantenna electrodes, leaving the rest of the electrons in the p^+ region to be recombined with a lifetime of 5 ps. The dramatic behavior changes from undoped to p^+ doped region is clearly observed in Fig. 3.10b. In contrast, the graded InGaAs structure (Fig. 3.10c) shows a smooth reduction of electron concentration caused by both the drift current and carrier recombination. Moreover, it can be seen that the deeper electrons are collected more effectively compared to the bilayer InAs structure due to the CB quasi-electric field extending over almost the entire InGaAs layer, suggesting an increase in the low frequency radiation components.

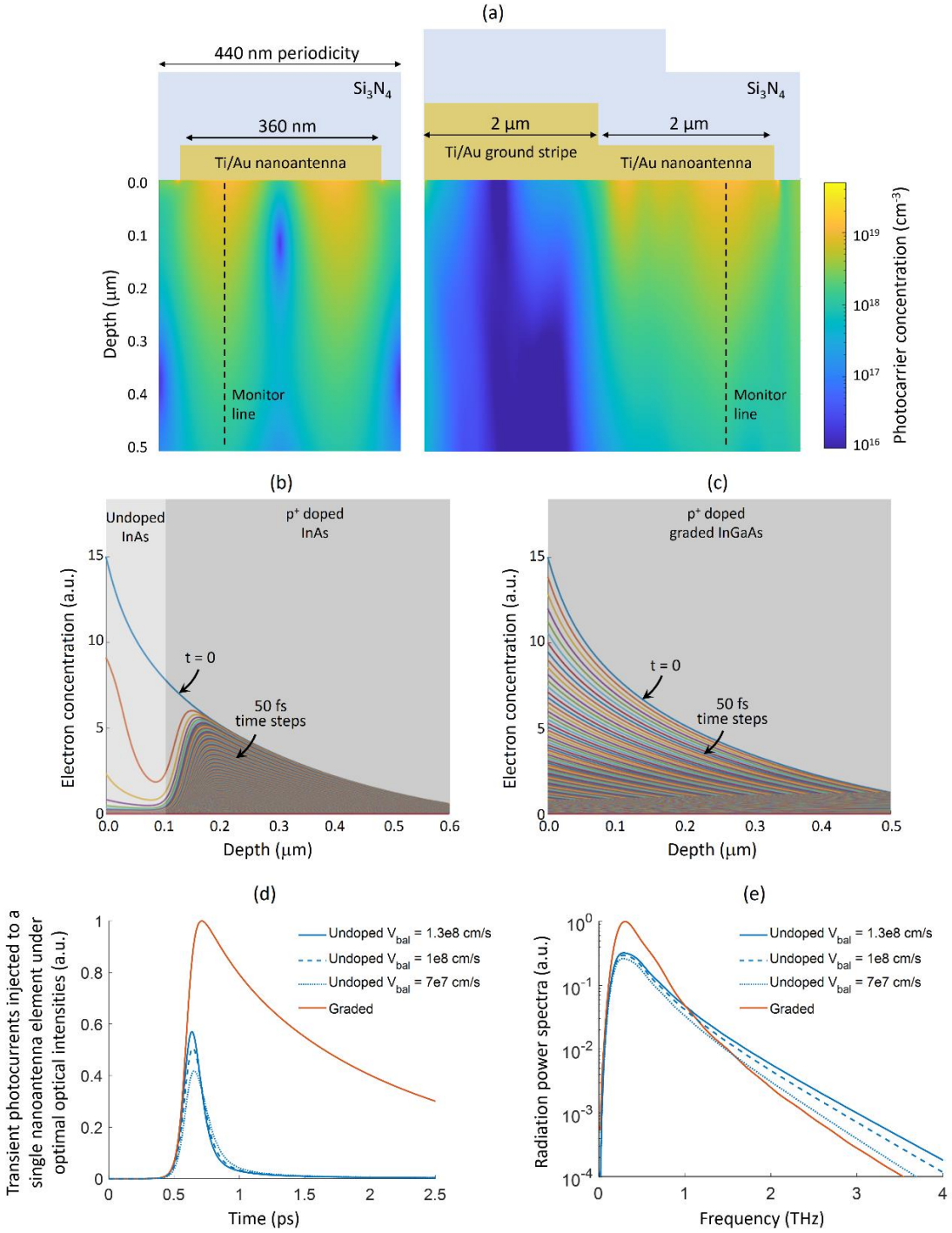

Fig. 3.10: (a) Peak photocarrier concentration generated within the photoconductive active region at an average optical power of 900 mW (assuming a 120 fs pulsewidth and a 76 MHz repetition rate) calculated using a finite-difference-time-domain-based electromagnetic solver (Lumerical). Cross-sections perpendicular to (left) and in parallel with (right) the nanoantenna orientation are shown, where the dashed monitor lines show the position with the highest photocarrier concentration. (b) Calculated impulse response of electron concentration for the bilayer InAs emitter with a 50 fs time resolution, assuming $v_{bal} = 1.3 \times 10^8\ cm/s$. (c) Calculated impulse response of electron concentration

for the graded InGaAs emitter with a 50 fs time resolution. (d) Calculated transient photocurrents injected to a single nanoantenna element for the bilayer InAs emitter (under various ballistic velocities) and graded InGaAs emitter for a laser pulsewidth of 120 fs. (e) Calculated power spectra generated by the entire nanoantenna arrays of the bilayer InAs and graded InGaAs emitters.

Using the calculated impulse response of electron concentration, the impulse response of the injected photocurrent to the nanoantennas fabricated on the bilayer InAs and graded InGaAs semiconductor structures is calculated. Since both structures are terminated with a high-conductivity InAs layer (with surface Fermi level pinning above the conduction band), the nanoantenna metal - InAs junctions are expected to have very low contact resistance and negligible energy barrier for electrons (Ohmic contact). An important difference between the bilayer InAs and graded InGaAs emitters is their experimentally observed optimal optical beam sizes ($1/e^2$ beam diameter of 330 μm and 100 μm for the bilayer InAs emitter and graded InGaAs emitter, respectively) at which they provide the highest radiation power. This difference is attributed to weaker carrier screening in the graded InGaAs emitter due to its flat valence band, leading to negligible hole accumulation within the active region. Carrier screening of the electric field originates from the presence of high carrier concentrations, which create an opposing electric field that consequently reduces the acceleration of the carriers and the radiation power. Different optical beam sizes translate to different incident optical intensity levels under the same optical power. Figure 3.10d shows the transient photocurrents injected to a single antenna element at the optimum optical intensity for both emitters calculated by convolving the impulse response photocurrents with the temporal profile of a 120 fs sech^2-shaped laser pulse used for the experimental characterization. The calculated transient photocurrents for the bilayer InAs structure are plotted for different ballistic velocities because screening of the built-in electric field as a result of the photocarrier drift as well as a small number of scattering events could lower the actual electron velocity in the undoped InAs region. Higher ballistic velocity in the undoped InAs region leads to

sharper transient response, which in the frequency-domain translates to a slower frequency roll-off (Fig. 3.10e). Figure 3.10e shows the estimated power spectra generated by the two emitters obtained by calculating the emitted radiation from the entire nanoantenna array (see more detail in Section 3.3.3). Compared to the bilayer InAs structure, the large photocurrent decay time of the graded InGaAs structure provides stronger sub-terahertz radiation power at a cost of slightly faster frequency roll-off since electrons generated deeper in the InGaAs layer drift to the nanoantennas. The results of this quantitative analysis agree very well with the experimental results discussed in the next section.

3.3.2. Experimental Results

Emitters with the same nanoantenna geometry as described in [91] and a total active area of 1 × 1 mm^2 are fabricated on the graded InGaAs semiconductor structures grown through MBE. Each nanoantenna element has a length of 2 μm to maintain a high-efficiency and broadband radiation performance [91]. The ground stripes have a 2 μm width and a 0.5 μm gap size from the adjacent nanoantenna tips. Fabrication of the emitter prototypes starts with EBL and Ti/Au deposition to form the nanoantenna array as well as the ground stripes sequentially. The 240-nm-thick Si_3N_4 anti-reflection coating is deposited next through plasma-enhanced chemical vapor deposition. Figure 3.11a shows the optical and scanning electron microscopy images of a graded InGaAs emitter prototype.

A graded InGaAs emitter prototype is mounted on a hyper-hemispherical silicon lens to better collimate the generated terahertz radiation. The radiated power spectrum of the emitter is characterized using a THz-TDS system, where an optical parametric oscillator pumped by a Ti:Sapphire laser (Coherent Mira HP) generates femtosecond pulses at a 76 MHz repetition rate, with a 120 fs pulse-width and a center wavelength of ~ 1550 nm. A beam splitter separates the

optical beam into two branches for the excitation of the emitter and an H-dipole-based PCA detector fabricated on an ErAs:InGaAs substrate [67]. While changing the time delay between the two branches, the detector output photocurrent is amplified using a transimpedance amplifier (FEMTO DHPCA-100 at 10^6 V/A gain) and recorded, signifying the time-domain terahertz waveform, as shown in Fig. 3.11b. Since the radiated electric field is proportional to the time derivative of the transient photocurrent, the negative cycle of the sub-picosecond terahertz pulses radiated by the graded InGaAs emitter is significantly lower than the positive cycle due to the long photocurrent decay time predicted in Fig. 3.10d. Through Fourier transform of the time-domain waveform, the radiated power spectrum is obtained (Fig. 3.11c), showing a radiation bandwidth larger than 3 THz when capturing and averaging only 10 traces over a 5 second data acquisition time. It should be noted that the H-dipole-based PCA detector used for our measurements exhibits a resonant behavior at low frequencies, which results in ringing in the detected spectrum. The low frequency resonances are also observed in the measured time-domain electric field. The broad bandwidth of the generated radiation is due to the sub-picosecond rising edge of the generated pulses, which provides high frequency radiation components.

The total radiated power from the emitter is measured using a calibrated pyroelectric detector (Sensors und Lasertechnik THz-30 detector calibrated by Physikalisch-Technische Bundesanstalt, Germany). Terahertz pulses with 860 μW average power are generated at an average optical pump power of 900 mW, exhibiting ~4 times higher radiation power compared to the bilayer InAs emitter [91], which is in agreement with the theoretical predictions shown in Fig. 3.10e. This is the highest reported radiation power compared with the previously demonstrated telecommunication-compatible photoconductive terahertz pulse emitters [69, 71, 73, 123-125]. The radiation power of the graded InGaAs emitter increases super-linearly as a function of the optical pump power with

no signs of saturation, suggesting even higher radiation power and efficiency at higher optical pump powers. While the dominant radiation mechanism relies on the electron drift current feeding the nanoantennas, there could be other secondary mechanisms such as photo-Dember effect and nonlinear optical processes contributing to the generated terahertz power.

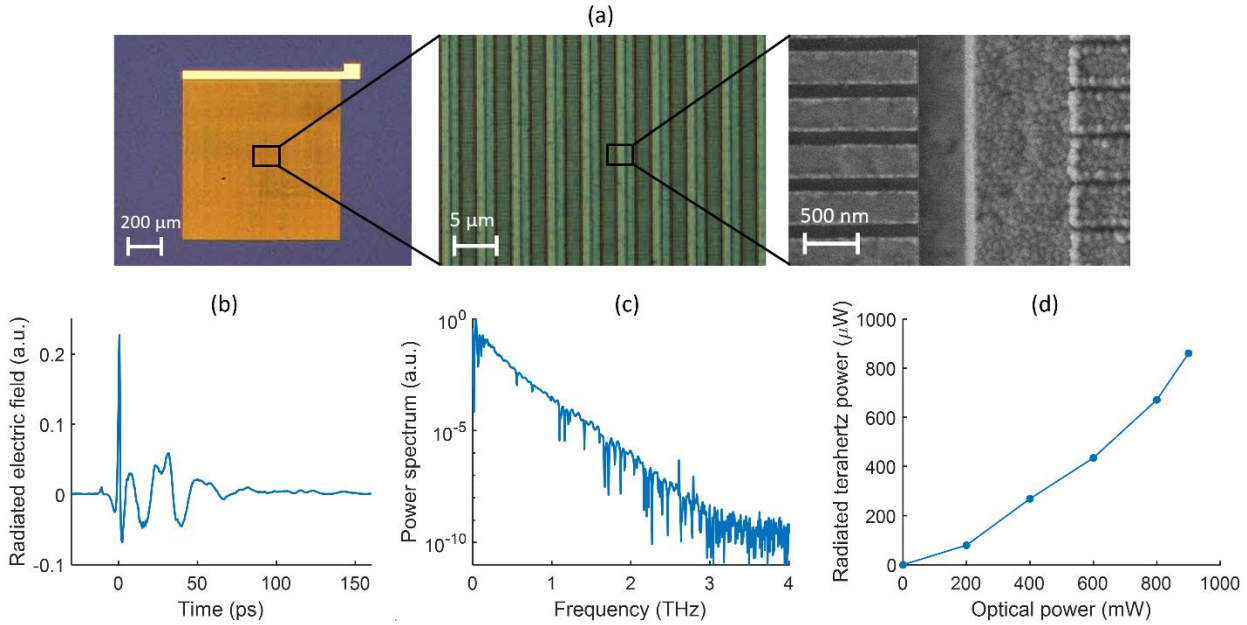

Fig. 3.11: (a) Optical and scanning electron microscopy images of a fabricated graded InGaAs emitter prototype. (b) The measured terahertz time-domain electric field, (c) radiated power spectrum, and (d) total radiated power of the graded InGaAs emitter prototype. (b) and (c) are measured under an average optical power of 450 mW.

As mentioned earlier, the optimal diameter of the optical beam incident on the graded InGaAs emitter under pulsed operation is experimentally determined to be ~100 µm. To further investigate the impact of the optical beam size, we characterize the emitter when generating quasi-CW terahertz radiation at different frequencies as a function of the optical excitation intensity. The optical beam from two C-band CW lasers (Santec TSL-510 and QPhotonics QDFBLD-1550-10) are combined in a fiber and pulse-modulated at a 1 MHz frequency with a 10% duty cycle using an acousto-optic modulator (Gooch & Housego R15200-.2-1.55-GaP-FO-GH). The modulated beam is then amplified to an average optical power of 300 mW using an Erbium-doped fiber

amplifier (HPFA-C-33-IA). Photomixing of the two beams induces an oscillating photocurrent on the nanoantennas at the difference frequency of the two beams, which is tunable by varying the wavelength of one of the CW seed lasers. The radiated power is measured using a superconducting bolometer (QMC Instruments Ltd. Model QNbB/PTC). At the same total optical power level, the optical beam size incident on the nanoantenna array is adjusted to vary the optical excitation intensity. Figure 3.12 shows the measured radiation power at different terahertz frequencies as a function of the $1/e^2$ optical beam diameter. An optimal optical beam size that maximizes the radiated power is clearly observed at each terahertz frequency. At very small beam sizes, the carrier screening becomes too strong, creating an opposing electric field that consequently reduces the acceleration of the carriers and the radiation power. On the other hand, at very large beam sizes, the destructive interference of the radiation from the nanoantennas decreases the total radiated power. This is clearly revealed by the fact that the optimal beam diameter decreases as the terahertz frequency increases, where the destructive interference gets stronger at shorter wavelengths. Finally, it should be noted that the optimal beam diameter values shown in Fig. 3.12 support the optimal value of ~ 100 μm under pulsed operation, which contains the contribution from all of the radiated frequency components.

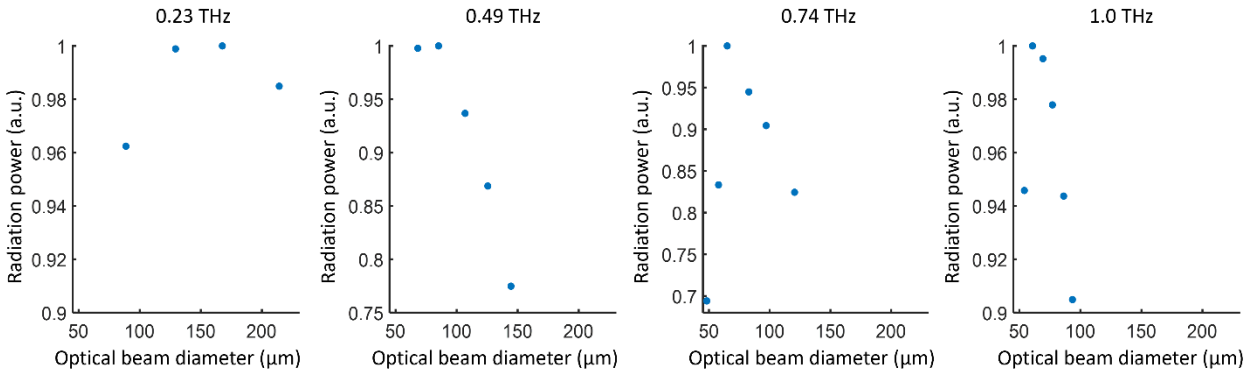

Fig. 3.12: Measured quasi-CW radiation power from the graded InGaAs emitter as a function of the $1/e^2$ incident optical beam diameter at various terahertz frequencies.

In summary, we demonstrate high-power terahertz pulse generation from bias-free nanoantennas on a graded composition InGaAs structure with a linearly graded Indium composition. Such a semiconductor heterostructure creates a deep built-in quasi-electric field that extends throughout the entire thickness of the InGaAs layer while maintaining a field strength that is high enough to drift the photo-generated electrons at high velocities. As a result, the number of the collected electrons by the nanoantennas that contribute to terahertz pulse generation is increased. Furthermore, by the excitation of surface plasmon waves along the nanoantennas at ~1550 nm wavelength range, the optical generation is significantly enhanced within a few hundred nanometers beneath each nanoantenna element, where the built-in electric field strength is maximized, greatly reducing the transit time of the photo-generated electrons to the radiating nanoantennas. Using a fabricated graded InGaAs emitter, we demonstrate the generation of terahertz pulses with a record-high 860 μW average power at an average optical pump power of 900 mW. It should be pointed out that further optimization of the layer thicknesses, composition gradient, and doping levels could provide even faster carrier dynamics to increase the radiation power and bandwidth of the bias-free photoconductive emitters beyond the prototypes explored in this work. In addition, a distributed Bragg reflector at the bottom of the photoconductive structure could form an optical cavity to further enhance the power efficiencies [111]. The high radiation power and high reliability of the presented terahertz emitter, without requiring any external bias voltage or special optical focus and alignment requirements, would be very attractive for real-world terahertz imaging and spectroscopy systems. As previously demonstrated [91], the emitter chip can be simply mounted at the tip of an optical fiber to provide a flexible platform for diverse application scenarios.

3.3.3. Supplementary Information for the Theoretical Modeling of Bilayer InAs Emitter and Graded InGaAs Emitter

Steady-state electron drift velocity in the graded InGaAs structure

The electron drift velocity is quantified by the following empirical formula [153],

$$v_e = \frac{\mu_e \mathcal{E}}{\sqrt{1 + \left(\frac{\mu_e \mathcal{E}}{v_{sat}}\right)^2}}, \tag{3.10}$$

where v_e is the electron drift velocity, μ_e is the low-field electron mobility, $\mathcal{E}$ is the electric field, and $v_{sat} = \sqrt{2E_{phonon}/m^*}$ is the approximated saturation velocity determined by the optical phonon energy E_{phonon} and effective mass m^*. The low-field mobility values, effective masses, and optical phonon energies for highly doped $In_{0.53}Ga_{0.47}As$ and InAs are found from the literature [154-159]. Using these parameters, for an electric field of 6 kV/cm in the graded InGaAs emitter, similar velocities of ~ 1.5×10^7 cm/s are obtained for both $In_{0.53}Ga_{0.47}As$ and InAs. This justifies that the approximation of a constant steady-state drift velocity of 1.5×10^7 cm/s throughout the entire graded InGaAs structure is valid.

Estimation of the diffusion term for impulse response calculation

To see why the diffusion current can be ignored in the closed form calculations, it should be noted that the initial carrier concentration is determined by the plasmonic-enhanced optical generation profile, which follows an exponential decay into the substrate due to the evanescent nature of the surface plasmon waves. In other words, the initial carrier concentration can be approximated as $n_0 e^{-y/L_0}$, where n_0 denotes the initial electron concentration at the surface and

$L_0 \sim 210\ nm$ characterizes the decay rate of the electron concentration into the substrate. Therefore, the diffusion current is approximately

$$J_{diff} = \frac{D_n}{L_0^2} n_0 e^{-y/L_0}, \tag{3.11}$$

while the drift term J_{drift} and recombination term R are

$$J_{drift} = \frac{v_e}{L_0} n_0 e^{-y/L_0}, \tag{3.12}$$

$$R = \frac{-1}{\tau_e} n_0 e^{-y/L_0}. \tag{3.13}$$

Comparing the constant factors of the three terms with $L_0 = 210\ nm$, $D_n = 1.3 \times 10^{-3}\ m^2/s$, $v_e = 1.5 \times 10^7\ cm/s$ and $\tau_e = 5\ ps$, we have

$$\frac{D_n}{L_0^2} \ll \frac{v_e}{L_0}, \frac{D_n}{L_0^2} \ll \frac{1}{\tau_e}. \tag{3.14}$$

This justifies the negligible impact of the diffusion current. Similar arguments apply to the bilayer InAs emitter due to its high quasi-ballistic velocity in the undoped region and 5 ps carrier lifetime in the p+ doped region. To further support this claim, the electron drift-diffusion equation is numerically solved for the graded InGaAs emitter with and without the diffusion term, showing a negligible difference between the two results that are shown in Fig. 3.13.

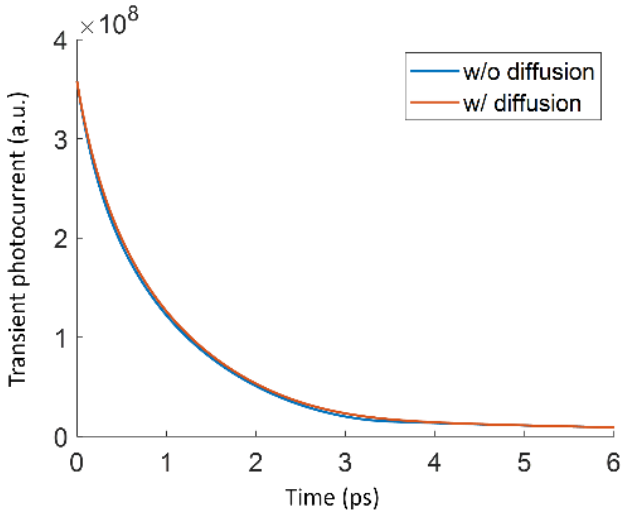

Fig. 3.13: Photocurrent impulse response obtained by numerically solving the electron drift-diffusion equation with and without the diffusion term.

Estimation of the radiated terahertz power spectrum

Due to the high conductivity of the substrates, a fraction of the injected currents (Fig. 3.10d) is directed to flow on the nanoantennas. The induced current on the nanoantennas is calculated by considering the antenna and substrate impedance levels. Next, the transient current induced on the nanoantennas is converted to the frequency domain, $I_{induced}(f)$, to obtain the radiated electric field $E_i(r,\theta,\phi,f)$ from a single nanoantenna element

$$E_i(r,\theta,\phi,f) \sim jksin\theta \frac{e^{-jkr}}{r} I_{induced}(f), \tag{3.15}$$

where $k = 2\pi fn/c$ is the wavevector, with n = 3.6 as the refractive index of GaAs. (r,θ,ϕ) are the spherical coordinates with their orientations relative to the nanoantenna array illustrated in Fig. 3.14.

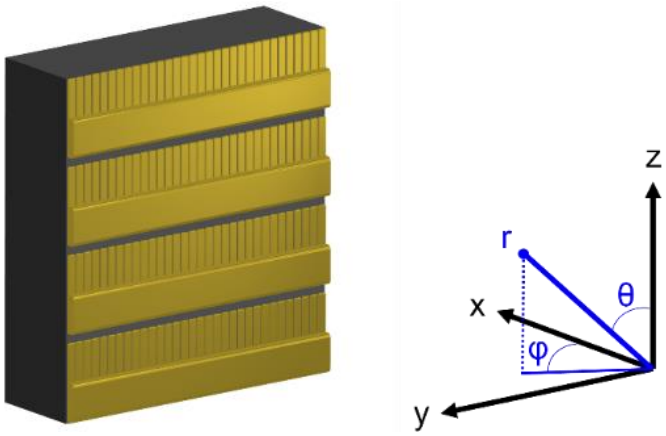

Fig. 3.14: Nanoantenna array orientation and the definition of the spherical coordinates.

Then, the far-field radiated power spectrum from the two-dimensional nanoantenna array excited by the incident optical beam is calculated using the nanoantenna array factors.

$$E_{array}(r,\theta,\phi,f) = E_i(r,\theta,\phi,f)AF_y(\theta,\phi,f)AF_z(\theta,f), \tag{3.16}$$

where AF_y and AF_z are the array factors of the nanoantenna array in the y and z directions:

$$AF_y(\theta,\phi,f) = \frac{sin\left(\frac{N_y\psi_y}{2}\right)}{sin\left(\frac{\psi_y}{2}\right)}, \psi_y = p_y k sin\phi sin\theta, \tag{3.17}$$

$$AF_z(\theta,f) = \frac{sin\left(\frac{N_z\psi_z}{2}\right)}{sin\left(\frac{\psi_z}{2}\right)}, \psi_z = p_z k cos\theta, \tag{3.18}$$

where p_y = 440 nm and p_z = 4.5 μm are the periodicity of the nanoantennas in the y and z directions, respectively, and N_y and N_z are the number of nanoantennas in the y and z directions, respectively, determined by the incident optical beam size. Then, the total radiated power is obtained from the integral below, with η_0 being the vacuum wave impedance.

$$P_{rad}(f) = \frac{1}{2\eta_0}\int_{-\pi/2}^{\pi/2}\int_{0}^{\pi}\left|E_{array}(\theta,\phi,f)\right|^2 r^2 sin\theta d\theta d\phi, \tag{3.19}$$

3.4. Tunable Continuous-Wave Terahertz Generation through Optical Parametric Oscillation in On-Chip Microresonators

In Section 3.3.2, it is shown that, although the bias-free nanoantenna arrays are specifically optimized for broadband pulsed radiation, the achieved ultrafast carrier dynamics actually enable CW generation under bias-free operation as well. Therefore, we use the bias-free emitters to realize a CW terahertz synthesizer pumped by optical frequencies generated from a nonlinear microresonator, leading to a broad terahertz frequency tuning range with sub-Hz linewidths after frequency stabilization. All experimental results presented in this section are done with a bilayer InAs emitter on an SI-GaAs substrate.

3.4.1. Free-Running Continuous-Wave Generation

As shown in Fig. 3.15, to characterize the power spectrum of the bilayer InAs emitter, a pair of free-running CW lasers with equal power are combined and amplified to pump the emitter. The radiated terahertz power is measured using a pyroelectric detector (QMC Instruments Ltd.) with lock-in detection.

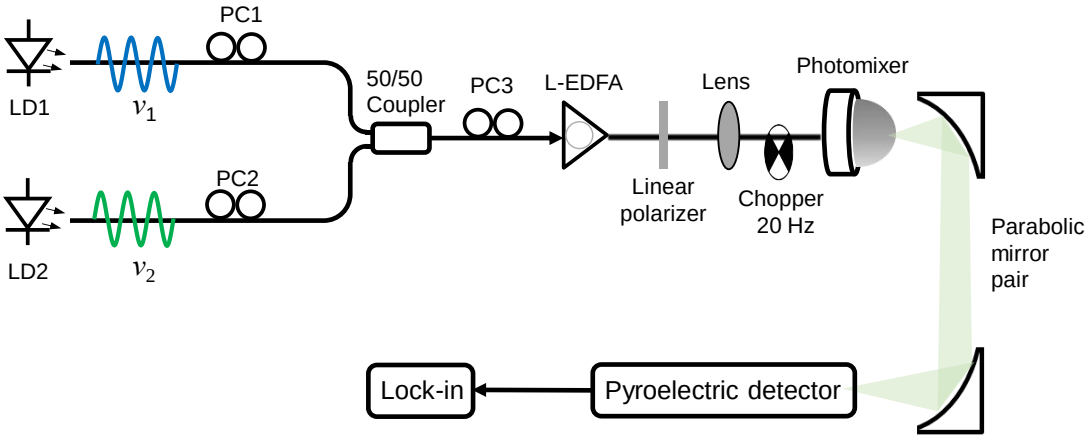

Fig. 3.15: Experimental setup for characterizing the power spectrum of the bilayer InAs emitter. LD: laser diode, PC: polarization controller, L-EDFA: L-band erbium doped fiber amplifier.

The measured power spectrum from the bilayer InAs emitter in the frequency range of 0.1-2.3 THz is shown in Fig. 3.16, where multiple water absorption lines are clearly observed in agreement with the HITRAN database (plotted in red).

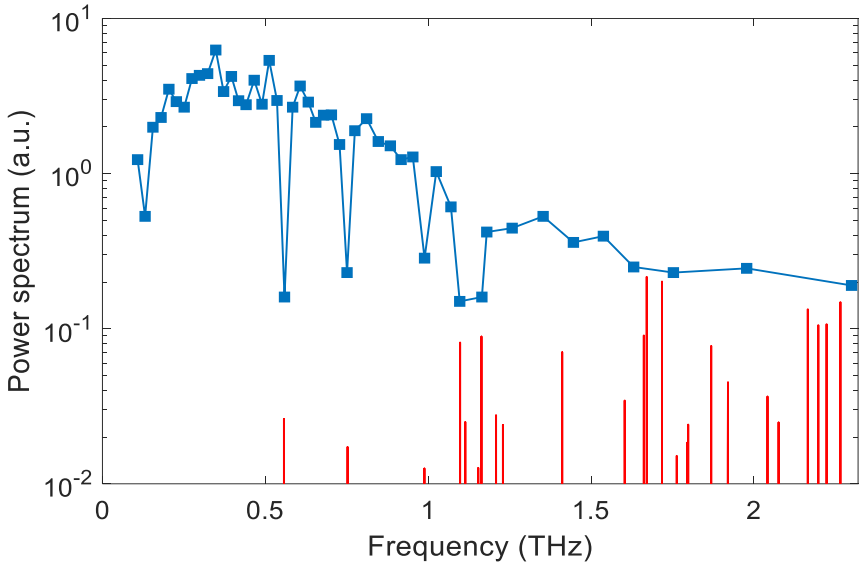

Fig. 3.16: Measured terahertz power spectrum spanning from 100 GHz to 2.3 THz by a pyroelectric detector.

After verifying broadband CW generation from the bias-free emitter, the CW laser pair is replaced by an optically excited microresonator for generating tunable optical frequency pairs that will be used for photomixing. The microresonator is a Si_3N_4-based waveguide cavity with a high quality factor, which is designed to enhance optical parametric oscillation. As a result, when the microresonator is pumped with an optical wavelength close to one of its resonance frequencies, under phase matching conditions, it can transfer part of its energy to another resonance frequency, generating a parametric sideband that is tunable by detuning the pump optical frequency. With a free spectral range of ~ 20 GHz, the generated parametric sidebands will be an integer multiple of 20 GHz away from the pump frequency. Therefore, a step-tunable terahertz frequency is generated by photomixing the pump and the parametric sidebands. The output terahertz radiation is routed to a harmonic mixer (VDI MixAMC with WR 1.5 and WR 2.2 horn antennas) with the

downconverted IF signal (~ 1 GHz) observed on an electrical spectrum analyzer (ESA). Figure 3.17 shows many IF spectra compiled together to demonstrate the step-tunable input terahertz frequency from 330 GHz to 750 GHz. Note that this range is only limited by the harmonic mixer bandwidth. Clearly, the lower intensities at 550 GHz and 750 GHz are due to the presence of water vapor absorption lines. For all other frequencies, the observed SNR is about 50 dB under a 10 kHz resolution bandwidth.

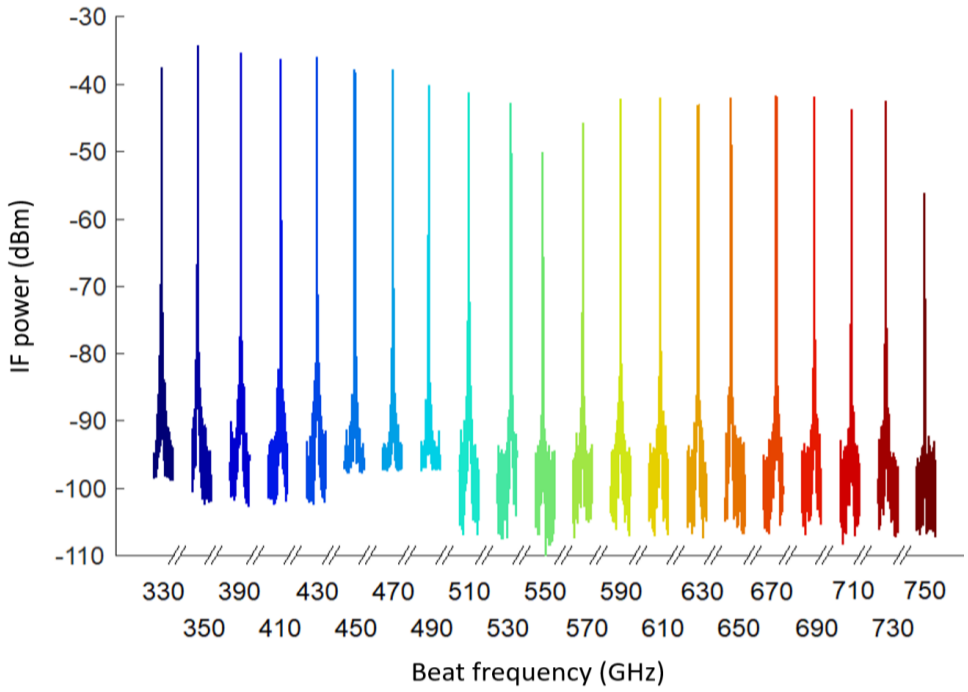

Fig. 3.17: Measured intermediate frequency spectra of the downconverted terahertz wave, which is step-tunable with a step size ~ 20 GHz equal to the free spectral range of the microresonator. The frequency range of 330 ~ 750 GHz is only limited by the bandwidth of the harmonic mixer.

Moreover, since both the pump and parametric sideband emit from a single microresonator, the common mode phase noise is strongly suppressed. Therefore, the terahertz beat frequency generated from the microresonator under free-running condition is much more stable as compared to a pair of independent CW lasers. To experimentally characterize the beat frequency variation, the downconverted IF spectrum is repetitively captured using an ESA 100 times, as shown in Fig.

3.18. Clearly, the microresonator shows ~ 4 times lower frequency variation compared to the CW laser pair. The residual frequency variation comes from the power and wavelength fluctuations of the pump beam, which slightly changes the phase matching condition and, hence, the frequency of the parametric sideband. In the next section, we show that the use of a feedback loop allows stabilizing the pump beam, reaching sub-Hz stability for the generated terahertz radiation.

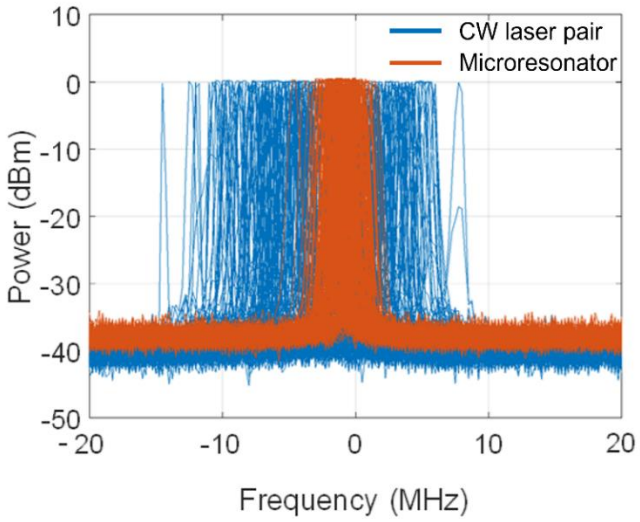

Fig. 3.18: Measured intermediate frequency spectra of the downconverted terahertz wave generated from a pair of free-running CW lasers (blue) and the microresonator (orange), showing a ~ 4 times frequency stability improvement for the latter case.

3.4.2. Frequency-Stabilized Continuous-Wave Generation

Tunability of the generated terahertz wave highly depends on effective microresonator temperature which, in turn, introduces thermal stochastic frequency fluctuations of the generated terahertz signal induced by thermodynamical fluctuations of the microresonator mode. The small mode volume of the microresonator physically leads to high thermal sensitivity to ambient temperature fluctuations. The thermal instability originates from thermal energy exchange between the microresonator and ambient background or laser heating from the intracavity optical power

absorption. The thermal fluctuations, fundamentally mediated by thermal expansion and thermo-refractive index effects, impose phase decoherence of the generated terahertz signal.

To improve the instantaneous linewidth and frequency stability of the generated terahertz signal and further increase its frequency tuning resolution, microresonator intracavity power stabilization (main stabilization loop) and pump-resonance detuning stabilization (auxiliary stabilization loop) are engaged, as illustrated in Fig. 3.19. A terahertz wave at 650 GHz is downconverted to an IF of ~ 1 GHz using the harmonic mixer. An ESA and a signal source analyzer (SSA) are used to characterize instantaneous linewidth and frequency noise of the downconverted signal at IF, respectively. To facilitate feedback locking, the IF passes through a 260× frequency divider and mixes with a local oscillator (LO2) to generate the error signal, which is fed to a proportional-integral-derivative (PID) controller to control the pump laser polarization to stabilize the microresonator intracavity power after polarization demodulation with a linear polarizer. Meanwhile, the integral error signal auxiliary controls the pump laser frequency to facilitate the stabilization of the pump-resonance detuning.

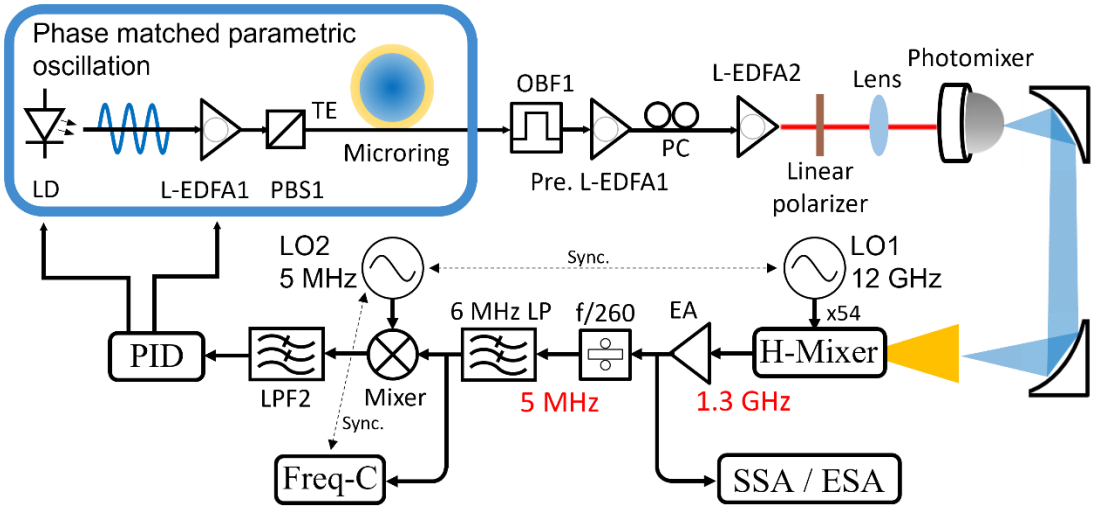

Fig. 3.19: Experimental setup for terahertz frequency stabilization. PBS: polarizing beamsplitter, OBF: optical bandpass filter, LO: local oscillator, Freq-C: frequency counter.

Figure 3.20 shows the stabilized instantaneous linewidth of the generated terahertz signal over a 50 Hz frequency span and a resolution bandwidth and video bandwidth of 1 Hz. After pump laser power and frequency stabilization, the signal shows more than a 40 dB SNR and 0.98 Hz linewidth for a 1.83-second sweep time.

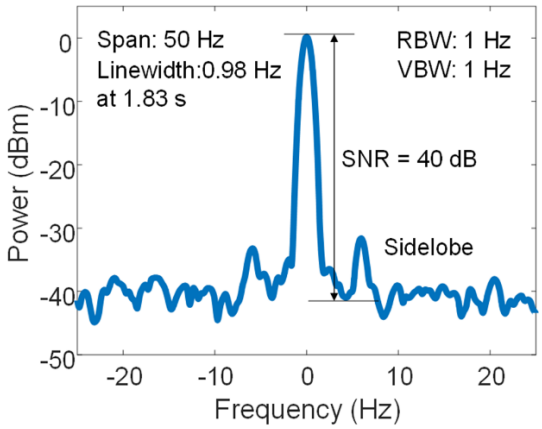

Fig. 3.20: Measured instantaneous linewidth of the generated terahertz signal at 650 GHz under frequency stabilization, showing more than a 40 dB SNR and 0.98 Hz linewidth for a 1.83-second sweep time.

Finally, the long-term frequency stability of the terahertz signal is examined with a referenced frequency counter for a 300-ms gate time. Figure 3.21 shows the Allan deviation of the free-running and residual signals at 650 GHz. The residual frequency stability is improved by 400,000 times for a 1-second averaging time and reaches the instrumental limit of the frequency counter. The stabilized Allan deviation curve follows the ideal $1/\tau$ slope for the entire measurement time of 1000 s.

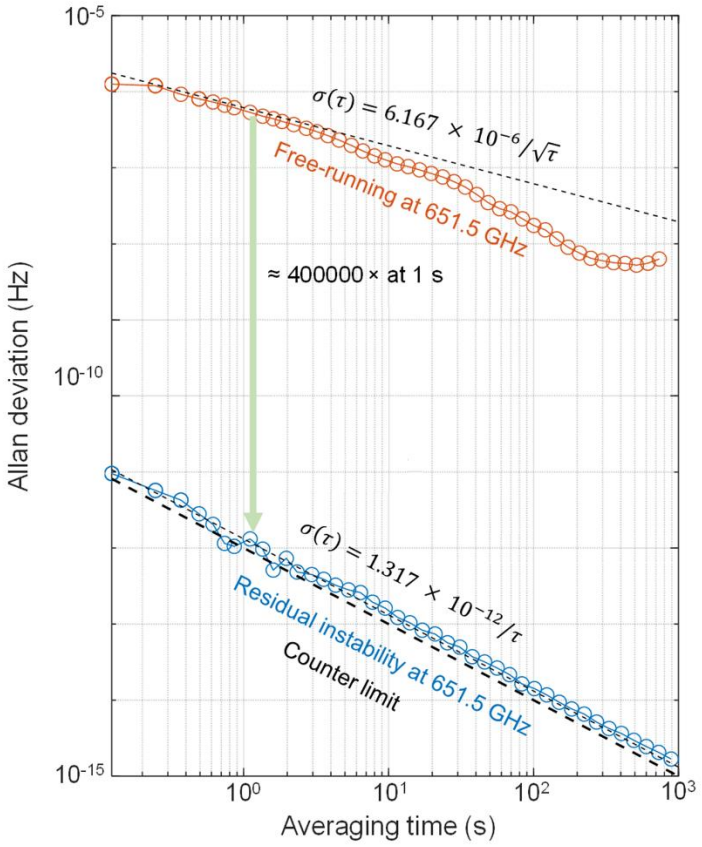

Fig. 3.21: Allan deviation of the free-running and stabilized terahertz signals.

Chapter 4: Conclusion

This dissertation explores two major approaches to develop high-performance telecommunication-compatible photoconductive terahertz sources and detectors without using conventional defect-introduced short-carrier-lifetime photoconductors: plasmonics-enabled ultrafast carrier dynamics based on carrier transit time reduction and photoconductor band engineering. Both of these approaches take advantage of the plasmonic enhancement of near field optical generation close to the plasmonic electrodes at the surface, leading to significantly reduced transport distance for the photocarriers, which facilitate the ultrafast photoconductive response required for terahertz operation.

Plasmonics-enabled carrier transit time reduction has demonstrated diverse functionalities including the realization of terahertz sources and detectors under both pulsed and CW operation, making it highly accessible and applicable when utilizing various semiconductors and optical wavelengths for designing photoconductive terahertz devices. Moreover, further improvement in the device efficiency is expected by incorporating distributed Bragg reflectors beneath the active photo-absorbing layer, which leads to additional cavity enhancement of the optical generation. Also, further reduction of the InGaAs thickness below 200 nm used in the prototype devices would suppress the dark/noise current, leading to broader bandwidth operation, while having a negligible impact on the SNR since the optical absorption is tightly confined near the plasmonic contact electrodes.

Aiming to solve the thermal reliability issue for telecommunication compatible terahertz emitters, the combination of plasmonic enhancement and photoconductor band engineering has led to the realization of several bias-free photoconductive emitters, which offer multiple orders of

magnitude improvement in optical-to-terahertz conversion efficiency compared to other passive terahertz generation techniques. Different multilayered photoconductive structures are investigated to introduce the strong band-bending required for high-efficiency, passive optical-to-terahertz conversion. The impacts of the substrate loss and lattice mismatch on the terahertz radiation power and bandwidth are analyzed in detail. In particular, bilayer InAs grown on a high resistivity silicon substrate offers improved terahertz radiation bandwidth in addition to its integrability with other silicon photonic platforms, offering a very promising solution for real-world terahertz applications. Aside from the substrate properties, the impact of the built-in electric field profile on the carrier dynamics is also extensively analyzed. Using graded-composition InGaAs structures, a deep built-in electric field is induced throughout the entire photoconductive layer, allowing all of the photo-generated electrons to be accelerated to contribute to terahertz generation. Consequently, a record-high pulsed terahertz power level of 860 μW is demonstrated compared to other telecommunication-compatible photoconductive emitters.

One of the most important directions to further improve the performance of bias-free emitters is to reduce the photocurrent leakage from the antenna to the highly conducting InAs substrate. Optimized choices of the nanoantenna geometry and selective InAs etching are some promising directions that need to be further investigated and developed. It is expected that further optimization of the photoconductor structure, composition, doping profile, and MBE growth on silicon substrate will lead to even faster carrier dynamics, making bias-free emitters an attractive solution for future terahertz systems.

Finally, the use of bias-free emitters together with on-chip nonlinear microresonators for implementing a tunable CW terahertz synthesizer is introduced. With active frequency

stabilization through a feedback loop, broadly tunable terahertz radiation with a sub-Hz linewidth is achieved.

Bibliography

[1] M. Van Exter, C. Fattinger, and D. Grischkowsky, "Terahertz time-domain spectroscopy of water vapor," *Opt. Lett.* **14**(20), 1128-1130 (1989).

[2] A. Markelz, S. Whitmire, J. Hillebrecht, and R. Birge, "THz time domain spectroscopy of biomolecular conformational modes," *Phys. Med. Biol.* **47**(21), 3797 (2002).

[3] Y. C. Shen, T. Lo, P. F. Taday, B. E. Cole, W. R. Tribe, and M. C. Kemp, "Detection and identification of explosives using terahertz pulsed spectroscopic imaging," *Appl. Phys. Lett.* **86**(24), 241116 (2005).

[4] D. M. Mittleman, R. H. Jacobsen, R. Neelamani, R. G. Baraniuk, and M. C. Nuss, "Gas sensing using terahertz time-domain spectroscopy," *Appl. Phys. B* **67**(3), 379-390 (1998).

[5] M. Kato, S. R. Tripathi, K. Murate, K. Imayama, and K. Kawase, "Non-destructive drug inspection in covering materials using a terahertz spectral imaging system with injection-seeded terahertz parametric generation and detection," *Opt. Express* **24**(6), 6425-6432 (2016).

[6] A. Redo-Sanchez, B. Heshmat, A. Aghasi, et al., "Terahertz time-gated spectral imaging for content extraction through layered structures," *Nat. Commun.* **7**(1), 1-7 (2016).

[7] M. C. Kemp, P. F. Taday, B. E. Cole, J. A. Cluff, A. J. Fitzgerald, and W. R. Tribe, "Security applications of terahertz technology," In *Terahertz for Military and Security Applications*, vol. 5070, pp. 44-52. International Society for Optics and Photonics, 2003.

[8] R. Ulbricht, E. Hendry, J. Shan, T. F. Heinz, and M. Bonn, "Carrier dynamics in semiconductors studied with time-resolved terahertz spectroscopy," *Rev. Mod. Phys.* **83**(2), 543 (2011).

[9] S. E. Ralph, S. Perkowitz, N. Katzenellenbogen, and D. Grischkowsky, "Terahertz spectroscopy of optically thick multilayered semiconductor structures," *JOSA B* **11**(12), 2528-2532 (1994).

[10] B. B. Hu, and M. C. Nuss, "Imaging with terahertz waves," *Opt. Lett.* **20**(16), 1716-1718 (1995).

[11] M. Tonouchi, "Cutting-edge terahertz technology," *Nat. Photonics* **1**(2), 97-105 (2007).

[12] B. Ferguson, and X.-C. Zhang, "Materials for terahertz science and technology," *Nat. Mater.* **1**(1), 26-33 (2002).

[13] P. U. Jepsen, D. G. Cooke, and M. Koch, "Terahertz spectroscopy and imaging–Modern techniques and applications," *Laser Photonics Rev.* **5**(1), 124-166 (2011).

[14] E. Pickwell, and V. P. Wallace, "Biomedical applications of terahertz technology," *J. Phys. D: Appl. Phys.* **39**(17), R301 (2006).

[15] S. Fan, Y. He, B. S. Ung, and E. Pickwell-MacPherson, "The growth of biomedical terahertz research," *J. Phys. D: Appl. Phys.* **47**(37), 374009 (2014).

[16] R. M. Woodward, B. E. Cole, V. P. Wallace, et al., "Terahertz pulse imaging in reflection geometry of human skin cancer and skin tissue," *Phys. Med. Biol.* **47**(21), 3853 (2002).

[17] V. P. Wallace, P. F. Taday, A. J. Fitzgerald, et al., "Terahertz pulsed imaging and spectroscopy for biomedical and pharmaceutical applications," *Faraday Discuss.* **126**, 255-263 (2004).

[18] E. Castro-Camus, M. Palomar, and A. A. Covarrubias, "Leaf water dynamics of Arabidopsis thaliana monitored in-vivo using terahertz time-domain spectroscopy," *Sci. Rep.* **3**(1), 1-5 (2013).

[19] F. Rutz, M. Koch, S. Khare, M. Moneke, H. Richter, and U. Ewert, "Terahertz quality control of polymeric products," *Int. J. Infrared Millimeter Waves* **27**(4), 547-556 (2006).

[20] M. Scheller, C. Jansen, and M. Koch, "Analyzing sub-100-μm samples with transmission terahertz time domain spectroscopy," *Opt. Commun.* **282**(7), 1304-1306 (2009).

[21] S. Krimi, J. Klier, J. Jonuscheit, G. Von Freymann, R. Urbansky, and R. Beigang, "Highly accurate thickness measurement of multi-layered automotive paints using terahertz technology," *Appl. Phys. Lett.* **109**(2), 021105 (2016).

[22] P. C. Ashworth, E. Pickwell-MacPherson, E. Provenzano, et al., "Terahertz pulsed spectroscopy of freshly excised human breast cancer," *Opt. Express* **17**(15), 12444-12454 (2009).

[23] Smith, Peter R., David H. Auston, and Martin C. Nuss, "Subpicosecond photoconducting dipole antennas," *IEEE J. Quantum Electron.* **24**(2), 255-260 (1988).

[24] Auston, D. H., K. P. Cheung, and P. R. Smith, "Picosecond photoconducting Hertzian dipoles," *Appl. Phys. Lett.* **45**(3), 284-286 (1984).

[25] Verghese, S., et al., "Generation and detection of coherent terahertz waves using two photomixers," *Appl. Phys. Lett.* **73**(26), 3824-3826 (1998).

[26] Jepsen, P. Uhd, Rune Hylsberg Jacobsen, and S. R. Keiding, "Generation and detection of terahertz pulses from biased semiconductor antennas," *JOSA B* **13**(11), 2424-2436 (1996).

[27] Zhao, G., et al., "Design and performance of a THz emission and detection setup based on a semi-insulating GaAs emitter," *Rev. Sci. Instrum.* **73**(4), 1715-1719 (2002).

[28] Matsuura, Shuji, Masahiko Tani, and Kiyomi Sakai, "Generation of coherent terahertz radiation by photomixing in dipole photoconductive antennas," *Appl. Phys. Lett.* **70**(5), 559-561 (1997).

[29] Jarrahi, Mona, and Thomas H. Lee, "High-power tunable terahertz generation based on photoconductive antenna arrays," *2008 IEEE MTT-S International Microwave Symposium Digest*. IEEE, 2008.

[30] Peytavit, E., et al., "Milliwatt-level output power in the sub-terahertz range generated by photomixing in a GaAs photoconductor," *Appl. Phys. Lett.* **99**(22), 223508 (2011).

[31] Roehle, H., et al., "Next generation 1.5 μm terahertz antennas: mesa-structuring of InGaAs/InAlAs photoconductive layers," *Opt. Express* **18**(3), 2296-2301 (2010).

[32] Taylor, Z. D., et al., "Resonant-optical-cavity photoconductive switch with 0.5% conversion efficiency and 1.0 W peak power," *Opt. Lett.* **31**(11), 1729-1731 (2006).

[33] Jarrahi, Mona, "Terahertz radiation-band engineering through spatial beam-shaping," *IEEE Photonics Technol. Lett.* **21**(13), 830-832 (2009).

[34] Preu, Sascha, et al., "1550 nm ErAs: In (Al) GaAs large area photoconductive emitters," *Appl. Phys. Lett.* **101**(10), 101105 (2012).

[35] Cai, Y., et al., "Coherent terahertz radiation detection: Direct comparison between free-space electro-optic sampling and antenna detection," *Appl. Phys. Lett.* **73**(4), 444-446 (1998).

[36] Sun, F. G., G. A. Wagoner, and X-C. Zhang, "Measurement of free-space terahertz pulses via long-lifetime photoconductors," *Appl. Phys. Lett.* **67**(12), 1656-1658 (1995).

[37] O'Hara, John F., et al., "Enhanced terahertz detection via ErAs: GaAs nanoisland superlattices," *Appl. Phys. Lett.* **88**(25), 251119 (2006).

[38] Liu, Tze-An, et al., "Ultrabroadband terahertz field detection by photoconductive antennas based on multi-energy arsenic-ion-implanted GaAs and semi-insulating GaAs," *Appl. Phys. Lett.* **83**(7), 1322-1324 (2003).

[39] Suzuki, Masato, and Masayoshi Tonouchi, "Fe-implanted InGaAs photoconductive terahertz detectors triggered by 1.56 μm femtosecond optical pulses," *Appl. Phys. Lett.* **86**(16), 163504 (2005).

[40] Liu, Tze-An, et al., "Ultrabroadband terahertz field detection by proton-bombarded InP photoconductive antennas," *Opt. Express* **12**(13), 2954-2959 (2004).

[41] Castro-Camus, E., et al., "Polarization-sensitive terahertz detection by multicontact photoconductive receivers," *Appl. Phys. Lett.* **86**(25), 254102 (2005).

[42] Peter, F., et al., "Coherent terahertz detection with a large-area photoconductive antenna," *Appl. Phys. Lett.* **91**(8), 081109 (2007).

[43] Liu, Shuchang, Xiang Shou, and Ajay Nahata, "Coherent detection of multiband terahertz radiation using a surface plasmon-polariton based photoconductive antenna," *IEEE Trans. Terahertz Sci. Technol.* **1**(2), 412-415 (2011).

[44] Preu, Sascha, et al., "Tunable, continuous-wave terahertz photomixer sources and applications," *J. Appl. Phys.* **109**(6), 4 (2011).

[45] Takayanagi, Jun, Hiroki Jinno, Shingo Ichino, Koji Suizu, Masatsugu Yamashita, Toshihiko Ouchi, Shintaro Kasai et al., "High-resolution time-of-flight terahertz tomography using a femtosecond fiber laser," *Opt. Express* **17**(9), 7533-7539 (2009).

[46] Bessou, Maryelle, Bruno Chassagne, Jean-Pascal Caumes, Christophe Pradère, Philippe Maire, Marc Tondusson, and Emmanuel Abraham, "Three-dimensional terahertz computed tomography of human bones," *Appl. Opt.* **51**(28), 6738-6744 (2012).

[47] Lopato, Przemyslaw, "Pulsed excitation terahertz tomography–multiparametric approach," *Open Phys.* **16**(1), 111-116 (2018).

[48] Hindle, Francis, Arnaud Cuisset, Robin Bocquet, and Gaël Mouret, "Continuous-wave terahertz by photomixing: applications to gas phase pollutant detection and quantification," *C. R. Phys.* **9**(2), 262-275 (2008).

[49] Bigourd, Damien, Arnaud Cuisset, Francis Hindle, Sophie Matton, Eric Fertein, Robin Bocquet, and Gaël Mouret, "Detection and quantification of multiple molecular species in mainstream cigarette smoke by continuous-wave terahertz spectroscopy," *Opt. Lett.* **31**(15), 2356-2358 (2006).

[50] Eliet, Sophie, Marie-Aline Martin-Drumel, Mickaël Guinet, Francis Hindle, Gaël Mouret, Robin Bocquet, and Arnaud Cuisset, "Doppler limited rotational transitions of OH and SH radicals measured by continuous-wave terahertz photomixing," *J. Mol. Struct.* **1006**(1-3), 13-19 (2011).

[51] F. W. Smith, A. R. Calawa, C-L. Chen, M. J. Manfra, and L. J. Mahoney, "New MBE buffer used to eliminate backgating in GaAs MESFETs," *IEEE Electron Device Lett.* **9**(2), 77-80 (1988).

[52] A. C. Warren, N. Katzenellenbogen, D. Grischkowsky, J. M. Woodall, M. R. Melloch, and N. Otsuka, "Subpicosecond, freely propagating electromagnetic pulse generation and detection using GaAs:As epilayers," *Appl. Phys. Lett.* **58**(14), 1512-1514 (1991).

[53] E. R. Brown, F. W. Smith, and K. A. McIntosh, "Coherent millimeter-wave generation by heterodyne conversion in low-temperature-grown GaAs photoconductors," *J. Appl. Phys.* **73**(3), 1480-1484 (1993).

[54] S. Gupta, M. Y. Frankel, J. A. Valdmanis, et al., "Subpicosecond carrier lifetime in GaAs grown by molecular beam epitaxy at low temperatures," *Appl. Phys. Lett.* **59**(25), 3276-3278 (1991).

[55] F. Ganikhanov, G-R. Lin, W-C. Chen, C-S. Chang, and C-L. Pan, "Subpicosecond carrier lifetimes in arsenic-ion-implanted GaAs," *Appl. Phys. Lett.* **67**(23), 3465-3467 (1995).

[56] J. Lloyd-Hughes, E. Castro-Camus, M. D. Fraser, C. Jagadish, and M. B. Johnston, "Carrier dynamics in ion-implanted GaAs studied by simulation and observation of terahertz emission," *Phys. Rev. B* **70**(23), 235330 (2004).

[57] M. Griebel, J. H. Smet, J. Kuhl, et al., “Picosecond carrier dynamics in ErAs:GaAs superlattices,” In *Ultrafast Electronics and Optoelectronics*, p. UWC5. Optical Society of America, 2001.

[58] V. Pačebutas, A. Bičiūnas, S. Balakauskas, et al., “Terahertz time-domain-spectroscopy system based on femtosecond Yb:fiber laser and GaBiAs photoconducting components,” *Appl. Phys. Lett.* **97**(3), 031111 (2010).

[59] V. Pačebutas, A. Bičiūnas, K. Bertulis, and A. Krotkus, "Optoelectronic terahertz radiation system based on femtosecond 1 μm laser pulses and GaBiAs detector," *Electron. Lett.* **44**(19), 1154-1155 (2008).

[60] M. S. Kong, J. S. Kim, S. P. Han, et al., “Terahertz radiation using log-spiral-based low-temperature-grown InGaAs photoconductive antenna pumped by mode-locked Yb-doped fiber laser,” *Opt. Express* **24**(7), 7037-7045 (2016).

[61] G. Matthäus, B. Ortaç, J. Limpert, et al., “Intracavity terahertz generation inside a high-energy ultrafast soliton fiber laser,” *Appl. Phys. Lett.* **93**(26), 261105 (2008).

[62] Mangeney, J., N. Chimot, L. Meignien, N. Zerounian, P. Crozat, K. Blary, J. F. Lampin, and P. Mounaix, "Emission characteristics of ion-irradiated $In_{0.53}Ga_{0.47}As$ based photoconductive antennas excited at 1.55 μm," *Opt. Express* **15**(14), 8943-8950 (2007).

[63] Joulaud, L., Mangeney, J., Lourtioz, J. M., Crozat, P., & Patriarche, G., “Thermal stability of ion-irradiated InGaAs with (sub-) picosecond carrier lifetime,” *Appl. Phys. Lett.* **82**(6), 856-858 (2003).

[64] Chimot, N., Mangeney, J., Joulaud, L., Crozat, P., Bernas, H., Blary, K., & Lampin, J. F., "Terahertz radiation from heavy-ion-irradiated $In_{0.53}Ga_{0.47}As$ photoconductive antenna excited at 1.55 μm," *Appl. Phys. Lett.* **87**(19), 193510 (2005).

[65] Mangeney, J., & Crozat, P., "Ion-irradiated $In_{0.53}Ga_{0.47}As$ photoconductive antennas for THz generation and detection at 1.55 μm wavelength," *C. R. Phys.* **9**(2), 142-152 (2008).

[66] M. Sukhotin, E. R. Brown, D. Driscoll, M. Hanson, and A. C. Gossard, "Picosecond photocarrier-lifetime in ErAs:InGaAs at 1.55 μm," *Appl. Phys. Lett.* **83**(19), 3921-3923 (2003).

[67] U. Nandi, J. C. Norman, A. C. Gossard, H. Lu, and S. Preu, "1550-nm driven ErAs: In (Al) GaAs photoconductor-based terahertz time domain system with 6.5 THz bandwidth," *J. Infrared, Millimeter, Terahertz Waves* **39**(4), 340-348 (2018).

[68] A.D.J. Fernandez Olvera, H. Lu, A. C. Gossard, and S. Preu, "Continuous-wave 1550 nm operated terahertz system using ErAs: In (Al) GaAs photo-conductors with 52 dB dynamic range at 1 THz," *Opt. Express* **25**(23), 29492-29500 (2017).

[69] B. Globisch, R. J. B. Dietz, R. B. Kohlhaas, et al., "Iron doped InGaAs: Competitive THz emitters and detectors fabricated from the same photoconductor," *J. Appl. Phys.* **121**(5), 053102 (2017).

[70] R. B. Kohlhaas, B. Globisch, S. Nellen, et al., "Rhodium doped InGaAs: A superior ultrafast photoconductor," *Appl. Phys. Lett.* **112**(10), 102101 (2018).

[71] R. B. Kohlhaas, S. Breuer, L. Liebermeister, et al., “637 μW emitted terahertz power from photoconductive antennas based on rhodium doped InGaAs,” *Appl. Phys. Lett.* **117**(13), 131105 (2020).

[72] B. Sartorius, H. Roehle, H. Künzel, et al., “All-fiber terahertz time-domain spectrometer operating at 1.5 μm telecom wavelengths,” *Opt. Express* **16**(13), 9565-9570 (2008).

[73] R. J. B. Dietz, B. Globisch, M. Gerhard, et al., “64 μW pulsed terahertz emission from growth optimized InGaAs/InAlAs heterostructures with separated photoconductive and trapping regions,” *Appl. Phys. Lett.* **103**(6), 061103 (2013).

[74] R. J. B. Dietz, B. Globisch, H. Roehle, D. Stanze, T. Göbel, and M. Schell, "Influence and adjustment of carrier lifetimes in InGaAs/InAlAs photoconductive pulsed terahertz detectors: 6 THz bandwidth and 90dB dynamic range," *Opt. Express* **22**(16), 19411-19422 (2014).

[75] Dionne, J. A., et al., "Planar metal plasmon waveguides: frequency-dependent dispersion, propagation, localization, and loss beyond the free electron model," *Phys. Rev. B* **72**(7), 075405 (2005).

[76] Pendry, J. B., L. Martin-Moreno, and F. J. Garcia-Vidal, "Mimicking surface plasmons with structured surfaces," *Science* **305**(5685), 847-848 (2004).

[77] E. Ozbay, "Plasmonics: merging photonics and electronics at nanoscale dimensions," *Science* **311**(5758), 189-193 (2006).

[78] Ebbesen, Thomas W., et al., "Extraordinary optical transmission through sub-wavelength hole arrays," *Nature* **391**(6668), 667 (1998).

[79] Schuller, Jon A., et al., "Plasmonics for extreme light concentration and manipulation," *Nat. Mater.* **9**(3), 193 (2010).

[80] Genet, C., and T. W. Ebbesen, "Light in tiny holes," *Nanoscience And Technology: A Collection of Reviews from Nature Journals*. 205-212, (2010).

[81] A. Hartschuh, E. J. Sánchez, X. S. Xie, and L. Novotny, "High-resolution near-field Raman microscopy of single-walled carbon nanotubes," *Phys. Rev. Lett.* **90**(9), 095503 (2003).

[82] H. G. Frey, S. Witt, K. Felderer, and R. Guckenberger, "High-resolution imaging of single fluorescent molecules with the optical near-field of a metal tip," *Phys. Rev. Lett.* **93**(20), 200801 (2004).

[83] T. Ishi, J. Fujikata, K. Makita, T. Baba, and K. Ohashi, "Si nano-photodiode with a surface plasmon antenna," *Jpn. J. Appl. Phys.* **44**(3L), L364 (2005).

[84] L. Tang, S. E. Kocabas, S. Latif, et al., "Nanometre-scale germanium photodetector enhanced by a near-infrared dipole antenna," *Nat. Photonics* **2**(4), 226-229 (2008).

[85] M. R. Hashemi, S. H. Yang, T. Wang, N. Sepúlveda, and M. Jarrahi, "Electronically-controlled beam-steering through vanadium dioxide metasurfaces," *Sci. Rep.* **6**(1), 1-8 (2016).

[86] A. Abbes, P-K. Lu, P. Nouvel, et al., "280 GHz Radiation Source Driven by a 1064nm Continuous-Wave Dual-Frequency Vertical External Cavity Semiconductor Laser," In *2021 46th International Conference on Infrared, Millimeter and Terahertz Waves (IRMMW-THz)*, pp. 1-2. IEEE, 2021.

[87] P-K. Lu, and Mona Jarrahi, "A Continuous-wave Terahertz Self-heterodyne Spectroscopy System without Using Short-carrier-lifetime Photoconductors," In *2021 46th International Conference on Infrared, Millimeter and Terahertz Waves (IRMMW-THz)*, pp. 1-2. IEEE, 2021.

[88] W. Wang, P-K. Lu, A. K. Vinod, et al., "High spectral purity chip-scale tunable THz radiation source," In *CLEO: Applications and Technology*, pp. ATu2T-3. Optical Society of America, 2021.

[89] D. Turan, N. T. Yardimci, and M. Jarrahi, "Plasmonics-enhanced photoconductive terahertz detector pumped by Ytterbium-doped fiber laser," *Opt. Express* **28**(3), 3835-3845 (2020).

[90] P-K. Lu, D. Turan, and M. Jarrahi, "High-sensitivity telecommunication-compatible photoconductive terahertz detection through carrier transit time reduction," *Opt. Express* **28**(18), 26324-26335 (2020).

[91] D. Turan, P-K. Lu, N. T. Yardimci, et al., "Wavelength conversion through plasmon-coupled surface states," *Nat. Commun.* **12**(1), 1-8 (2021).

[92] Berry, Christopher W., and Mona Jarrahi, "Plasmonically-enhanced localization of light into photoconductive antennas," In CLEO/QELS: 2010 Laser Science to Photonic Applications, pp. 1-2. IEEE, 2010.

[93] Hsieh, Bing-Yu, and Mona Jarrahi, "Analysis of periodic metallic nano-slits for efficient interaction of terahertz and optical waves at nano-scale dimensions," *J. Appl. Phys.* **109**(8), 084326 (2011).

[94] Berry, Christopher W., and Mona Jarrahi, "Ultrafast photoconductors based on plasmonic gratings," *2011 International Conference on Infrared, Millimeter, and Terahertz Waves*. IEEE, 2011.

[95] Berry, Christopher W., and Mona Jarrahi, "Terahertz generation using plasmonic photoconductive gratings," *New J. Phys.* **14**(10), 105029 (2012).

[96] Berry, Christopher W., Mohammad R. Hashemi, and Mona Jarrahi, "Generation of high power pulsed terahertz radiation using a plasmonic photoconductive emitter array with logarithmic spiral antennas," *Appl. Phys. Lett.* **104**(8), 081122 (2014).

[97] Heshmat, Barmak, et al., "Nanoplasmonic terahertz photoconductive switch on GaAs," *Nano Lett.* **12**(12), 6255-6259 (2012).

[98] Yang, Shang-Hua, et al., "7.5% optical-to-terahertz conversion efficiency offered by photoconductive emitters with three-dimensional plasmonic contact electrodes," *IEEE Trans. Terahertz Sci. Technol.* **4**(5), 575-581 (2014).

[99] Yang, Shang-Hua, and Mona Jarrahi, "Enhanced light-matter interaction at nanoscale by utilizing high-aspect-ratio metallic gratings," *Opt. Lett.* **38**(18), 3677-3679 (2013).

[100] Li, Xurong, Nezih Tolga Yardimci, and Mona Jarrahi, "A polarization-insensitive plasmonic photoconductive terahertz emitter," *AIP Adv.* **7**(11), 115113 (2017).

[101] Yang, Shang-Hua, and Mona Jarrahi, "Frequency-tunable continuous-wave terahertz sources based on GaAs plasmonic photomixers," *Appl. Phys. Lett.* **107**(13), 131111 (2015).

[102] C. W. Berry, et al., "Plasmonics enhanced photomixing for generating quasi-continuous-wave frequency-tunable terahertz radiation," *Opt. Lett.* **39**(15), 4522-4524 (2014).

[103] C. W. Berry, et al., "High power terahertz generation using 1550 nm plasmonic photomixers," *Appl. Phys. Lett.* **105**(1), 011121 (2014).

[104] Yang, S-H., et al., "Tunable terahertz wave generation through a bimodal laser diode and plasmonic photomixer," *Opt. Express* **23**(24), 31206-31215 (2015).

[105] Yang, Shang-Hua, and Mona Jarrahi, "Spectral characteristics of terahertz radiation from plasmonic photomixers," *Opt. Express* **23**(22), 28522-28530 (2015).

[106] Huang, Shu-Wei, et al., "Globally stable microresonator Turing pattern formation for coherent high-power THz radiation on-chip," *Phys. Rev. X* **7**(4), 041002 (2017).

[107] Wang, Ning, et al., "Room-temperature heterodyne terahertz detection with quantum-level sensitivity," *Nat. Astron.* **3**(11), 977-982 (2019).

[108] C. W. Berry, N. Wang, M. R. Hashemi, M. Unlu, and M. Jarrahi, "Significant performance enhancement in photoconductive terahertz optoelectronics by incorporating plasmonic contact electrodes," *Nat. Commun.* **4**(1), 1-10 (2013).

[109] N. T. Yardimci, D. Turan, S. Cakmakyapan, and M. Jarrahi, "A high-responsivity and broadband photoconductive terahertz detector based on a plasmonic nanocavity," *Appl. Phys. Lett.* **113**(25), 251102 (2018).

[110] N. T. Yardimci, D. Turan, and M. Jarrahi, "Efficient photoconductive terahertz detection through photon trapping in plasmonic nanocavities," *APL Photonics* **6**(8), 080802 (2021).

[111] N. T. Yardimci, S. Cakmakyapan, S. Hemmati, and M. Jarrahi, "A high-power broadband terahertz source enabled by three-dimensional light confinement in a plasmonic nanocavity," *Sci. Rep.* **7**(1), 1-8 (2017).

[112] N. T. Yardimci, and M. Jarrahi, “High sensitivity terahertz detection through large-area plasmonic nano-antenna arrays,” *Sci. Rep.* **7**(1), 1-8 (2017).

[113] N. T. Yardimci, and M. Jarrahi, “Nanostructure-Enhanced Photoconductive Terahertz Emission and Detection,” *Small* **14**(44), 1802437 (2018).

[114] S. G. Park, Y. Choi, Y-J. Oh, and K-H. Jeong, "Terahertz photoconductive antenna with metal nanoislands," *Opt. Express* **20**(23), 25530-25535 (2012).

[115] A. Jooshesh, L. Smith, M. Masnadi-Shirazi, et al., "Nanoplasmonics enhanced terahertz sources," *Opt. Express* **22**(23), 27992-28001 (2014).

[116] N. T. Yardimci, H. Lu, and M. Jarrahi, “High power telecommunication-compatible photoconductive terahertz emitters based on plasmonic nano-antenna arrays,” *Appl. Phys. Lett.* **109**(19), 191103 (2016).

[117] D. Turan, S. C. Corzo-Garcia, N. T. Yardimci, E. Castro-Camus, and M. Jarrahi, "Impact of the metal adhesion layer on the radiation power of plasmonic photoconductive terahertz sources," *J. Infrared, Millimeter, Terahertz Waves* **38**(12), 1448-1456 (2017).

[118] N. T. Yardimci, S. H. Yang, C. W. Berry, and M. Jarrahi, "High-power terahertz generation using large-area plasmonic photoconductive emitters," *IEEE Trans. Terahertz Sci. Technol.* **5**(2), 223-229 (2015).

[119] W. Mönch, “On the physics of metal-semiconductor interfaces,” *Rep. Prog. Phys.* **53**(3), 221 (1990).

[120] W. Mönch, “Barrier heights of real Schottky contacts explained by metal-induced gap states and lateral inhomogeneities,” *J. Vacuum Sci. Technol. B: Microelectronics and Nanometer Structures Processing, Measurement, and Phenomena* **17**(4), 1867-1876 (1999).

[121] J. Tersoff, “Schottky barriers and semiconductor band structures,” *Phys. Rev. B* **32**(10), 6968 (1985).

[122] L. F. J. Piper, T. D. Veal, M. J. Lowe, and C. F. McConville, “Electron depletion at InAs free surfaces: Doping-induced acceptorlike gap states,” *Phys. Rev. B* **73**(19), 195321 (2006).

[123] U. Nandi, K. Dutzi, A. Deninger, H. Lu, J. Norman, A. C. Gossard, N. Vieweg, and S. Preu, “ErAs:In(Al)GaAs photoconductor-based time domain system with 4.5 THz single shot bandwidth and emitted terahertz power of 164 μW,” *Opt. Lett.* **45**(10), 2812-2815 (2020).

[124] B. Globisch, R. J. B. Dietz, T. Göbel, M. Schell, W. Bohmeyer, R. Müller, and A. Steiger, “Absolute terahertz power measurement of a time-domain spectroscopy system,” *Opt. Lett.* **40**(15), 3544-3547 (2015).

[125] A. Mingardi, W. D. Zhang, E. R. Brown, A. D. Feldman, T. E. Harvey, and R. P. Mirin, “High power generation of THz from 1550-nm photoconductive emitters,” *Opt. Express* **26**(11), 14472-14478 (2018).

[126] G. Klatt, B. Surrer, D. Stephan, O. Schubert, M. Fischer, J. Faist, A. Leitenstorfer, R. Huber, and T. Dekorsy, "Photo-Dember terahertz emitter excited with an Er: fiber laser," *Appl. Phys. Lett.* **98**(2), 021114 (2011).

[127] M. L. Smith, R. Mendis, R. E. M. Vickers, and R. A. Lewis, "Comparison of photoexcited p-InAs THz radiation source with conventional thermal radiation sources," *J. Appl. Phys.* **105**(6), 063109 (2009).

[128] K. Liu, J. Xu, T. Yuan, and X. C. Zhang, "Terahertz radiation from InAs induced by carrier diffusion and drift," *Phys. Rev. B* **73**(15), 155330 (2006).

[129] P-K. Lu, D. Turan, and M. Jarrahi, "High-Power Terahertz Pulse Generation from Bias-Free Nanoantennas on Graded Composition InGaAs Structures," *Opt. Express* **30**(2), 1584-1598 (2022).

[130] M. Tani, S. Matsuura, K. Sakai, and S. I. Nakashima, "Emission characteristics of photoconductive antennas based on low-temperature-grown GaAs and semi-insulating GaAs," *Appl. Opt.* **36**(30), 7853-7859 (1997).

[131] M. Beck, Hanjo Schäfer, Gregor Klatt, et al., "Impulsive terahertz radiation with high electric fields from an amplifier-driven large-area photoconductive antenna," *Opt. Express* **18**(9), 9251-9257 (2010).

[132] M. Venkatesh, K. S. Rao, T. S. Abhilash, S. P. Tewari, and A. K. Chaudhary, "Optical characterization of GaAs photoconductive antennas for efficient generation and detection of Terahertz radiation," *Opt. Mater.* **36**(3), 596-601 (2014).

[133] P. J. Hale, J. Madeo, C. Chin, et al., "20 THz broadband generation using semi-insulating GaAs interdigitated photoconductive antennas," *Opt. Express* **22**(21), 26358-26364 (2014).

[134] Wang, N., & Jarrahi, M., "Noise analysis of photoconductive terahertz detectors," *J. Infrared, Millimeter, Terahertz Waves* **34**(9), 519-528 (2013).

[135] Turan, D., Yardimci, N. T., & Jarrahi, M., “0.4 mW Terahertz Power Generation through Bias-Free, Telecommunication-Compatible, Photoconductive Nano-Antennas,” In 2019 44th International Conference on Infrared, Millimeter, and Terahertz Waves (IRMMW-THz) (pp. 1-2). IEEE. (2019, September)

[136] Rothman, L. S., Gordon, I. E., Babikov, Y., Barbe, A., Benner, D. C., Bernath, P. F., ... & Campargue, A., “The HITRAN2012 molecular spectroscopic database,” *J. Quant Spectrosc Radiat Transfer* **130**, 4-50 (2013).

[137] Breuer, S., Kohlhaas, R. B., Nellen, S., Liebermeister, L., Globisch, B., Schell, M., ... & Masselink, W. T., “Transition Metal Doped InGaAs Photoconductors for THz Detectors,” In 2019 Compound Semiconductor Week (CSW) (pp. 1-2). IEEE. (2019, May).

[138] Göbel, Thorsten, Dennis Stanze, Björn Globisch, Roman JB Dietz, Helmut Roehle, and Martin Schell, "Telecom technology based continuous wave terahertz photomixing system with 105 decibel signal-to-noise ratio and 3.5 terahertz bandwidth," *Opt. Lett.* **38**(20), 4197-4199 (2013).

[139] Roggenbuck, Axel, Komalavalli Thirunavukkuarasu, Holger Schmitz, Jennifer Marx, Anselm Deninger, Ivan Cámara Mayorga, Rolf Güsten, Joachim Hemberger, and Markus Grüninger, "Using a fiber stretcher as a fast phase modulator in a continuous wave terahertz spectrometer," *JOSA B* **29**(4), 614-620 (2012).

[140] Liebermeister, Lars, Simon Nellen, Robert Kohlhaas, Steffen Breuer, Martin Schell, and Björn Globisch, "Ultra-fast, high-bandwidth coherent cw THz spectrometer for non-destructive testing," *J. Infrared, Millimeter, Terahertz Waves* **40**(3), 288-296 (2019).

[141] Liebermeister, Lars, Simon Nellen, Robert B. Kohlhaas, Sebastian Lauck, Milan Deumer, Steffen Breuer, Martin Schell, and Björn Globisch, "Optoelectronic frequency-modulated continuous-wave terahertz spectroscopy with 4 THz bandwidth," *Nat. Commun.* **12**(1), 1-10 (2021).

[142] Jarrahi, M., "Advanced photoconductive terahertz optoelectronics based on nano-antennas and nano-plasmonic light concentrators," *IEEE Trans. Terahertz Sci. Technol.* **5**(3), 391-397 (2015).

[143] Yardimci, N. T., Salas, R., Krivoy, E. M., Nair, H. P., Bank, S. R., & Jarrahi, M., "Impact of substrate characteristics on performance of large area plasmonic photoconductive emitters," *Opt. Express* **23**(25), 32035-32043 (2015).

[144] J. Lu, S. H. Lee, X. Li, S. C. Lee, J. H. Han, O. P. Kown, and K. A. Nelson, "Efficient terahertz generation in highly nonlinear organic crystal HMB-TMS," *Opt. Express* **26**(23), 30786-30794 (2018).

[145] A. Rovere, Y. G. Jeong, R. Piccoli, S. H. Lee, S. C. Lee, O. P. Kwon, M. Jazbinsek, R. Morandotti, and L. Razzari, "Generation of high-field terahertz pulses in an HMQ-TMS organic crystal pumped by an ytterbium laser at 1030 nm," *Opt. Express* **26**(3), 2509-2516 (2018).

[146] T. Seifert, S. Jaiswal, U. Martens, J. Hannegan, L. Braun, P. Maldonado, F. Freimuth, A. Kronenberg, J. Henrizi, I. Radu, and E. Beaurepaire, "Efficient metallic spintronic emitters of ultrabroadband terahertz radiation," *Nat. Photonics* **10**(7), 483-488 (2016).

[147] U. Nandi, M. S. Abdelaziz, S. Jaiswal, G. Jakob, O. Gueckstock, S. M. Rouzegar, T. S. Seifert, M. Kläui, T. Kampfrath, and S. Preu, "Antenna-coupled spintronic terahertz

emitters driven by a 1550 nm femtosecond laser oscillator," *Appl. Phys. Lett.* **115**(2), 022405 (2019).

[148] M. Klos, R. Bartholdt, J. Klier, J. F. Lampin and R. Beigang, “Photoconductive antennas based on low temperature grown GaAs on silicon substrates for broadband terahertz generation and detection,” In 2015 40th International Conference on Infrared, Millimeter, and Terahertz waves (IRMMW-THz) (pp. 1-1). IEEE.

[149] A. Singh, A. Pashkin, S. Winnerl, M. Helm, and H. Schneider, "Gapless broadband terahertz emission from a germanium photoconductive emitter," *ACS Photonics* **5**(7), 2718-2723 (2018).

[150] S. Bhargava, H-R. Blank, V. Narayanamurti, and H. Kroemer, "Fermi-level pinning position at the Au–InAs interface determined using ballistic electron emission microscopy," *Appl. Phys. Lett.* **70**(6), 759-761 (1997).

[151] M. A. Haase, V. M. Robbins, N. Tabatabaie, and G. E. Stillman, “Subthreshold electron velocity-field characteristics of GaAs and $In_{0.53}Ga_{0.47}As$,” *J. Appl. Phys.* **57**(6), 2295-2298 (1985).

[152] G. Sabatini, C. Palermo, P. Ziade, T. Laurent, H. Marinchio, H. Rodilla, J. Mateos, T. Gonzalez, R. Teissier, and L. Varani, “Monte Carlo study of ballistic effects in high speed InAs-based quantum hot electron transistor,” in *35th Int. Conf. Infrared Millim. Terahertz Waves* (2010), pp. 1-2.

[153] Y. Taur and T. H. Ning, *Fundamentals of modern VLSI devices*, (Cambridge University, 2013).

[154] E. Khutsishvilii, Z. Chubinishvili, G. Kekelidze, I. Kalandadze, T. Qamushadze, and M. Metskhvarishvili, "The Features of Electronic Conduction in InAs," *European J. Eng. Technol. Research* **6**(3), 75-78 (2021).

[155] E. S. Harmon, M. L. Lovejoy, M. R. Melloch, M. S. Lundstrom, D. Ritter, and R. A. Hamm, "Minority-carrier mobility enhancement in p+ InGaAs lattice matched to InP," *Appl. Phys. Lett.* **63**(5), 636-638 (1993).

[156] Arabshahi, Hadi, M. R. Khalvati, and M. Rezaee Rokn-Abadi, "Temperature and doping dependencies of electron mobility in InAs, AlAs and AlGaAs at high electric field application," *Brazilian J. Phys.* **38**, 293-296 (2008).

[157] Brennan, Kevin, "Theory of the steady-state hole drift velocity in InGaAs," *Appl. Phys. Lett.* **51**(13), 995-997 (1987).

[158] Kesamanly, F. P., Yu. MaTtsev, D. N. Nasledov, L. A. Nikolaeva, M. N. Pivovarov, V. A. Skripkin, and Yu. I. Uvanov, "Structure of the conduction band in indium arsenide (Indium arsenide crystals conduction band structure with various electron concentrations, determining electron mass dependence on concentration and temperature)," *Fiz. Tekhn. Polupr*. **3**(8), 1182-1187 (1969).

[159] T. P. Pearsall, *GaInAsP Alloy Semiconductors*, (John Wiley and Sons, 1982).

[160] I. Tångring, Y. X. Song, Z. H. Lai, S. M. Wang, M. Sadeghi, and A. Larsson, "A study of the doping influence on strain relaxation of graded composition InGaAs layers grown by molecular beam epitaxy," *J. Crystal Growth* **311**(7), 1684-1687 (2009).

[161] K. E. Lee, and E. A. Fitzgerald, "High-quality metamorphic compositionally graded InGaAs buffers," *J. Crystal Growth* **312**(2), 250-257 (2010).

[162] P. Kidd, D. J. Dunstan, H. G. Colson, M.A. Louren, A. Sacedo, F. Gonza, L. Gonza, Y. Gonza, R. Garci, D. Gonza, and F.J. Pacheco, "Comparison of the crystalline quality of step-graded and continuously graded InGaAs buffer layers," *J. Crystal Growth* **169**(4), 649-659 (1996).

[163] S. Kalem, J. I. Chyi, H. Morkoç, R. Bean, and K. Zanio, "Growth and transport properties of InAs epilayers on GaAs," *Appl. Phys. Lett.* **53**(17), 1647-1649 (1988).

[164] S. M. Sze, Y. Li, and K. K. Ng, *Physics of Semiconductor Devices*, (Wiley, 2021).

[165] S. L. Teitel, and J. W. Wilkins, "Ballistic transport and velocity overshoot in semiconductors: Part I—Uniform field effects," *IEEE Trans. Electron Devices* **30**(2), 150-153 (1983).

[166] G. H. Döhler, F. Renner, O. Klar, M. Eckardt, A. Schwanhäußer, S. Malzer, D. Driscoll, M. Hanson, A.C. Gossard, G. Loata, and T. Löffler, "THz-photomixer based on quasi-ballistic transport," *Semiconductor Sci. Technol.* **20**(7), S178 (2005).

[167] K. Brennan, and K. Hess, "High field transport in GaAs, InP and InAs," *Solid-State Electron.* **27**(4), 347-357 (1984).

[168] J. Park, J. H. Kang, X. Liu, S. J. Maddox, K. Tang, P. C. McIntyre, S. R. Bank, and M. L. Brongersma, "Dynamic thermal emission control with InAs-based plasmonic metasurfaces," *Sci. Adv.* **4**(12), 3163 (2018).